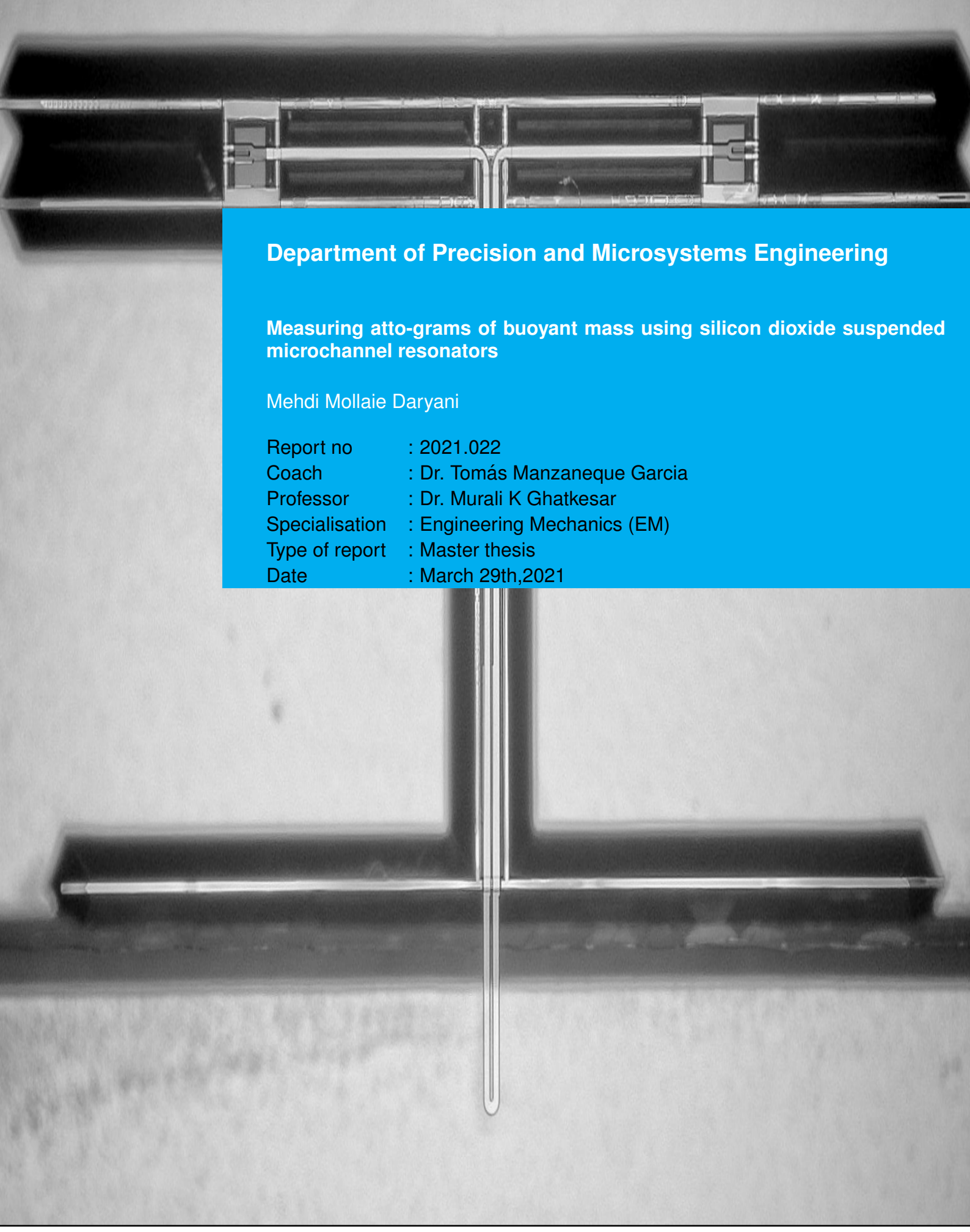

Department of Precision and Microsystems Engineering

Measuring atto-grams of buoyant mass using silicon dioxide suspended microchannel resonators

Mehdi Mollaie Daryani

Report no	: 2021.022
Coach	: Dr. Tomás Manzaneque Garcia
Professor	: Dr. Murali K Ghatkesar
Specialisation	: Engineering Mechanics (EM)
Type of report	: Master thesis
Date	: March 29th,2021

TU Delft Delft University of Technology

Challenge the future

Measuring atto-grams of buoyant mass using silicon dioxide suspended microchannel resonators

by

Mehdi Mollaie Daryani

to obtain the degree of Master of Science
at the Delft University of Technology,
to be defended publicly on Monday March 29, 2021 at 3:00 PM.

Student number:	4418492	
Project duration:	October 24, 2019 – March 29, 2021	
Thesis committee:	Dr. Murali K Ghatkesar,	TU Delft, Chair
	Dr. Tomás Manzaneque Garcia,	TU Delft
	Dr. Gerard Verbiest,	TU Delft

TU Delft

Preface

The thesis in front of you presents my work on precise mass measurements of nanoparticles using TUDelft fabricated suspended microchannel resonators. This is one of the final steps in development of our device providing single nanoparticle mass sensing in a robust and precise manner.

Readers who are mainly interested in nanoplastics and available detection methods can find them in Chapter 1 to Chapter 3. SMR's theory can be found in Chapter 4. The results and graphs can also be found in the paper and throughout the supplementary notes, and readers, who are specially interested in PLL-resonator design and modeling can find them in Section 7.1 and Section 7.2.

The gratitude I owe to my supervisors for numerous discussions during online or face to face meetings on my project, which are the core of my understanding about mass sensing by a SMR, is disproportionate to the small size: Dr. Murali k.Ghatkesar and Dr. Tomás Manazaneque. Thanks for continuous support of my research by patience, enthusiasm, motivation and immense knowledge.
I am indebted to my brother, Salar, for encouragements and stimulating discussions.
Finally, this material would never have existed without continuous help and support of the rest of my beloved family, over the past years.

Delft, February 2021

Summary

In connection with growing in applications of nanoparticles in various industrial sectors such as cosmetics and pharmaceuticals, the demands for in-line identification and characterization of nanoparticles suspended in fluids has increased. In addition to that, nanoparticles in general and nanoplastics in particular, can easily contaminate air and water resources, resulting in human health risks. Among available techniques, suspended microchannel resonators can respond to the characterization demands in terms of mass detection and concentration of nanoparticles in fluids. This technique is based on changes in resonance frequency of the suspended microchannel due to flowing of nanoparticles through the suspended hollow cantilever.

In this project we aimed to characterise TUDelft made suspended microchannel resonators in terms of mass limit detection and speed of detection. To achieve this, firstly, the modal analysis was conducted to determine the resonance frequencies of two bending modes and first torsional mode. Secondly, a phase-locked loop was designed to track the resonance frequencies. Then, the frequency stability of the measurements was studied using the Allan deviation method. Finally, the mass detection limit was obtained by conversion of Allan deviation's data. The detection speed was also computed using the characteristic time constant of the system.

We found that the lowest resolved mass can be detected by the second bending mode. This was 0.11 fg and 0.38 fg using an empty and a water-filled resonator respectively, for a system bandwidth of 1000 Hz that corresponds to a system settling time of 0.37 ms. We also managed to measure a buoyant mass of 21.2 fg which is an equivalent gold nanoparticle of 130 nm in diameter, during one of the attempts to detect suspended gold nanoparticles in deionized water.

In order to achieve continuous and precise mass measurements of nanoparticles suspended in fluids, it is recommended that: i) fabrication of a new suspended microchannel resonator that allows for working continuously without experiencing fractures in it earlier than applying flow driven pressure, ii) equipping our setup with a sensitive flow rate sensor in the range of (pL/s) that provides regulating fluid flow smoothly and iii) applying matched filter methods that allows for automatic peak detections in a continuous measurement.

Acronyms

ADEV Allan deviation. 50

AFM Atomic Force Microscopy. 12, 13

AVAR Allan variance. 50

BSE backscattered electrons. 10

DLS Dynamic light Scattering. 8, 76

DUT Device Under Test. 20

EDS Energy Dispersive X-ray Spectroscopy. 10, 11

FFT Fast Fourier Transform. 49

FM Frequency Modulation. 50

FPGA Field programable Gate Array. 20

FTIR Fourier Transform Infrared Spectroscopy. 5, 6

IR Infrared. 5, 6

LDV Laser Doppler Vibrometer. 18

LF Loop Filter. 18

MALS Multi Angle Light Scattering. 7

MS Mass Spectrometry. 6, 8, 9, 13

PD Phase Detector. 18, 45

PE Polyethylene. 3

PLL Phase-Locked Loop. iii, 18, 20, 39, 42–44, 46–48, 59–61, 75, 76

PP Polypropylene. 3

PS Polystyrene. 3

PSD Power Spectral Densities. 49

PUR Polyurethane. 3

PVC Polyvinyl chloride. 3

Pyr-GC-MS Pyrolysis-Gas Chromatography-Mass Spectrometry. 6, 7

SE secondary electrons. 10

SEM Scanning Electron Microscopy. 10–13

SMR Suspended Microchannel Resonator. iii, 13, 17–20, 48, 75, 76

SNR Suspended Nanochannel Resonator. 18, 50

TEM Transmission Electron Microscopy. 11–13

UV-Vis Ultraviolet - Visible Spectroscopy. 9, 10

VCO Voltage Controlled Oscillator. 18

Contents

I

Literature review

1

Introduction

Today, plastic products are involved in many fields from health to textiles and construction. The world plastic production has raised dramatically, from 2 million tons in 1950 to almost 360 million tons in 2018 [41, 45]. Synthetic polymers such as polyethylene (PE), polystyrene (PS), polyurethane (PUR), polypropylene (PP) and polyvinyl chloride (PVC) are the core of plastics. In addition to polymers, additives are added to plastics to enhance their mechanical, chemical and visual characteristics such as strength, fire resistance and colouration [45].

In recent years, the topic of nanoplastics pollution became a matter of public concern since the existence of nanoplastics was reported in marine waters [127] and in facial scrubs [54]. However, break down of microplastics into smaller than $1\mu m$ particles had already been claimed in publications [32]. This degradation can be mechanical degradation by waves in aquatic environments, photodegradation by sunlight or ultraviolet radiation and thermooxidative degradation which occurs at moderate temperature [81]. Since this is a new issue for researchers, size classification of nanoplastics is still under discussion. Some authors set the upper limit at $1000nm(1\mu m)$ for nanoplastic, while others define nanoplastics in the size ranges $1nm - 100nm$ [18, 47, 113, 127]. In the following discussion nanoplastics are defined as plastic particles in the sizes smaller than $1\mu m$. Nanoplastics sources are categorized into primary particles, which are manufactured on purpose e.g. nano scaled plastic particles used in cosmetics, and secondary nanoplastics particles, i.e. plastic particles degraded and fragmented from larger plastic particles [81, 113]. Industrial and human activities such as waste disposal and coastal landfill operations contribute to the distribution of secondary particles in freshwater and marine environment [80, 81]. However, primary particles from pharmaceutic and cosmetic industries, which are used in consumer products, are introduced directly into the environment via wastewater or during consumption [80, 81].

Basically, nanoparticles properties in terms of physical, electric, chemical and mechanical characteristics differ from those of corresponding bulk material due to their broad range in size [16]. Therefore, there could be a material which is nontoxic in bulk while it can be toxic at nanoscale owing its characteristic properties[64]. However, it has not been fully understood which parameter has the greatest influence on toxicity of nanoparticles and there might be a large number of parameters (e.g. chemical composition, size, shape, mass concentration, charge and high surface area to volume ratio and etc.) which are responsible for potentially harmful effects of nanoparticles [81]. Nanoparticles can rapidly interact with biomolecules which are available in biological fluids (e.g. human plasma) due to their high surface free energy [84]. This interaction with proteins results in a biological coating which is know as "the protein corona" on the nanoparticle's surface. This corona changes the biological identity of the particle. This is detrimental in the medical applications in which drugs delivery to the target organs is vital [126]. Suppose, nano drug particles, which are supposed to target a specific organ of body, are covered by the protein corona and their biological identity are changed. Therefore, they might target another organ which does not need drugs. Coming back to plastics, despite possessing various chemical compositions, plastics also can transport other chemicals and materials due to their surface low polarity. Consequently, plastic particles can adsorb or absorb hydrophobic contaminants such as persistent organic pollutants (POPs) [80, 128]. This carrier effect can be enhanced in nano scale because of larger ratio of surface area to volume in nanoplastics compared to micro or meso plastic paticles [80].

In order to investigate health impacts of micro and nanoplastics, exposure routes need to be identified. Literature suggests that there are three possible routes of human exposure to micro and nanoplastics including: oral exposure (drinking water and food chain), dermal exposure (water and cosmetics) and inhalation (air) [72, 107]. Drinking water could be contaminated if filtration systems of water treatment do not detect micro and nanoplastics which pass through filters. Plastic waste degraded to the nano size or manufactured nano scale plastic particles can enter the aquatic food web via bacteria, zooplankton and algae, which are eaten by filter feeders and then consumed by fishes and humans [80], as the presence of microplastics have already been reported in zooplankton [30], mussels [73] and fishes [89]. Dermal exposure involves human's skin interactions either with water containing micro and naoplastics during washing or via available nano and microplastics in personal care products. Although the uptake of microplastics by skin is unlikely to happen due to the micron size which does not allow for penetration, nanoplastics can eventually enter the humans skin [107]. Air can also carry micro and nanoplastics which become airborne, and they can be in contact with humans through inhalation [72, 107]. Although concerns have been raised that micro and nanoplastics impact human health, investigations are still limited and they are mostly concerned with microplastics rather than nanoplastics. It is claimed that microplastics might enter the blood circulation through lymph, but due to their size, translocation across cellular membranes is very unlikely, resulting in light penetration in organs [18]. Therefore, they may locally engage the immune system as inflammation of the gut is expected[103]. In contrast, nanoplastics, due to their small size, can pass biological barriers to penetrate organs and can move across immune cells [18, 72]. However, the potential toxicity of nanoplastics on humans has hardly been verified [18, 107].

One of the barriers for conducting research on nanoplastics is the reliable detection methods in water and tissues [72]. Inevitably, all research involving micro and nanoplastics contains two main steps: sample preparation and analysis of the prepared sample [90, 113]. The sample preparation step contains digestion approaches, concentration methods and separation methods [90, 113]. Digestion approaches, such as acid treatment or enzymatic protocol, remove possible matrices such as organisms and tissue from the sample. The concentration methods provide detectable amount of sample for a specific analysis method, but the separation methods separate micro and nanoparticles from other particles with various sizes [90, 113]. The separation methods are dependent on two factors: first, the type of sample such as biological samples (fish, mussels or plankton), sediment samples (beach sediment or deep see sediment) or water samples (wastewater, drinking water, see water or fresh water), and second, the analytical methods which are supposed to be applied afterwards [90, 113]. The suggested methods for concentration of nanoplastics are [18, 113]: membrane filtration, ultrafiltration (UF), ultracentrifugation (UC), while methods such as field flow fraction (FFF), asymmetric flow field flow fraction (AF4) and hydrodynamic chromatography (HDC) have been claimed for separation techniques. Following the sample preparation methods, analysis techniques, detection and identification of nanoplastics, which are the final aim of this report, are required. In order to detect and identify micro- and nanoplastics, literature suggests some analytical techniques including thermal, spectroscopic, as well as light scattering and microscopic methods which yield determining either physical characteristics such as size and mass of particles or the chemical composition of particles [18, 81, 106].

In the following sections, first, the suggested detection techniques with their advantages and limitations are introduced. An alternative method then is proposed and explained. Finally, the research questions, time plan and approaches to obtain the desired result are discussed.

2

Detection methods

In this chapter, techniques that have already been applied in submicro- and nanoplastics are reviewed. The physics behind the techniques and possible pros and cons are discussed.

2.1. Fourier Transform Infrared Spectroscopy (FTIR)

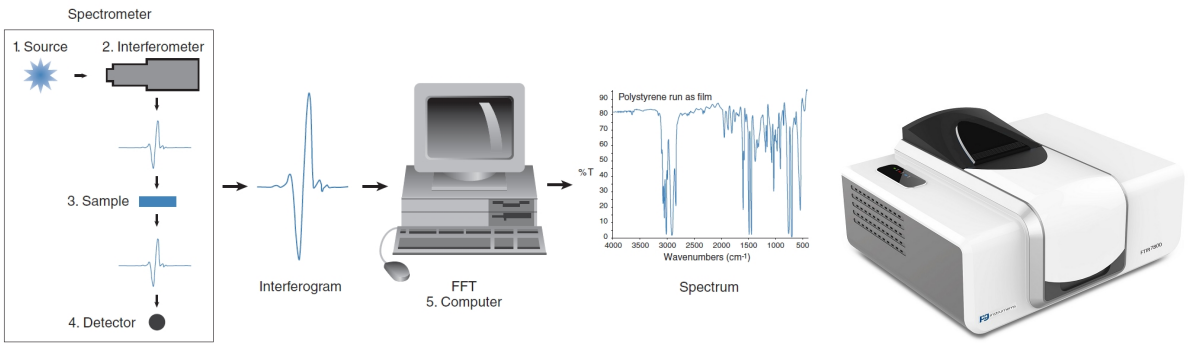

Figure 2.1: *(a) Schematic of FTIR technique [129]. (b) FTIR 7800, an example of FTIR spectrometer[101].*

FTIR is an infrared spectroscopy technique which has been widely employed to identify the type of plastics. Owing to its reliability, simplicity and accurate spectra, FTIR has become the predominant technique for identifying the type of plastics[55, 75, 131]. This technique relies on changes in dipole moment of specific group of materials as a result of molecular vibration caused by absorption of IR radiation of that molecule [86, 116, 143].
In FTIR [33, 116, 119, 129]: First, a fitting light source generates IR radiation which enters an interferometer (e.g. Michelson) and is directed to a beam splitter. Then, the split beams are cast over a fixed and moving mirror respectively so that they cause interference in return. Next, the recombined beam, which leaves the interferometer, is directed at a sample. The sample then absorbs some amounts of light (absorption), while the remaining light which passes trough the sample (transmittance) will be collected by a detector to produce a raw signal (interferogram) of light intensity versus mirror positions. Hence, the spectral information of all wavelengths is gained at the same time. Thereafter, the information which was presented in the interferogram is decoded by means of computers and Fourier transform. To do this, initially, an interferogram is made without inserting the sample and the Fourier transform is mathematically applied to this raw information, resulting in a plot of IR intensity as a function of wavenumbers (Reference spectrum). Afterwards, the last step is repeated but this time in the presence of sample (Sample spectrum). Lastly, two spectra are combined to form transmission spectrum of the IR light as a function of wavenumbers. In the finale stage of FTIR, once the IR spectrum is obtained, the IR spectrum is compared with available reference spectra of other materials to identify chemical type of the sample.

FTIR is non-destructive, fast and reliable although its major disadvantage is the low detection sensitivity (particle down to $\approx 25\mu m$ in size) [123].

2.2. Raman Spectroscopy (RM)

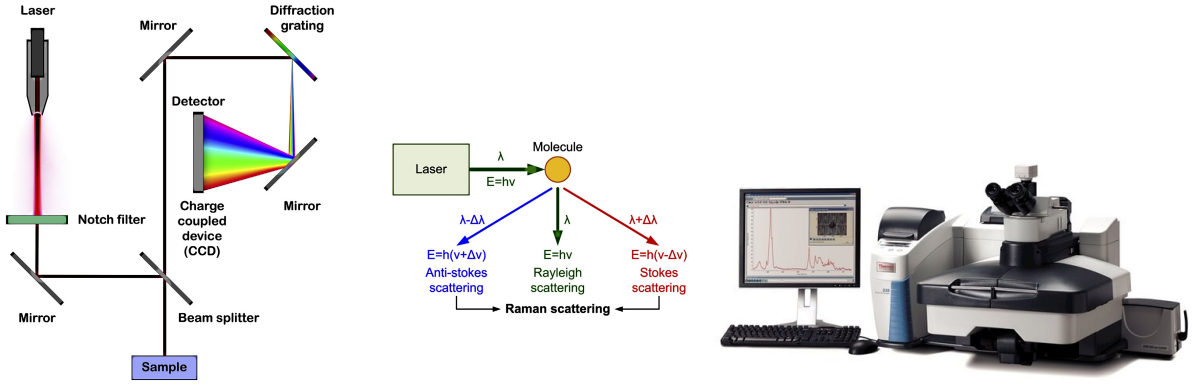

(a) (b)

Figure 2.2: *(a) Schematic of Raman spectrometer [33] and principle of Raman scattering [105]. (b) DXR™3 Raman Spectroscopy Microscope[130], a commercial Raman spectrometer with microscope.*

Raman is a spectroscopic technique which allows for the identification of polymers. The physics behind Raman spectroscopy is concerned with the Raman scattering [33, 105]: When a sample is irradiated with a laser light, some of the light is absorbed and scattered due to interaction between photons of light and the molecules of the sample. Rayliegh scattering (elastic) and Raman scattering (inelastic) are two forms of scattered light, as illustrated in 2.2(a). An extreme large portion of the scattered light is Rayleigh scattering(elastic) which has identical frequency with the incident light, meaning that there are no energy levels differences between the incident and emitted photons. However, the energy exchange between the photons and sample's molecules also produces inelastic scattering light which is called either anti-Stokes scattering when the emitted photons gain energy or Stokes when the emitted photons lose energy in this energy exchange.
In this technique [33, 105, 117]: First, a monochromatic laser source in visible or near IR region irradiates a sample by means of optical devices. The sample then absorbs and scatters either elastically or inelastically the incident light. Finally, the Raman scattered light which contains information about molecular structure and characteristic of the types of bonds are collected by a detector to produce Raman spectrum, which is unique for each type of materials, with characteristic peaks at a fixed wave lengths related to a particular molecular vibration.
Raman is a non-destructive, easy, fast and potent technique for chemical identification of plastic particles (micro plastics) [6, 33, 105]. Furthermore, this technique which also can be coupled to microscopy [30] is able to identify small microplastics (down to 2 μm).

2.3. Pyrolysis-Gas Chromatography-Mass Spectrometry (Pyr-GC-MS)

Pyr-GC-MS is an analytical thermal technique to identify sample's compositions. In order to obtain compounds, a pyrolyzer, a gas chromatograph (GC) and a mass spectrometer (MS) are combined (see 2.3(a)).
The operating principle is as follows: First, inside the pyrolyzer, large molecules of the sample in terms of molecular weight are decomposed into smaller molecular weight molecules at a fixed temperature (between 200-600 $°C$) in an oxygen free atmosphere[33]. The decomposed molecules are then injected into GC under a gas flow of helium (He) as carrier to be separated depending on their volatility (lower volatile particles move slower and vice versa). Finally, the separated volatile particles enter the MS where they get ionized, deflected by an electromagnetic field, and detected based on their mass to charge ratio [13]. The result of Pyr-GC-MS is a chromatogram which can be compared by an electronic database of known compounds to identify the unknown compounds.
Advantages and disadvantages of this technique are [83, 100]: Pyr-GC-MS is an easy operating technique (the samples only need to be transferred into pyrolyzer without any pretreatments). Furthermore, this technique

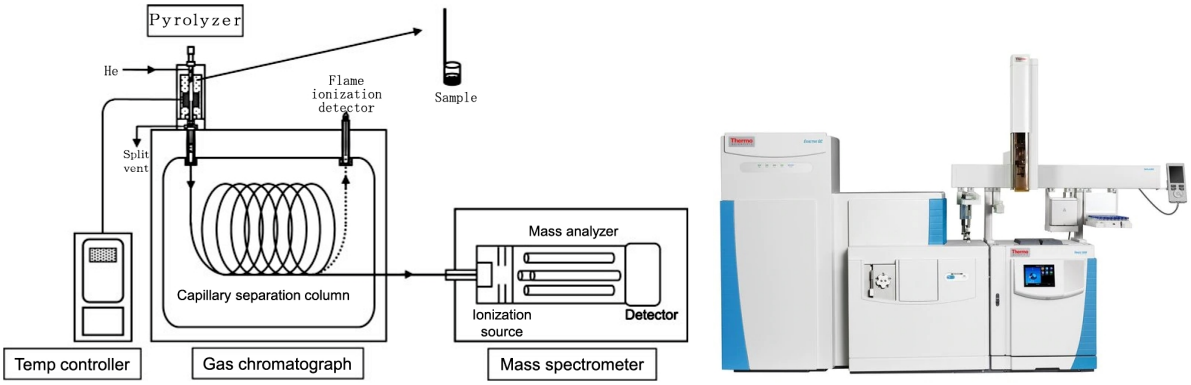

(a) (b)

Figure 2.3: *(a) The Pyr-GC-MS instrument components[135]. (b) The GC Orbitrap-MS System [58].*

is not affected by particle shapes. However, this technique is a time consuming (one run of Pyr-GC-MS takes around 30 minutes) and destructive method which does not release information on particles sizes.

2.4. Multi Angle Light Scattering (MALS)

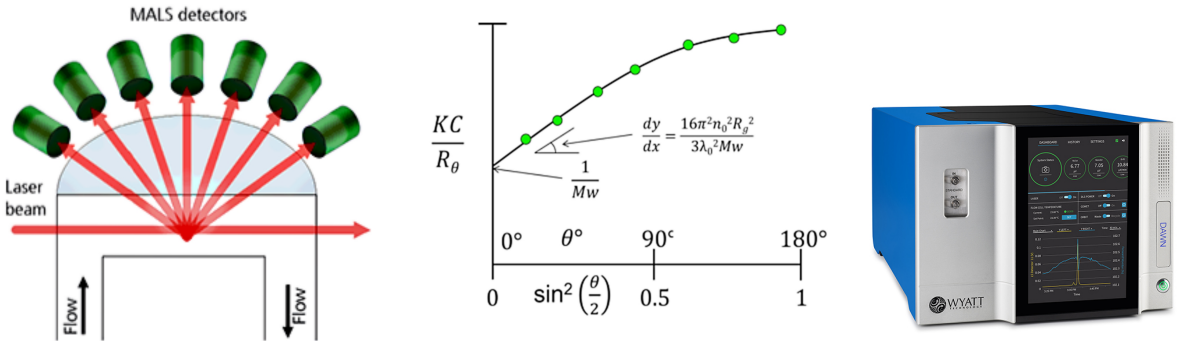

(a) (b)

Figure 2.4: *(a) Schematic of MALS technique and Deby plot[2]. (b) A commercial MALS (MALS) for detection of the molar mass and size of macromolecules and nanoparticles in solution. [142].*

The MALS is a powerful technique to measure the molar mass(M_w) and radius of gyration(R_g) of particles and molecules. The MALS principle is based on the Rayleigh theory which describes the relation between the average intensity of the scattered light (elastic scattering) by the sample and its R_g and M_w [102]. The Rayleigh approximation [141] relates Rayleigh ratio R_θ which is a function of intensity of the scattered light and M_w by:

$$\frac{KC}{R_\theta} \approx \frac{1}{M_w P_\theta} \tag{2.1}$$

where K is the optical constant, C is the concentration of particles in solution and P_θ which equals one at $\theta = 0$ is the particle scattering function.
As it can be seen in 2.4(a), a laser beam irradiates a sample and the intensity of scattered light is detected at various angles (3 to 18 different angles) by multiple detectors. The detected intensity is then brought into Deby plot by using the Rayleigh equation. Finally, a best fit is drawn and extrapolated back to $\theta = 0$ where M_w is calculated from the intercept and the initial slope of the fit line is used to calculate R_g [2]. MALS is limited to monodisperse flowing particles, while environmental suspensions are polydisperse [68, 144]. Therefore, MALS is always fed by a size separation technique e.g. AF4 which could increase the measurement time and complexity of this method [31, 83].

2.5. Dynamic Light Scattering (DLS)

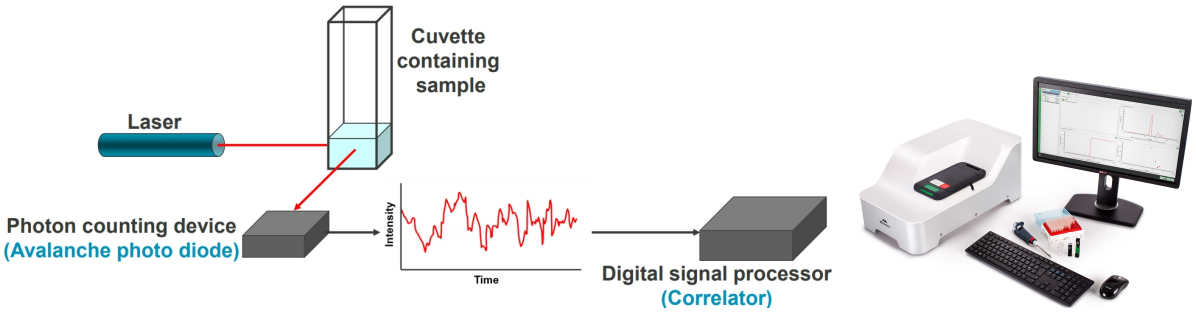

(a) (b)

Figure 2.5: *(a) DLS Instrument Components[65] and (b) Zetasizer Ultra, a commercial DLS system [3].*

Dynamic light Scattering (DLS), also recognized as "photon correlation spectroscopy", is an optical technique which is concerned with measurements of dispersed particles size in liquid media [104]. The DLS determines the hydrodynamic diameter $d(H)$ of the particles by measuring the Brownian motion which is defined as the random movement of particles due to collisions with the solvent molecules in the surrounding. It implies that how smaller are the particles, how faster they diffuse. The rate (velocity) of the Brownian motion is characterized by the translational diffusion coefficient (D) which is used in Stokes-Einstein equation to calculate the hydrodynamic diameter $d(H)$. Equation 2.2 describes this relation [77]:

$$d(H) = \frac{KT}{3\pi\eta D} \tag{2.2}$$

where T stands for the temperature in Kelvin, k is the Boltzmann constant, η is the viscosity , and D is he translational diffusion coefficient and $d(H)$ is the hydrodynamic diameter of the particle.
In DLS, particles are illuminated with a laser. Particles then scatter some of the light that hits them. It is called dynamic since if these particles were completely still we would measure a constant intensity of scattered light. However, since in a dispersion, diffusion causes the intensity of light scattered by the particles to fluctuate over time. The fluctuating intensity signal is created by combining the detected light scattered from lots of randomly diffusing particles. Afterwards, consecutive snapshots of the light scattering signal are taken rapidly. These snapshots are always compared to the original signal measured to obtain a correlation graph. Based on the correlation graph, the translational diffusion coefficient (D) which is used for determination of the hydrodynamic size is calculated[65].
DLS has several advantages including: simplicity, fast operating time, being non-invasive, being low-cost and requiring low amount of sample[86, 113, 134]. It should, however, be considered that DLS is concerned with theoretical models which work with equivalent sphere's radious, hence particle's shape is ignored. DLS optimally measures the monodisperse suspensions since scattered light intensity of smaller particles could be masked by those of larger particles [74, 113]. Moreover, DLS overestimates large particles since the light intensity (I) is theoretically correlated with (d^6) which is the particle's diameter to the power six[74, 113].

2.6. Mass Spectrometry (MS)

MS is a technique that is categorized under analytical methods for chemical composition and molecular weight determination of the samples [74, 133]. This method is normally coupled to separation techniques e.g. gas/liquid chromatography or Pyr-GC (see **??**). MSs seek to acquire mass to charge (m/z) ratio of ionized particles. The three major parts of mass spectrometers are an ion source which is responsible for producing gas phase ions from chemical substances (ionization), an analyser that separates the ionized particles based on their m/z values, and a detector which is responsible for generating signals from the separated ions [138]. There are various types of mass spectrometers since there are distinct techniques for either ionization of particles e.g. electron impact (EI), chemical ionization (CI), laser desorption (LD), electrospray ionization (ESI), or separation of ions e.g. magnetic sector analyzers, quadrupole ion traps, time-of flight (TOF), quadrupole mass filters analyzers [61, 138].

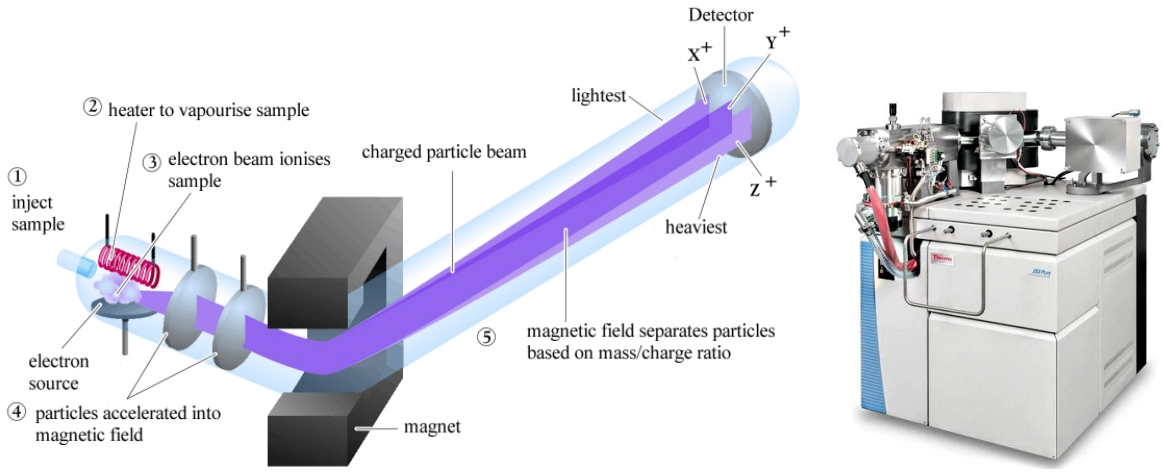

Figure 2.6: *(a) Simple schematic of a mass spectrometer [56] and (b) 10 kV Isotope Ratio Mass Spectrometer [5].*

2.6(a) depicts the EI-magnetic mass spectrometer. Its operation is as follows [99, 138]: First, a small amount of the sample is heated and evaporated and injected into the ionization chamber where an electron-beam is produced by a filament to ionize the vapour particles via inductive effects and losing valance electrons. Second, the ionized particles enter an electrostatic field which accelerates the ions by increase in their kinetic energy before their arrival at the analyzer. Third, in presence of a magnetic field which is perpendicular to the ions moving direction, the accelerated ionized particles follow a curved track which allows ions to be separated based on their momentum (particles are deflected inwards or outwards the curved path). Equation 2.3 which is an outcome of Lorentz force, angular momentum, as well as kinetic energy shows that ions with various m/z ratio can be forced to reach the detector by varying either magnitude of the magnetic field (B) or voltage of the electrostatic field (U). Other parameters are the charge of an electron (e) and the radial path of the moving ion (r). Finally, a detector collects and sends the gathered information to a computer for obtaining a mass spectrum of relative abundance of detected particles as a function of the m/z ratio.

$$\frac{m}{z} = \frac{B^2 r^2 e}{2U} \tag{2.3}$$

Despite its high accuracy and reliability in chemical identification, MS is a destructive and an expensive technique which only can detect charged particles, meaning that particles which are not ionized for any reasons will be out of detection process [26, 74].

2.7. Ultraviolet - Visible Spectroscopy (UV-Vis)

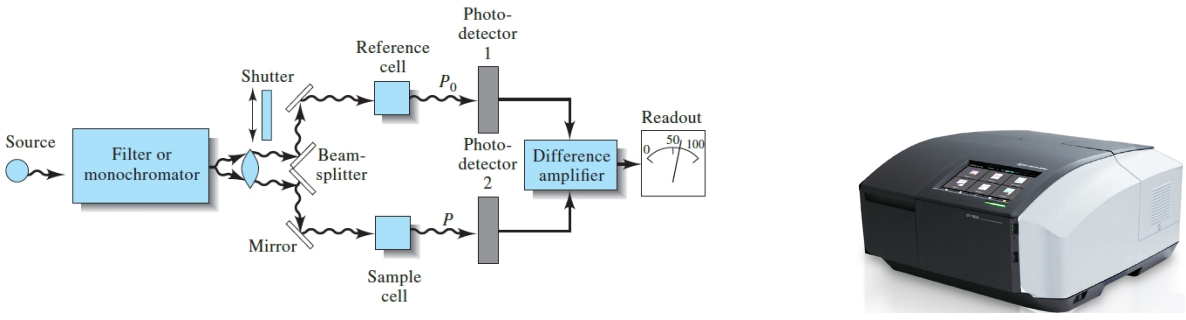

Figure 2.7: *(a) Instrumental design for UV-visible spectrometer[118] and (b) An example of UV-vis spectrometer [4].*

UV-Vis is another characterization method that is employed for both qualitative and quantitative study of nanoparticle materials in transparent fluids [6, 114]. This technique is based on electronic energy transitions

between orbitals of molecules and atoms of the sample so that the absorbed wavelength by the sample has the required energy for moving an electron from lower energy level to the higher one [11, 51, 96].
In UV-Vis spectroscopy [96, 118]: First, a light source comprises one or more lamps which provide ultraviolet and visible electromagnetic radiation shines on the entrance slit of a monochromator to filter out unnecessary wavelengths. A beam splitter is then used to split the light beam into two directions which simultaneously allow the light beams traverse both reference solution and the sample to two identical detectors. In the end, the two outputs are used to determine either transmittance, absorbance, and concentration of the sample by applying the Beer-Bouguer-Lambert law or the UV-Vis spectrum which plots the absorbance changes of the sample versus the wavelength ranges. The acquired UV-Vis spectrum can be overlaid onto the standard spectra for identification of the sample.
Although, UV-Vis spectroscopy is simple to use and inexpensive for determination of sample's concentration, it is not a reliable method for identification of nanoparticles due to the possible change in absorption characteristic of nanoparticle while they interact with fluids [50, 96, 114, 137].

2.8. Scanning Electron Microscopy(SEM)

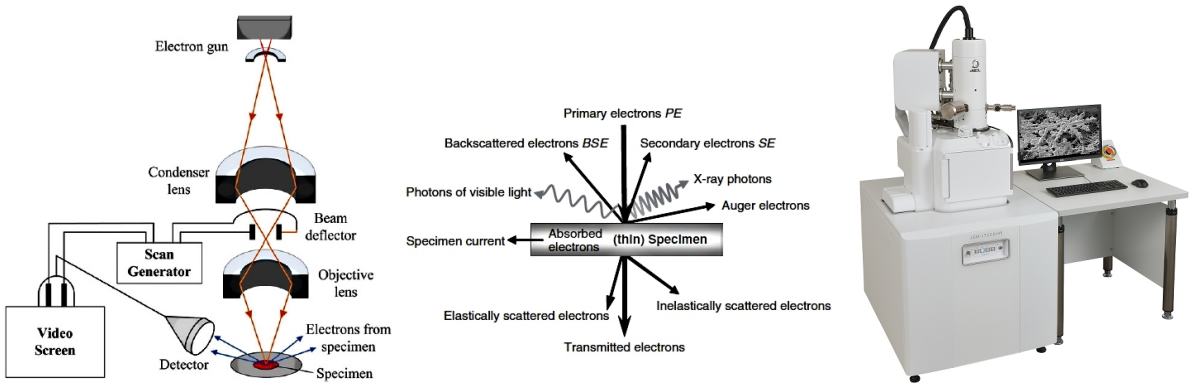

(a) (b)

Figure 2.8: *(a) The SEM working principle diagram [148] and generation of some useful signals when a focused electron beam hits a sample [121]. (b) The JSM-IT500HR InTouchScope™ SEM which has been designed for multiple attachments, e.g. energy dispersive X-ray spectrometer (EDS) [62].*

Scanning electron microscopy (SEM) is a microscopy technique for the analysis of micro- and nanostructures. SEM technique collects and processes signals that are generated when a focused beam of electron hits a sample to provide useful information on the topography (by means of high quality images) and composition(in combination with EDS technique) of the sample's surface[52]. The SEM basically consists of 4 major parts: a vacuum column which contains the electron source and the electromagnetic lens system as well as the scanning unit, a chamber which contains specimen holder, detectors and the imaging units(see 2.8(a)).
SEM working principle is as follows: First, the electron gun at the top of the SEM's column emits electrons that are accelerated by means of acceleration voltage. Second, these electrons pass through the lens system to form a focused electron beam(referred to as primary electron (PE)) which can be deflected in X and Y directions by two pairs of scanning coils. The focused electron beam then hits the specimen's surface and evokes various type of signals which can be detected, amplified and translated either into topographic images or into chemical characterization spectra. The principal signals which are captured in SEM are backscattered electrons (BSEs) and secondary electrons(SEs). The BSEs and SEs are detected to form SEM images (physical characteristics), however a portion of X-ray emission which is called characteristic X-rays is captured by a dispersive X-ray energy detector for composition analysis (referred to as Energy Dispersive X-ray Spectroscopy (EDS)) of the sample [37, 52].
Although, SEM-EDS provides high quality images and elemental composition of a sample, this technique is expensive and requires considerable time and effort for preparation of the sample when the sample is volatile and less conductive [122].

2.9. Transmission Electron Microscopy (TEM)

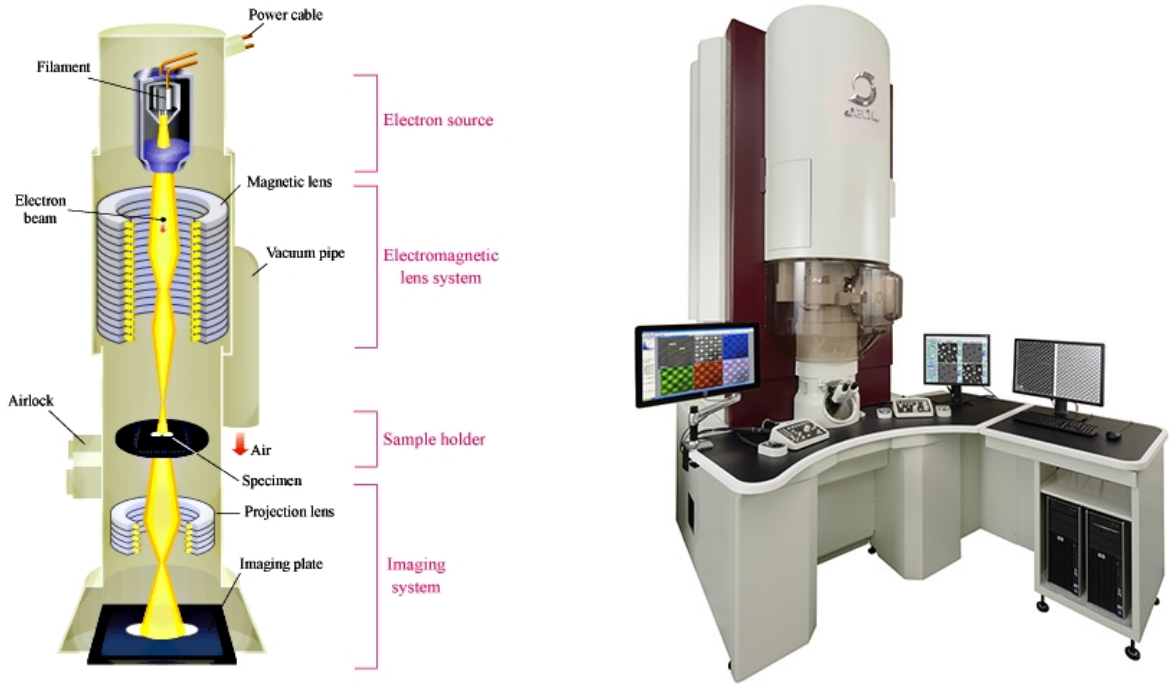

(a) (b)

Figure 2.9: *(a) Schematic diagram of transmission electron microscope [1] and (b) JEOL JEM-ARM300F Transmission Electron Microscope with 55pm resolution at 300kV [60].*

TEM is a technique which provides direct images of the sample to investigate nanoparticles shapes and sizes [79]. In addition to morphological and structural analysis, other techniques (e.g. EDS) can be attached to TEM for elemental composition analysis [79, 136]. Basically, electron microscopy techniques including TEM and SEM (see **??**) are based on wavelike characteristic of electrons. The electron wavelength is described by Equation 2.4 [10]:

$$\lambda = \frac{h}{p} = \frac{h}{mv} \tag{2.4}$$

where h, m, v ,p stand for Planck constant, electron mass, speed of electron and momentum of electron respectively. The achieved wavelength by this technique can pass through a solid of several μm thickness [38]. A conventional TEM comprises an illumination system (electron gun and electromagnetic lenses), a specimen holder and an imaging system (see 2.9(a)).
In TEM [38, 124]: Initially, an electron gun generates electrons which are accelerated and focused by several electromagnetic lenses. The focused electron beam then hits the sample resulting in transmission or reflection of the electrons. Next, the transmitted electrons are magnified to produce an image on a fluorescent screen by means of certain number of electromagnetic lenses. Finally, there are cameras to capture and transmit the images to a computer for further analysis.
Despite high resolution images and attachments (e.g. EDS) capabilities leading to physical and chemical characterization of the sample, there are some drawbacks for TEM. As wel as being an expensive (roughly 3K€-7M€) technique, TEM also requires costly maintenance due to their components such as high vacuum environment, specimen holder, cameras and etc. Furthermore, TEMs require a very thin layer (nonometer scale) sample which greatly increases time and effort in extensive sample preparations by highly trained operators [79].

2.10. Atomic Force Microscopy (AFM)

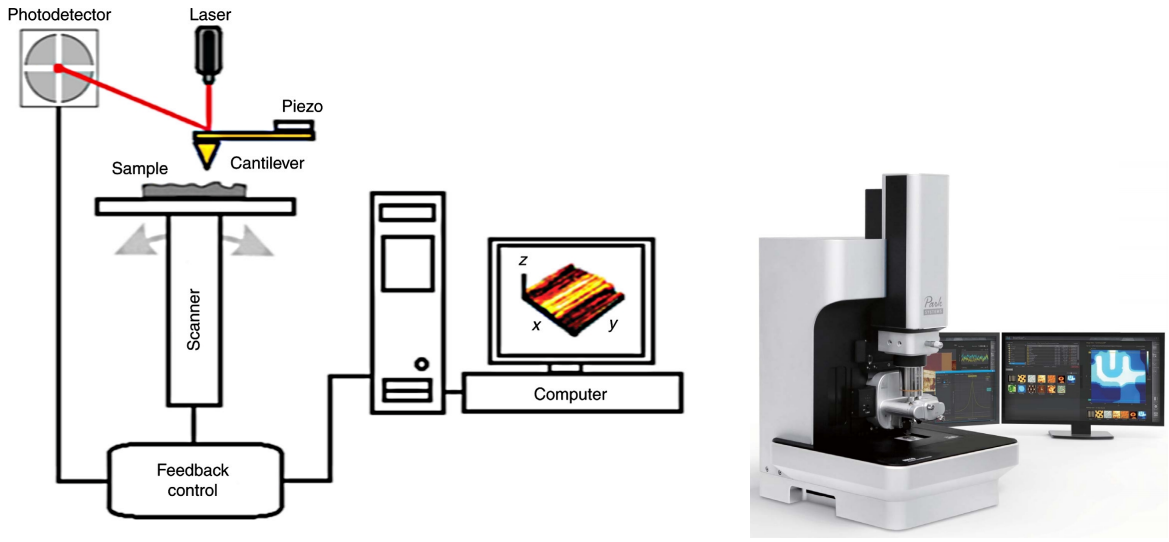

(a) (b)

Figure 2.10: *(a) Illustration of operating principles of AFM[125] and (b) Park NX10 Atomic force microscope [97].*

AFM is a microscopy technique which is employed to obtain topographic images down to nanometer scale primarily [43, 133], and mechanical properties (by means of force measurement) secondarily[27]. The working principle of AFM is based on the forces (attractive or repulsive) interaction between cantilever's tip (probe) and the sample's surface [44]. The main components of a standard AFM is as follows (see 2.10(a)): the cantilever with very sharp tip, optical detection system containing laser light and a position photo detector, scanner, and feedback control loop.
In AFM [85, 145]: initially, the probe comes into contact with the sample through the motion of raster scanning. Next, the reflected laser beam at the back of the probe monitors all movements (lateral and vertical) of the AFM tip due to raised or lowered features of the sample and height adjustments of the scanner by the feedback loop during surface scanning. At the same time, there is a position sensitive photo detector which traces the reflected beam, containing motion of the AFM tip. Lastly, the obtained information is sent to the computer to form topographic image of the sample. There are three major modes available for AFM apparatus: contact, tapping, and non-contact mode [78, 125]. A brief description of the modes is as follows [59]: In contact mode, there is always physical contacts between the AFM probe and the sample in presence of repulsive force and the feedback loop compensates for the constant deflection of the AFM cantilever. However, in non-contact mode ,which the AFM tip oscillates just above the surface in presence of attractive force, and tapping mode ,which the AFM tip has intermittent contact with the surface of the sample in presence of both repulsive and attractive forces, the AFM cantilever is excited at its resonance frequency and the feedback loop maintains constant resonance frequency of the AFM cantilever.
Although AFM is able to operate in different environments such as fluids and vacuum [46, 69], this technique is inherently unable to give information about material identification of the sample. To overcome this drawback, AFM can be combined either with Raman or IR spectroscopy for chemical information of the sample [35, 36, 147] with limitation of micron size particles. Furthermore, AFM is a noninvasive technique which is less expensive compared to TEM and SEM, while it provides comparable resolution in nanometer scale [86].

3

General assessment

The available detection and identification methods which were introduced in chapter 2 possess various pros and cons that cause each method to be powerful in some aspects while suffering from drawbacks in another aspects. Table 3.1 compares the mentioned techniques. Apart from physical or chemical characterizations, which none of the techniques measures the plastic nanoparticles masses, it is noticed that potent microscopic techniques such as AFM, TEM and SEM are expensive and mostly large in size. On the other hand, light scattering techniques suffer from lack of accuracy in polydisperse liquid samples. Similarly, MS spectroscopic related techniques are destructive and light spectroscopy methods are not accurate enough. The mentioned limitations call for a new device which can determine nanoparticle mass and would be inexpensive, accurate and portable, as well as being non-destructive and polydispersity compatible. A suspended microchannel resonator (SMR) which is introduced in chapter 4 can be a wise solution for the observed gap among other methods.

Table 3.1: *Analytical techniques for evaluation of the physical and chemical characteristics of microplastics, nanoplastics and nanomaterials*

Technique	Method	Sample size (Volume\mass)	Minimum particle size, spatial resolution, or particle mass	Advantages	Limitations \Disadvantages	References
FTIR	Spectroscopy	Milligrams	Particle size> $25\mu m$	Chemical characterization Non-destructive Fast and reliable Device size (small) Inexpensive	Physical characterization Detection resolution	[20, 25, 67, 123]
RM	Spectroscopy	Milligrams	Particle size> $2\mu m$	Chemical characterization Non-destructive Fast and easy Device size (small) Inexpensive	Physical characterization Detection resolution	[22, 67, 123] [25]
Pyr-GC-MS	Thermal	low mg	$50nm-\mu m$ Particle size $ng-\mu g$ Particle mass	Chemical characterization No sample preparations	Physical characterization Destructive Long measurement time Device size (large) Expensive	[53, 100, 115] [83, 113]
MALS	Light scattering	few μl	$10nm-1000nm$ Particle size	Physical characterization Non-destructive Low sample Fast and easy Device size (small) Inexpensive	Chemical characterization Polydispersity	[68, 113, 141, 144]
DLS	Light scattering	few μl	$1nm-3\mu m$ Particle size	Physical characterization Inexpensive Low sample Fast and easy Device size(small) Non-destructive	Chemical characterization Large particles Polydispersity	[19, 74, 113] [87]
MS	Spectroscopy	$10^{-9}-10^{-21}$ mol	nm Particle size Particle mass≤ $1MDa$	Chemical characterization Low sample High accuracy Any type of samples	Physical characterization Destructive Device size (large) Only charged particles Expensive	[26, 74, 86] [29, 48, 91, 98]
UV-Vis	Spectroscopy	few μl	$nm-\mu m$ Particle size	Quantitative characterization Inexpensive Device size(small) Non-destructive	Chemical characterization	[50, 120, 137] [4, 8, 96]
SEM	Microscopy	Sub-μg	$1nm-1\mu m$ Spatial resolution	Physical characterization Chemical characterization (by EDS coupling)	Sample preparation Expensive Device size (large)	[68, 95, 133] [25]
TEM	Microscopy	Sub-μg	$>0.1nm$ Spatial resolution	Physical characterization Chemical characterization (by EDS coupling)	Sample preparation Very expensive Device size (huge)	[47, 113, 133] [25]
AFM	Microscopy	Sub-μg	$\approx 0.1nm$ Spatial resolution	Physical Characterization Non-destructive High accuracy Device size (small)	Chemical characterization Complexity Expensive	[86, 110, 133] [25]

4

Suspended Micro-Nanochancel Resonators (SMRs/SNRs)

Nearly three decades ago, micro- and nanomechanical resonators, which could provide high sensitivity for mass sensing, were introduced [15, 39, 57, 132, 146]. These mechanical resonators measure the mass adsorbed on their surfaces by utilizing the natural frequency of the resonators. Blake's [63] publication provides several applications for this method. FEM simulation software e.g. COMSOL can be employed to model these resonators. The dynamics of such cantilever beams including natural frequency and mode shapes have been well determined using either Rayleigh's method or beam's theory in [109] or [17].

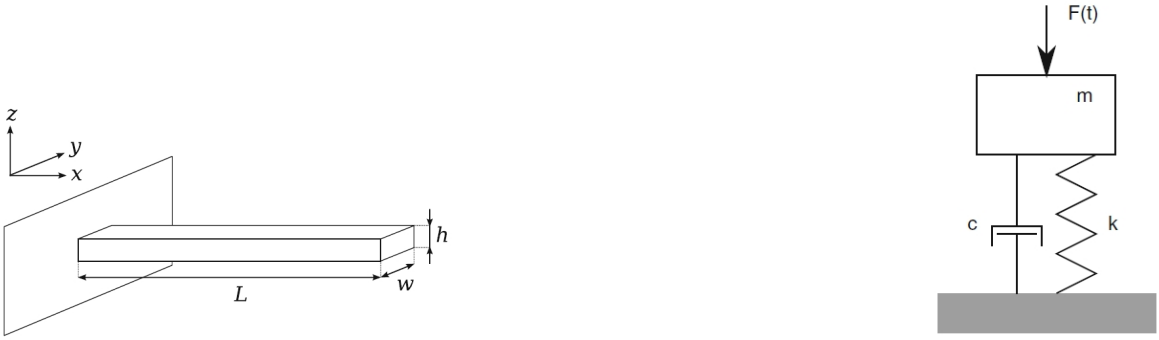

(a) (b)

Figure 4.1: *(a) Schematic of a mechanical resonator [111]. (b) Lumped-element model for clamped-free beams [111].*

A lumped-element model can also be employed to describe behavior of a mechanical resonator. The forced vibration of a cantilever shaped mechanical resonator, shown in 4.1(a), can be modelled with a linear spring, a mass and a linear damping element as depicted in 4.1(b). The equation of motion of this system can be expressed as a second order differential equation which is [112]:

$$m\frac{d^2X}{dt^2} + c\frac{dX}{dt} + kX = F(t) \tag{4.1}$$

Using the Laplace-transform, the transfer function for the total compliance $C_t(s)$ is derived [112]:

$$C_t(s) = \frac{X(s)}{F(s)} = \frac{1}{ms^2 + cs + k} = \frac{\frac{1}{k}}{\frac{m}{k}s^2 + \frac{c}{k}s + 1} = \frac{C_s}{\frac{s^2}{\omega_0^2} + 2\zeta\frac{s}{\omega_0^2} + 1} \tag{4.2}$$

where $C_s = \frac{1}{k}$ is the spring's compliance, $\omega_0 = \sqrt{\frac{k}{m}}$ is the undamped natural frequency and $\zeta = \frac{c}{2\sqrt{km}}$ is the damping ratio. If Equation 4.2 is solved for a free unndamped vibration, the natural frequency will be [112]:

$$\Omega = \sqrt{\frac{k}{m}} \tag{4.3}$$

while the damped natural frequency ($\omega_{d,n}$) and damped resonance frequency ($\omega_{d,r}$) for driven damped vibration are given as [112]:

$$\omega_{d,n} = \Omega\sqrt{1-\zeta^2} \tag{4.4}$$

$$\omega_{d,r} = \Omega\sqrt{1-2\zeta^2} \tag{4.5}$$

From Equation 4.5, it is evident that the resonance frequency is approximately equal to the undamped resonance frequency ($\omega_{d,r} \approx \Omega$) for slight damping.
In order to show the behavior expectation of the system graphically, the amplitude and phase of the system are derived from Equation 4.2 [112]:

$$|C_t(\omega)| = |\frac{X}{F}| = \frac{C_s}{\sqrt{(1-\frac{\omega^2}{\Omega^2})^2 + (2\zeta\frac{\omega}{\Omega})^2}} \tag{4.6}$$

$$\angle X(s)/F(s) = \phi = arctan(\frac{2\zeta\frac{\omega}{\Omega}}{(\frac{\omega}{\Omega})^2 - 1}) \tag{4.7}$$

The dimensionless form of the Equation 4.6 which is called "dynamic gain" is given by [111]:

$$\delta z_0 = |\frac{X}{FC_s}| = |\frac{Xk}{F}| = \frac{1}{\sqrt{(1-\frac{\omega^2}{\Omega^2})^2 + (2\zeta\frac{\omega}{\Omega})^2}} \tag{4.8}$$

Figure 4.2 plots both the amplitude and phase response of a linear resonator.

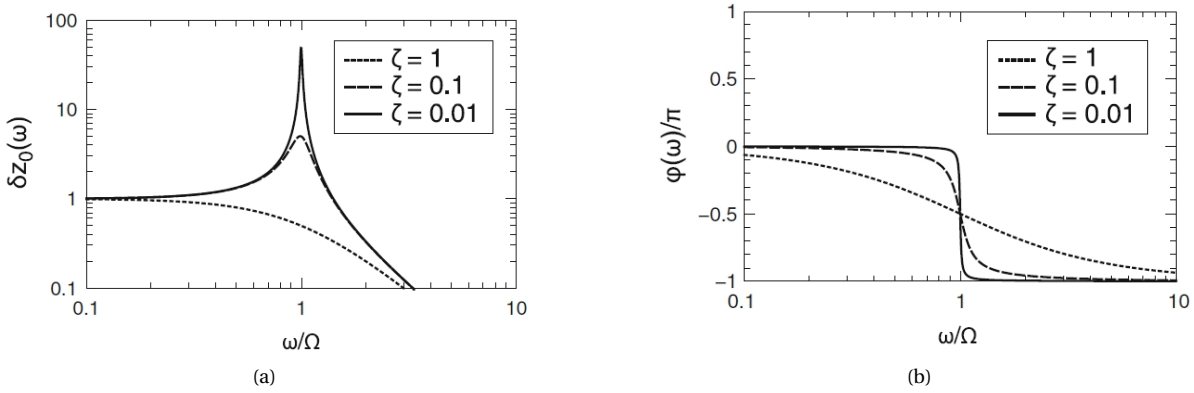

Figure 4.2: *(a) Relative amplitude response of the driven damped system [111]. (b) The corresponding phase response of the system [111].*

To complete our analysis, the quality factor (Q) of the resonator is defined. The quality factor (Q) indicates the sharpness of the resonance peak of resonators in bode plots and can be defined as the ratio between energy stored (W) and energy lost (ΔW) of the system within one operating cycle [111, 112]:

$$Q = 2\pi\frac{W}{\Delta W} = \frac{m\omega_{d,r}}{c} \tag{4.9}$$

Considering Equation 4.5 and knowing $\zeta = \frac{c}{2\sqrt{km}} = \frac{c}{2m\Omega}$ and $\omega_{d,r} \approx \Omega$, mathematical equation for quality factor (Q) is given by [112]:

$$Q = \frac{1}{2\zeta} \tag{4.10}$$

As Equation 4.10 indicates, a higher Q is obtained once lower damping occurs in system. Experimentally, the quality factor (Q) can be determined from the phase response (see 4.2(b)) in which the slope of the phase response at resonance frequency is proportional to the Q [111]:

$$\frac{d\phi}{d\omega} = \frac{2Q}{\Omega} \tag{4.11}$$

Now we return to single mass sensing by mechanical resonators. Since a mechanical resonator is a continuous structure and by knowing Equation 4.3,Equation 4.4 and Equation 4.5, the simplified dynamics of an individual resonance mode is given by [111]:

$$f_n = \frac{1}{2\pi}\sqrt{\frac{k_{eff}}{m_{eff}}} \tag{4.12}$$

where m_{eff} and k_{eff} represent effective mass and effective spring constant of the particular mode respectively. By differentiating f_n of Equation 4.12 with respect to the m_{eff}, a linear approximation for added mass(Δm) is obtained, showing in Equation 4.16:

$$\frac{df_n}{dm_{eff}} = -\frac{1}{4\pi}\sqrt{k_{eff}} \times (m_{eff})^{-\frac{3}{2}} \tag{4.13}$$

and from Equation 4.12 and supposing $m_{eff} + \Delta m \approx m_{eff}$, we have:

$$\sqrt{k_{eff}} = 2\pi\sqrt{m_{eff}} \times f_n \tag{4.14}$$

$$\frac{\Delta f_n}{f_n} \approx -\frac{1}{2}\frac{\Delta m}{m_{eff}} \tag{4.15}$$

$$\Delta m \approx -2m_{eff}\frac{\Delta f_n}{f_n} \tag{4.16}$$

Another important parameter is the mass responsivity (R) which is defined by the change of resonance frequency (Δf_n) as a result of changes in mass(Δm) [39, 111]:

$$R = \frac{\Delta f_n}{\Delta m} \approx -\frac{1}{2}\frac{f_n}{m_{eff}} \tag{4.17}$$

Equation 4.17 clearly shows that a high responsivity is reached by increase in resonance frequency (f_n) and lowering the effective mass (m_{eff}). Knowing system responsivity leads to determination of system sensitivity (SEN) which is inverse of R and it is defined as smallest mass sensing per $1Hz$ frequency shift.
Although mechanical resonators have been greatly successful in gaseous environments, they exhibit overdamped responses in liquid [23]. In liquid, due to fast dissipation of energy which results in lower quality factor (Q) and viscous drag which increases the effective mass (m_{eff}), mass sensitivity and frequency resolution are degraded [9, 23].

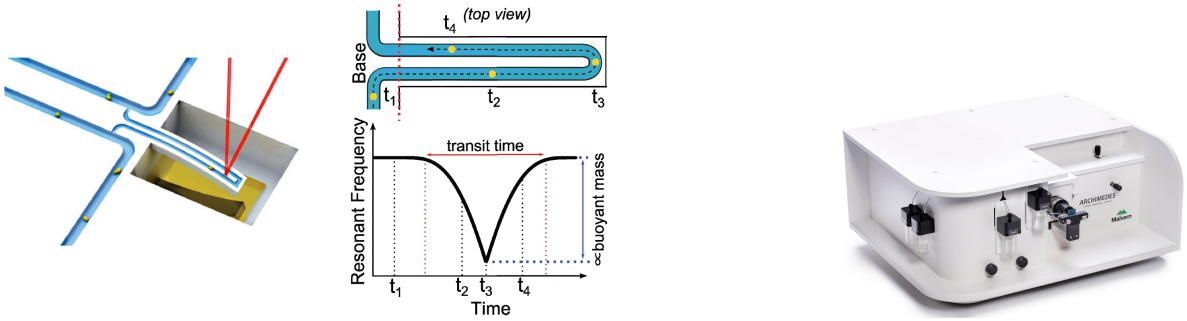

(a) (b)

Figure 4.3: *(a) A simple drawing of Micro-Nanochannel resonator and its operation [92]. (b) Archimedes, an instrument which uses SMR technique for mass measurement [76].*

In 2003, Burg and Manalis introduced a breakthrough to overcome this drawback of micromechanical resonators by implementing a micro fluidic channel inside the resonator. Afterwards, in 2006, this suspended microchannel resonator (SMR) was employed in the vacuum environment, resulting in a quality factor, in the order of 700 [23]. There are two operating modes for SMRs including "affinity-based capture" in which target particles are captured by receptors of the inside walls of SMRs and "flow-through" in which mass measurement is done when target particles pass through the microchannel [9]. In this project, flow through SMRs are only considered. As it has been mentioned, SMRs/SNRs devices are utilized for measuring the mass of particles suspended in liquids [21, 93], as well as fluid properties (density and viscosity) [66]. Literature claims that this technique is able to precisely measure the particle's mass in ranges down to femtogram ($1fg = 10^{-15}g$) by SMRs and atogram ($1ag = 10^{-18}g$) by SNRs for various samples such as nano gold particles [24, 71, 93] and polystyrene beads [49, 88].
The working principle of SMRs/SNRs, like the basic AFM technique in dynamic mode (non-contact and tapping modes, see section 2.10), relies on an oscillating cantilever[70]. In SMRs/SNRs, as 4.3(a) shows, fluid containing particles passes through an embedded U-shape channel which covers the entire length of the suspended micro cantilever. This suspended cantilever can be excited by different mechanisms, e.g. a piezoelectric actuator or electrostatic forces. As soon as a particle enters the U-shape channel, depending on its position inside the channel, the resonance frequency of the cantilever reduces to a minimum in the first half of the way (time t3 in 4.3(a)) and it returns to its previous frequency as particle exits the channel. These changes in resonance frequencies which show themselves mechanically by changes in deflection of the cantilever can be detected by optical systems (e.g. (LDV) Laser Doppler Vibrometer) which focuses on a certain point of the cantilever.
In order to estimate consecutive changes in resonant frequencies leading to particle's mass determination, there a control system is needed. A common architecture is the phase-locked loop (PLL). As 4.4(a) shows, a PLL consists of three elements: a phase detector (PD), a voltage controlled oscillator (VCO) and a loop filter (LF).A phase detector is responsible for comparing the phase of input signal (Φ_i) which is received from SMR

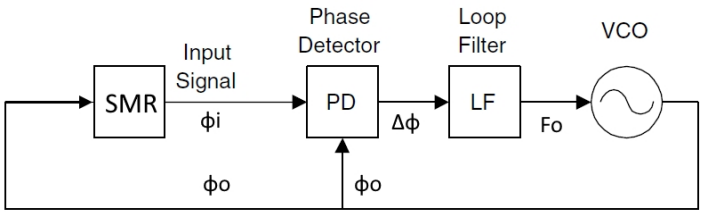

(a)

Figure 4.4: *Block diagram of the SMR with PLL*

and the VCO signal (ϕ_o). This phase difference ($\Delta\Phi$) then is utilized to obtain the frequency difference ($\Delta\omega$) and to control the frequency of the VCO by means of the loop filter (LF). The out put of LF changes the frequency of VCO so that the phase difference between input signal and VCO is kept at the resonance value ($-90deg$).
In chapter 3, it was claimed that this device, which uses a non-destructive method, can detect particles with different masses, implying particles with different sizes. In addition, due to its small size and simple instrumentation, it will be inexpensive as well. However, it only provides the particle mass without indicating chemical composition, leading to miss-interpretation of results when there is no information about the chemical compounds prior to the sample analysis.
Based upon device dimensions and first resonance frequency of our device filled with clean water ($124KHz$), which have been provided by [34], K_{eff}, m_{eff}, responsivity and sensitivity of our device can be determined such that $|R| = 7.74(\frac{Hz}{fg})$ or $S = 12.9(\frac{fg}{Hz})$. It implies that a frequency shift of $\Delta f = -2.15(HZ)$ in the frequency response can be observed if there is a PS spherical particle flowing inside the channel with $\rho = 1.05(\frac{g}{cm^3})$ and diameter of $100(nm)$.

5

Conclusion

5.1. Summary

There are various types of plastics, depending on their synthetic polymers. Basically, nanoplastics are either fabricated purposefully or as a result of microlplastics degradation. The existence of naoplastics has previously been confirmed. Nanoplastics can be toxic due to their chemical nature, their additives and the adsorbed chemicals. The uptake of nanoplastics by organs and immune cells have been proven. However, there is a lack of conducted research about potential toxicity of nanoplastics on human being. There are few techniques available for detection and identification of nanoplastics. Each method owns advantages and limitations. Since each method determines a parameter which differs from the determined parameter by another technique, it is unreasonable to compare them with each other and select the best one. However, from a general perspective, the observed gaps among the explained techniques were identified and an alternative method for bridging those gaps was introduced. The presented alternative was a suspended microchannel resonator which can measure the particle mass. At the same time, SMRs are highly sensitive and small in size. However, "flow through" SMRs suffers from disability of chemical characterization of nanoparticles since they are meant to sense particle mass. Although it seems that physical characterization of nanoparticles without knowing the chemical composition is not very useful or at least when a chemically unknown environmental sample is being analysed, there hopefully could be improvements in the physical characterization techniques in the future so that these techniques also become capable of chemical identification, as there is a hope to improve this technique (SMR) in such a way that allows for particle density determination and possibly chemical identifying in the future. Therefore, this device at the end can find its place among other existing characterization techniques without claiming superiority over others.

5.2. Research questions

Considering that SMR devices have already been used for mass measurement of nanoparticles and by keeping in mind that MNE group of HTE department of TUDelft has already fabricated a microchannel resonator for density measurement of fluids, the aim of this project is to answer the following questions:

- ***Can the fabricated silicondioxide SMR at TUDelft enhanced with the PLL control system detect nanoplastic particles?***

Based upon evidences in literature, our device is likely sensitive enough to detect nanoplastic particles. In case of a positive answer to the first question, the second question which considers the DUT performance will be investigated.

- ***What is the performance of silicondioxide SMR in terms of mass limit detection and maximum detection speed?***

5.3. Approach

In order to answer the research questions, two experiments at least must be accomplished, but before that the fabricated device should be tested in terms of quality factor and resonance frequency. The next challenge is the theoretical design and actual implementation of PLL on a FPGA board and post-processing calculations, leading to visual outputs.

The first question will be answered by conducting two separate experiments in which the frequency responses of clean water and water containing the purchased nanoengineered plastic particles with different sizes circulating inside the channel are observed and then compered. Any shifts in frequency response which are detected by PLL indicate sensitivity of our device to nanaoplastic particles.

The second question involves experiments including circulation of polluted water with various bead's diameter sizes (from few nanometers to micron) inside the channel connected to a PLL and PC for signal processing. Maximum detection speed can either be determined by measuring the time which is needed to detect only one particle or testing our device with specific pollution concentration per specific volume of clean water and measuring the determination time.

If project's time permits, buoyant mass difference between uncoated and coated particles (protein corona) will be investigated as well. This can be done by conducting an experiment by which two mass histograms (one for fluid with bare particles and another one for fluid with coated particles) will be compared to determine the corona mass.

II

Thesis

6

Paper

Precise measurement of a nanoparticle mass in liquid using silicon dioxide suspended microchannel resonators

Nowadays, nanoparticles applications are growing in various industrial fields such as cosmetics and pharmaceuticals. Hence, demand for flow-through characterization techniques, that allow for in-line assessment, are on the rise. The most interesting parameters for in-line assessment are mass and concentration of nanoparticles, that reveal information on yield and aggregation in a solution. The Suspended Micro-channel Resonator (SMR) is a device that can provide precise flow-through mass sensing down to the attogram. Here, we present our findings of a TUDelft made SMR on frequency stability and mass resolution.

1 Introduction

Today, plastic products are involved in many fields from health to textiles and construction. The world plastic production has raised dramatically, from 2 million tons in 1950 to almost 368 million tons in 2019 [4, 5]. Synthetic polymers such as polyethylene (PE), polystyrene (PS), polyurethane (PUR), polypropylene (PP) and polyvinyl chloride (PVC) are the core of plastics. In addition to polymers, additives are added to plastics to enhance their mechanical, chemical and visual characteristics such as strength, fire resistance and colouration [4]. Although the potential toxicity of nanoplastics on humans has hardly been verified, nanoplastics, due to their small sizes, can pass biological barriers to penetrate organs and can move across immune cells [6, 7, 8]. This shows the necessity of studying nanoplastics.

On the other hand, progression of tools for precise identifying and quantifying of nanoparticles (not only nanoplastics but also exosomes, viruses, protein aggregates) suspended in liquids in terms of physical properties is still challenging [9, 15]. There are few approaches available mostly based on scattering light measurements such as MALS and DLS. However, these methods can be prone to errors in polydisperse fluids [16, 17]. Hence, there still is demand for more precise and more efficient techniques for precise characterization of nanoparticles.

The Suspended Microchannel Resonator (SMR) is a MEMS mass sensor which allows for measuring of nanoparticles in a flow-through mode to characterize buoyant mass and concentration of

them [10, 11, 15]. Flow-through mode is based on a cantilever in which a micro fluidic channel has been embedded. The resonator's quality factor (Q) will be maximized as the device is placed into a vacuum environment. The working principle of

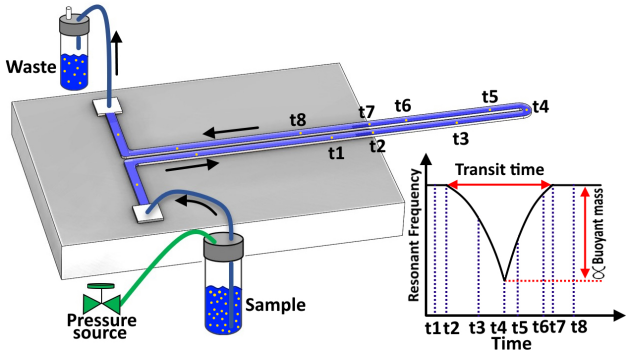

Fig. 1: *A graphic representation of SMR, showing a particle is flowing through eight different positions. On the right, the corresponding frequency shifts made by a particle as it moves from t1 to t8.*

SMRs is as follows (see Fig. 1): As a particle flows inside the cantilever through the micro channel, resonant frequency of the cantilever is modulated. This change in resonant frequency is transient and is according to particle's density which could be higher or lower than that of the carrier liquid, hence resonant frequency decreases or increases respectively. Then this resonance change can be translated into buoyant mass of the particle. Finally, using Archimedes principle, the density of particle can be obtained when weighing particle in fluids with different densities. Given that mass and density are known, volume of particle can be obtained as well [12].
In this paper we aim to obtain the limit of detection or mass sensitivity of silicon dioxide suspended microchannel resonant cantilevers, and the evidence of particle detection is shown.

2 Methods

2.1 Theory

The core of mass sensing by a resonator is based on Eq. (1) which has been derived from the mass-spring equivalent system Eq. (2) [14]. By definition, Δm is the mass change that causes a resonance frequency shift of Δf_n, while k is the equivalent spring constant of lumped system and m_{eff} is the effective mass of a vibration mode and fluid flowing inside.

$$\Delta m \approx -2m_{eff}\frac{\Delta f_n}{f_n} \tag{1}$$

$$f_n = \frac{1}{2\pi}\sqrt{\frac{k}{m_{eff}}} \tag{2}$$

In order to provide consecutive mass determination of suspended particles in fluid flowing through the resonator, resonance frequency of a resonator must be monitored continuously. This can be done by a Phase-Lock Loop (PLL) (see Fig. 2). As PLL will lock the phase of the system, a laplace domain transfer function of the resonator's phase is given in Eq. (3), where $\tau_c = \frac{2Q}{2\pi f_n}$ (Q is the resonator's quality factor and f_n is the resonance frequency of the resonator) is the characteristic time of the resonator, Φ_{in} is the phase of the actuation signal, assumed approximately harmonic and Φ_{out} is the phase of the resonator's response signal [10].

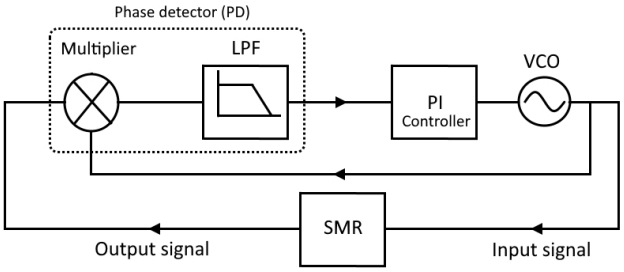

Fig. 2: *Block diagram of the SMR with PLL*

$$\Phi(s) = \frac{\Phi_{out}(s)}{\Phi_{in}(s)} = \frac{1}{\tau_c s + 1} \tag{3}$$

The phase domain model (see Fig. 3) is obtained by replacing the resonator phase transfer function and simplifying other components. Finally,

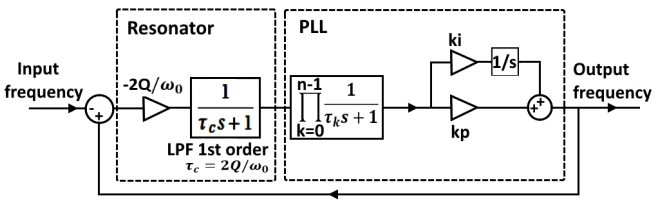

Fig. 3: *Generalized Phase-domain model of the resonator-PLL*

tailoring the desired system response is done by equating the transfer function of the system to a Butterworth filter, that allows for determination of PLL constants (k_p, k_i and τ_k) (see the supplementary notes).

2.2 Experimental setup

A device and its accessories, which can be seen in Fig. 4(a), consists of two major parts: Microfluidic chip and fluidic interface.

2.2.1 Microfluidic chip

The chip had a total of 3040 microns long microfluidic channel, including on-chip and suspended part. The chips were fabricated at the cleanroom facility (Else Kooi Lab) at TU Delft, whose process is described elsewhere [1, 2]. The main fabrication steps are: i) A Si wafer was etched for reservoirs. ii) Another Si wafer was etched for fluidic channels. iii) The two patterned wafers were bonded, oxidized and selectively etched to form the cantilever and remaining microfluidic channels. About 200 devices are fabricated on a wafer. Each chip was manually released from the wafer. The resonator is a U-shaped hollow cantilever and made of silicon dioxide (see Fig. 4(b)). There are two reservoirs on the back side of the chip that connect the hollow cantilever to the outside world. The dimensions of SMR are given in Table 1.

Table 1: *Chip and resonator dimensions*

Parameter	Value (μm)
Resonator total length	408
Gap between the legs (outer)	5.4
Channels width (outer)	11.3
Channels width (inner)	9
Channels height (outer)	3.5
Channels height (inner)	2.5
Chip length	2850
Chip width	1984

2.2.2 Fluidic interface

The fluidic interface was made of $HTM140$ (High Temperature Mold Material), produced using Envisiontec Micro Plus 3D printer with 30 micron resolution. Then, they were ultrasonically cleaned in %99 isopropyl alcohol followed by a 2 min UV curing before using. On the interface, first the needles and later the chip were glued using epoxy adhesive (EA 9492) to the interface. After attaching needles and before gluing a chip on the interface, a supplementary cleaning step was performed to reduce the chances of having blockages in the channels and reservoirs of the plastic interface. This procedure was implemented in the following sequence: i) Injecting ethanol using a syringe via needles multiple times, while the whole interface was already immersed in a beaker of ethanol. ii) Ultrasonic cleaning bath for 5 minutes with low power intensity. iii) Repeating step one while ethanol was substituted with DI water. iv) Repeating step one while ethanol was substituted with Isopropanol. v) Drying the interface and needles using a nitrogen gun. The main function of a fluidic interface was to provide a substrate allowing for fluid exchanges between the chip and fluid reservoir outside the setup. This is done using two reservoirs that must be aligned with two openings on the back side of the chip. These two reservoirs are connected internally to the raised portion on the sides of the plastic interface where two dispensing tips (Nordson, $32GA$) were attached for further connection using TYGON E-LFL TUBING with 0.19 mm inner and 2.03 mm outer diameter.

2.2.3 Fluids

Deionized (DI) water was used solely for the characterization of the cantilever. The DI water was provided by (Elga, Demiwater Purelab Flex) with resistivity of 18.2 MΩ cm, and it was double filtered with 0.2 µm syringe filter to be cleaned from possible existing large contaminations. To measure mass of nanoparticles, two other fluids were prepared using the DI water. These two solutions were obtained by diluting 100 nm diameter gold nanoparticles and 800 nm diameter Polystyrene nanoparticles that were supplied as aqueous suspensions with 0.05 mg mL^{-1} and 10% concentration, respectively. Gold nanoparticles were purchased from nanoComposix and polystyrene nanoparticles were obtained from Sigma-Aldrich Chemie. Both gold and polystyrene nanoparticles

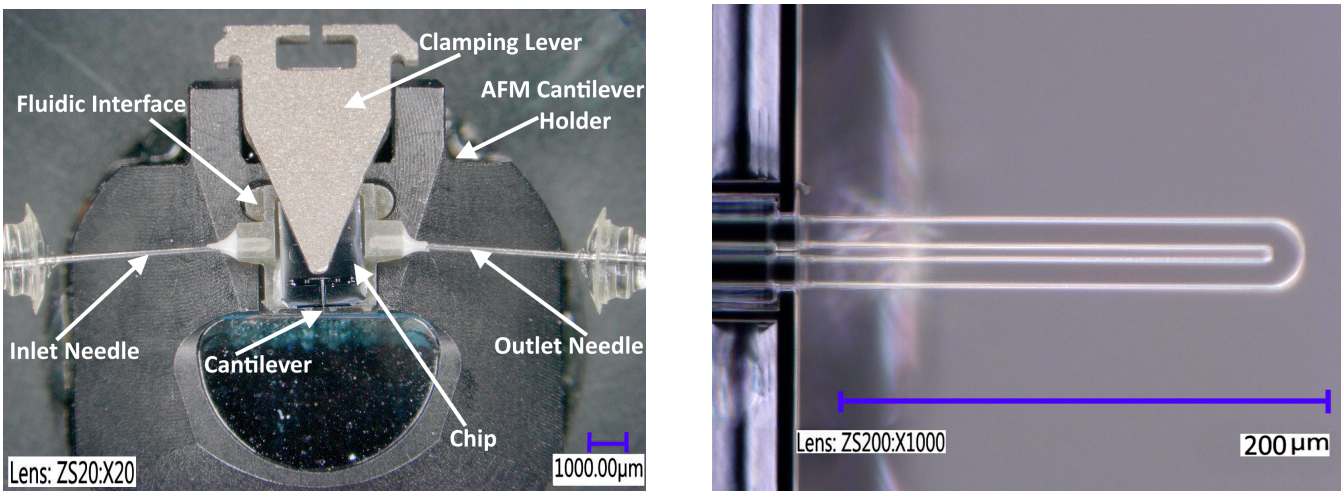

(a) (b)

Fig. 4: *(a) A chip containing a resonator, glued to an interface with needles, mounted on a Nanosurf AFM cantilever holder and clamped. (b) Top view of the U-shaped silicon dioxide resonator.*

were suspended in DI water before dilution. For conducting experiments, 5 mL of the mentioned solutions with a concentration of 1.022×10^7 particles mL^{-1} was provided in advance. This concentration was one order of magnitude lower than the concentration that can provide one particle per volume of the cantilever. By this, the probability of having two or more particles simultaneously in the suspended channel is small.

2.3 Experiments

Modal analysis was performed to characterize the empty and water-filled resonator. Next, by employing a Phase-Locked Loop, frequency changes over time were recorded.

2.3.1 Modal analysis

The sample including a chip, interface and two needles was mounted on an AFM cantilever-holder from Nanosurf (see Fig. 4(a)). The AFM cantilever-holder provided clamping by a clamping lever and excitation by an embedded piezoelectric. Next, the AFM holder was placed inside a vacuum chamber with four connection slots (one for excitation signal, two for vacuum pump and its sensor and one for solution's inlet and outlet). Finally, a laser Doppler vibrometer (Polytec MSA-400-PM2-D), including function generator, scanning head, decoder and a PC, was employed to identify the resonance frequencies and evaluate quality factors. A Pseudo random signal was selected to excite the piezoelectric material. This signal has nominally a constant power in frequency domain, therefore all the frequency range of interest is excited. The measurement laser beam was adjusted on the cantilever by looking through the microscope on the vibrometer. The Vibrometer can detect only out of plane motions and modes. Next, the optical signal was decoded and processed to an electrical analog signal which is proportional to either velocity or displacement depending on the decoder used. Then, it was digitized and sent to the PC where the modes and spectrum are visualized. A schematic of this experiment is shown in Fig. 5.

2.3.2 Phase-Locked Loop (PLL)

Initially, experiments were performed to investigate frequency stability, and to track frequency changes leading to single particle's mass detection. The mounted resonator on the AFM holder was placed into the vacuum chamber to which excitation signal, fluids input and output tubes, vacuum hose and pressure sensor were connected. The laser Doppler vibrometer (PolytecMSA-400-PM2-D) was used for optical signal decoding into analog signal, and a UHFLI (600 MHz) Lock-in Amplifier from Zurich Instruments) was employed for the PLL implementation. The lock-in pro-

vided a sinusoidal excitation signal until 1.5 V that allowed detection until the onset of nonlinearity in the cantilever resonance. To avoid saturating the input of the lock-in, a 10 dB attenuator was used between the vibrometer decoder and the lock-in. A schematic of this setup is shown in Fig. 5.

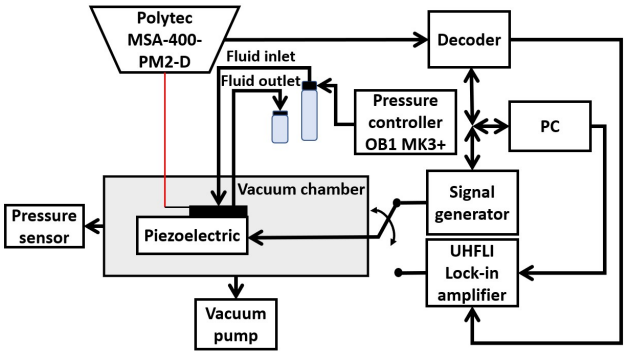

Fig. 5: *Schematic of the measurement setup. For modal analysis the actuation signal is generated by internal signal generator of the vibrometer. However, in phase-locked loop mode, the internal Zurich UHFLI instrument's oscillator excites the piezoelectric.*

To lock the phase at resonance, initially, several frequency sweeps with varying actuation power around specific resonance frequencies were performed until the onset of nonlinear regime. Next, required parameters for a PLL circuit such as quality factor (Q), resonance frequency and phase value at resonance were recorded. Then, a PLL circuit was made (see the supplementary notes). Ultimately, by applying PLL, a phase and frequency measurement over a period of 5 minutes was performed and recorded.

2.4 Data processing

To characterize the resonator in terms of stiffness (k), effective mass (m_{eff}) and quality factor (Q) in both empty and filled cases, the following steps were taken.
Quality factors were measured experimentally using both 3dB and phase slope techniques. Given that the displacement Power Spectral Density spectrum (PSD) of the resonator was measured using the vibrometer (It was obtained by an experiment, performed similar to modal analysis with two major differences: i) no excitation signal was involved, and ii) the displacement PSD in ($m^2\,Hz^{-1}$) versus frequency was measured instead), k and m_{eff} were obtained by [18]:

$$k = \frac{4K_BTQ}{\omega_r PSD(\omega_r)} \tag{4}$$

$$m_{eff} = \frac{k}{\omega_r^2} \tag{5}$$

Where T is the temperature in kelvin, K_B is Boltzmann's constant in joule per kelvin, ω_r is the resonance frequency and $PSD(\omega_r)$ is the power spectral density of the resonator displacement evaluated at the resonance frequency.
To investigate frequency stability, Allan deviation (σ_y) was computed for the specific gate times (τ) with M number of periods as following [19]:

$$\sigma_y(\tau) = \sqrt{\frac{1}{M}\sum_{k=0}^{M-1}\frac{(\overline{y}_{k+1}-\overline{y}_k)^2}{2}} \tag{6}$$

Where $\overline{y}$ is averaged fractional frequency. The theoretical Allan deviation of thermomechanical noise was also computed by [20]:

$$\sigma_y(\tau) = \sqrt{\frac{m\omega_r k_B T}{{A_0}^2 Q^3 \tau}} \tag{7}$$

Where A_0 is the applied force at resonance.
And Eqs. (6) and (7) were related to limit of mass detection by [21]:

$$\delta m \approx -2m_{eff}\sigma_y(\tau) \tag{8}$$

After frequency over time measurement with a liquid solution containing nanoparticles was done, unwanted frequency variations over time were eliminated by a finite impulse response (FIR) high-pass filter with 10 Hz bandwidth.

3 Results and discussion

3.1 Resonator characterization

Characterization was done when the resonator was empty and when it was filled with water. In case of water-filled cantilever, DI water was driven by 70 mbar pressure difference. It was noticed that there are various cantilever's filling times from a small fraction of 1 s to 25 s under the

same pressure difference. This indicates the existence of different resistance magnitudes in front of the flow in every single tested device. This could be either due to manual gluing of the chip and interface, which would cause partial blockage of inlet or outlet of reservoirs on the interface, or due to residues in channels during fabrication of micro-channels that would lead to non-uniform internal surfaces of the channels. Fig. 6 shows a cantilever fluid flow inside the SMR.

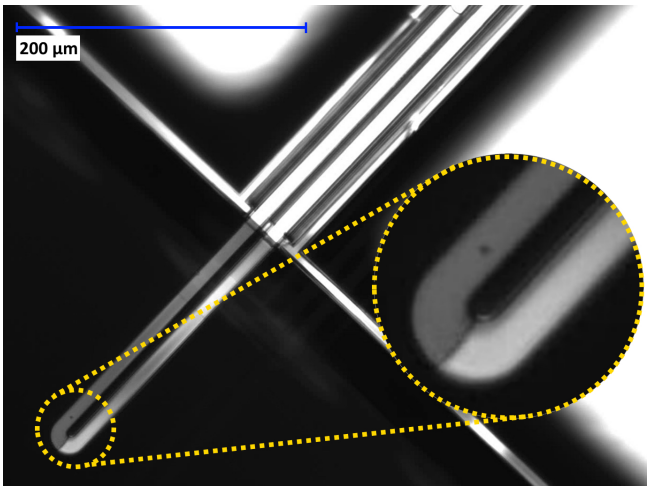

Fig. 6: *Suspended hollow cantilever being filled with liquid from left-leg to right-leg. (See supplementary notes). In the zoomed inset, the darker section is the water-filled section.*

Furthermore, in a frequency range up to 2 MHz, for both empty and water-filled cantilever, three modes were identified in a vacuum environment of 0.012 mbar using Polytec vibrometer. All modes occurred at frequencies below 1 MHz, including two bending modes and one torsional mode (see Fig. 7). There might be higher modes between 1-2 MHz, however due to their low amplitudes, they were hidden in the base line of spectra. In the frequency spectra, several other spikes were also observed. These peaks, which correspond no mode shapes, can be considered as rigid body motions of the cantilever or its base, since the actuation is provided by a piezoelectric and there is a clearance, albeit very slight, between the interface and its holder, hence we do not know about the exact place of actuation, the way that excitation energy is absorbed and how this energy is released to the cantilever. Therefore, these spike frequencies might change from time to time without showing any vibration modes.

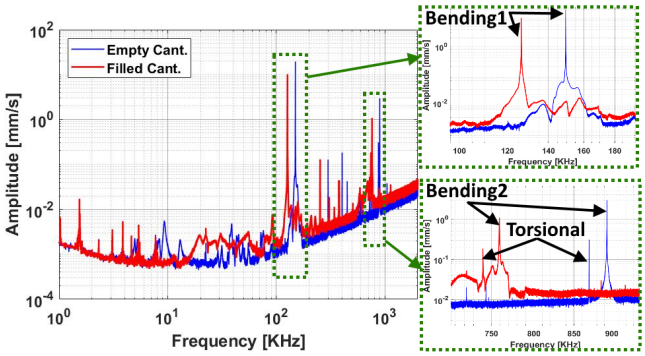

Fig. 7: *Complete spectra of the empty and water-filled resonator up to 2 MHZ*

Comparing both two spectra, it was also observed that the base line of the water-filled cantilever was slightly higher in amplitude beyond 10 kHz. As these spectra were obtained in different days (the device was dismounted from the setup and mounted several days later), this can be explained by the same mentioned reasons earlier in this section. The Important parameters of the detected modes are shown in Fig. 8.

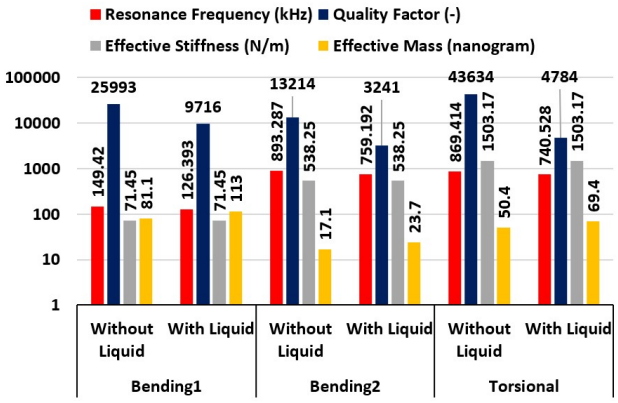

Fig. 8: *Summary of the resonator's parameters for different modes, obtained from the modal characterization experiment.*

In terms of resonant frequency, the water-filled resonator experienced a reduction of 23 kHz, 134 kHz and 129 kHz for bending 1, bending 2 and torsional mode respectively. These shifts in resonance frequencies are mainly due to the increase in effective mass of water-filled cantilever, which is inversely proportional to the resonance frequency. The predicted values from COMSOL simulation (see supplementary notes) of the resonance frequencies (112.24 kHz, 674.45 kHz and 698.54 kHz) are lower than of that obtained experimentally for empty cantilever. This discrepancy

is attributed to different value of Young's modulus or due to possible discrepancy in thickness of cantilever, which might be slightly non-uniform as a result of the fabrication process.
In terms of quality factors, torsional mode in the empty case showed the highest and bending 2 the lowest. This reduction of quality factor from bending 1 to bending 2 is in accordance with previous work on this device [13]. Moreover, significant drops (62.6%, 75.5% and 89% in bending 1,2 and torsional mode respectively) were noticed in case of water-filled cantilever compared to empty. The effective mass increased for each mode of water-filled compared to those of empty one. This was expected as water's mass was added to cantilever's mass.

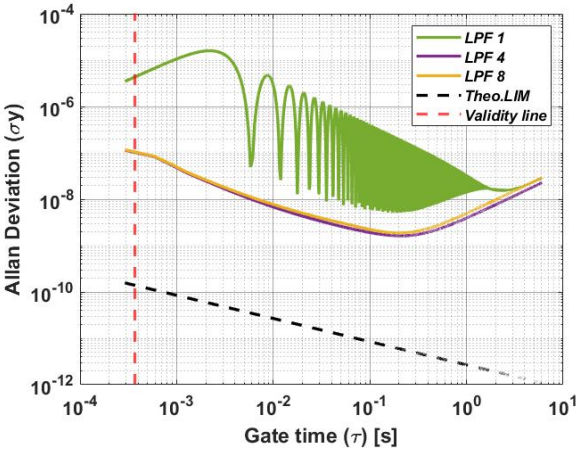

Fig. 9: *Fractional frequency Allan deviation for the empty cantilever operated at the first bending mode.*

3.2 Frequency stability

A PLL as described in Section 2.3.2 was implemented with PLL bandwidth (f_{PLL}=1000 Hz), PLL low-pass filter bandwidth (f_{LPF}=1414 Hz), sampling frequency (f_s=3.598 kHz) and K_p, K_i that are available in the supplementary notes.
We first obtained the experimental fractional frequency Allan deviation for the empty cantilever operated at the first bending mode with low-pass filter orders 1,4 and 8 (LPF1, LPF4 and LPF8). This is illustrated in Fig. 9. The validity line shown in red-dashed line specifies the maximum obtainable sample rate of our system. In other words, the validity line specifies the detection speed of system. This speed is 0.37 ms for 1000 Hz bandwidth, used in Fig. 9.
It was observed that in the validity region $\tau > 2.33/\omega_{PLL}$ [3], indicated by the red-dashed line in Fig. 9, the Allan deviation curve, associated with the system with LPF1, intensively oscillates over τ (see the green line in Fig. 9). These fluctuations are mainly due to inefficient low pass filtering in the demodulator, that was insufficient to remove $2\omega_r$ term from the signal out of the multiplier (see Fig. 2). Furthermore, comparing the systems with LPF4 and LPF8, it was observed that the σ_y changes over gate times are very similar. Hence, LPF1 and LPF8 were excluded from further analysis.
To compare empty and water-filled resonators, the Allan deviation curves are then represented in Fig. 10 for the already mentioned system parameters. The measured Allan deviations of empty and water-filled cantilever in all modes demonstrate similar trends. It is observed that there are continuous reductions in σ_y until a gate time between 20 ms and 400 ms, where the minima are reached in case of empty and water-filled resonator respectively. In both cases, Allan deviations at minima have almost the same magnitude in the first and second bending modes (bending 1 shows slightly smaller Allan deviation). These minima values are approximately one order of magnitude larger (amount of noise is higher) in case of torsional mode compared to first and second bending modes. By passing the minima, the curves thereupon follow a positive slope in case of first and second bending mode, while almost a zero slope is seen in torsional mode.
The zero slope in Allan deviation is an indication of having $1/f$ noise (flicker frequency or pink noise), while a positive slope is mostly attributed to the thermal drift which is defined as slow variations of temperature induced to the device. This thermal drift is dominant just after the minima (right side of minima) in the first and second bending modes, and causes earlier rise of Allan deviation in case of water-filled compared to the empty one. The curves, however start converging in long gate times around 1 s, implying the existence of the same amount of thermal drift at long gate times.
Another type of noise, that shows a slope of approximately -0.5 in Allan deviation graph (thus

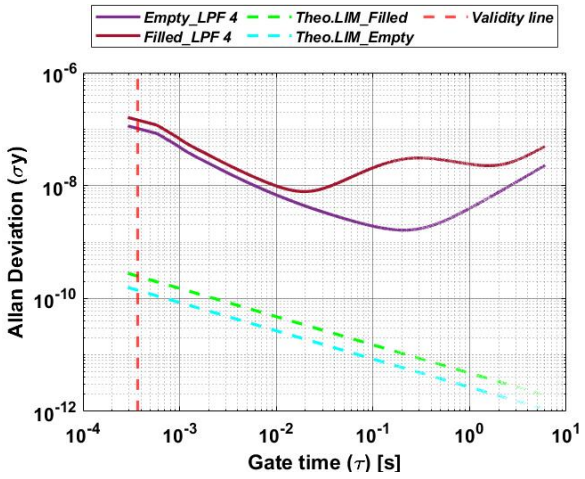

(a) Bending1

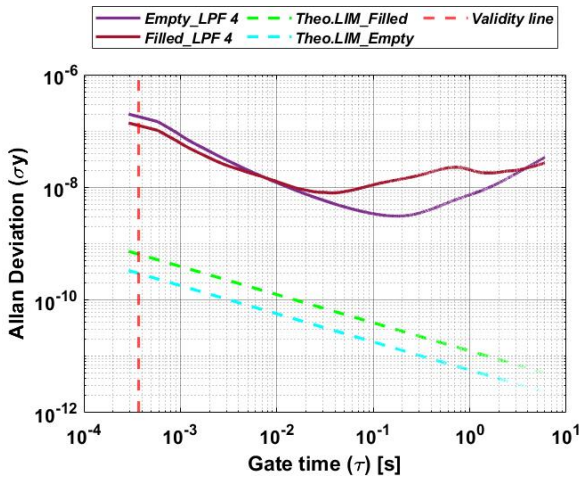

(b) Bending2

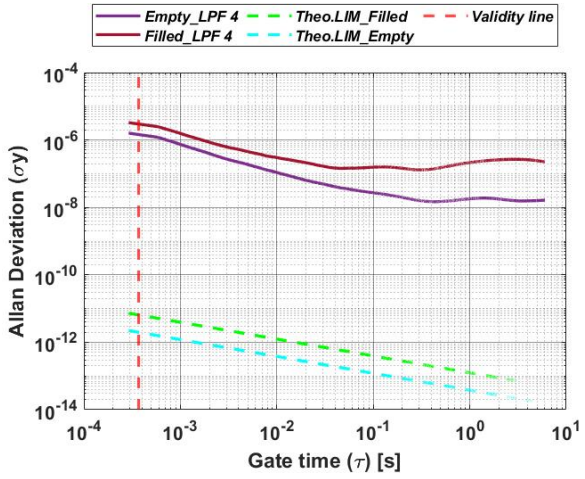

(c) Torsional

Fig. 10: *Fractional frequency Allan deviation for (a) Bending 1 mode, (b) Bending 2 mode and (c) Torsional mode. The right side of validity line (red-dashed) belongs to frequency noise and is determined by ($2.33/\omega_{PLL}$). The blue-dashed and green-dashed lines show the minimum Allan deviation that can be achieved theoretically by our system.*

it is white noise), is the thermomechanical noise. Thermomechanical noise is defined as random vibrations of a mechanical device due to thermal motion of the particles that form it. This noise will exist even if all other types of noise are removed from systems. Therefore, this noise determines the fundamental Allan deviation for our device (Green and blue dashed lines in Fig. 10). From Fig. 10, we notice that there is almost two orders of magnitude discrepancy between thermomechanical limit curves and their corresponding experimental curves in the first and second bending modes. This discrepancy becomes more conspicuous in torsional mode, where there is five orders of magnitude difference. This means that there is another noise source in short gate times that is larger in magnitude than the thermomechanicl noise of the system. In other words, the Allan deviations (in empty and water-filled cases) became limited by the same source of noise in short gate times (left sides of minima), that we call it instrument noise. This instrument noise could be either from the vibrometer or the lock-in amplifier.

3.3 Mass resolution

To address and compare minimum detectable buoyant mass over gate time for an empty and for a water-filled resonator, Allan deviation graphs obtained in Section 3.2 were translated into mass limit of detection, shown in Fig. 11. The smallest detectable masses by modes are given in Fig. 12(a), and equivalent gold and polystyrene particles diameter are seen in Fig. 12(b).

Comparing both cases, the lowest mass detection limit is achievable by the second bending mode, first bending mode and torsional mode respectively. In addition to that, the empty resonator is capable to sense smaller masses compared to the water-filled resonator in almost all gate times. It is noted, however, that we could have obtained better mass resolution if we had recorded data in presence of only thermomechanical noise (dashed lines in Fig. 11) in short gate times for both cases.

Looking at the numbers, in case of empty resonator, the lowest mass detection limits are 0.11 fg, 0.26 fg, 1.49 fg for the second bending

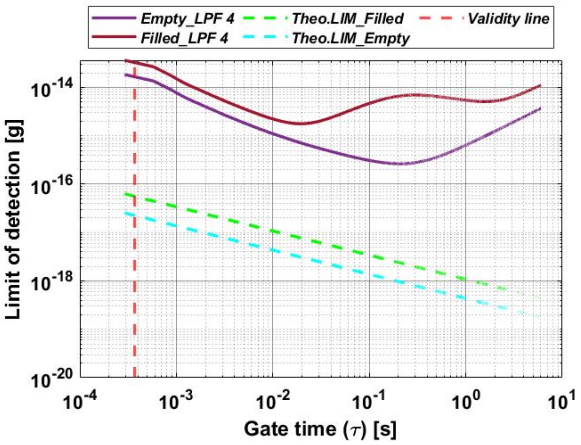

(a) Bending 1

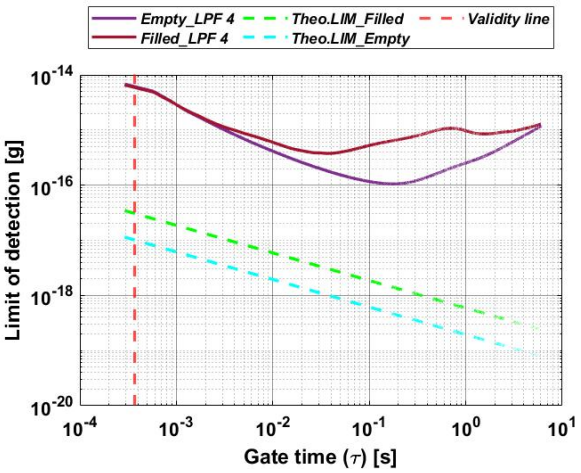

(b) Bending 2

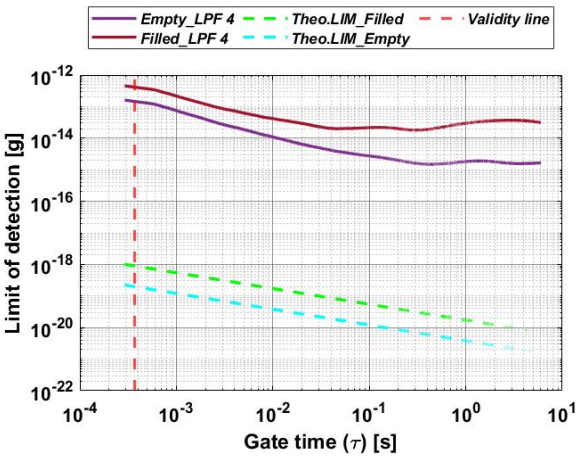

(c) Torsional

Fig. 11: *Comparison among different modes of water-filled and empty cantilever in terms of lowest buoyant mass detection with a PLL with LPF order 4*

mode, the first bending mode and torsional mode, respectively. This detection can be performed at averaging times between 200 ms to 400 ms (for different modes). However, in case of water-filled resonator, the lowest mass detection limit is achievable by the second bending (0.38 fg or 380 ag), first bending (1.75 fg) and torsional (20 fg) mode respectively. This detection can be performed at shorter gate times compared to the empty case, that is between 20 ms to 40 ms.

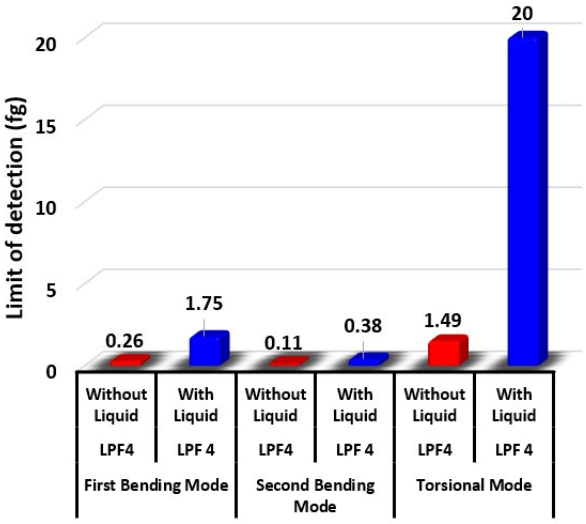

(a)

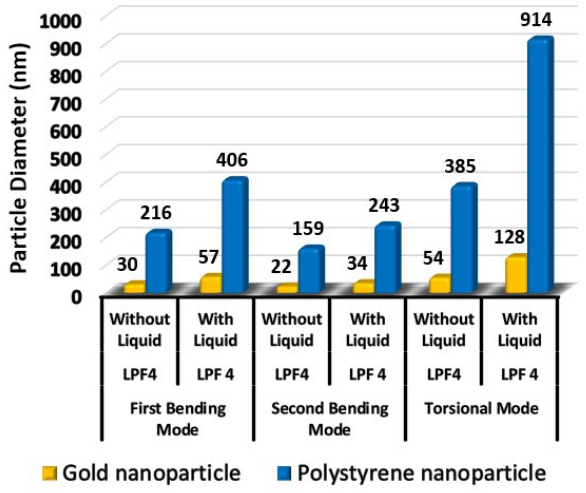

(b)

Fig. 12: *(a) Comparison among different modes with LPF order 4 in terms of smallest detectable mass in* fg.*(b) Summary of the smallest detectable equivalent spherical particle's diameter for gold and polystyrene nanoparticles by different modes.*

3.4 Introducing nanoparticles into resonator

To assess the particles mass detection ability of our system, two liquid samples containing gold and polystyrene nanoparticles were used. In case of gold nanoparticles, two different driven pressure differences were tested using the first bending mode, and in case of polystyrene nanoparticles, three different driven pressure differences were tested using the second bending mode. In this section, we present a result with gold nanoparticles solution flowing for only one value of pressure difference (500 mbar). The results for other cases can be found in the supplementary notes.

Using the described PLL systems with bandwidth 100 Hz and low pass filter order 4, the resonance frequency was recorded for a period of 300 s. To target the limit of detection in bending 1, the obtained data points were averaged on 5 ms (see Fig. 11(a)). The chosen f_{PLL} provides 3.7 ms detection speed, which is faster than selected averaging time (5 ms) for this experiment. The evolution of the resonant frequency with time can be seen in Fig. 13, along with the phase shift introduced by the resonator, where 0 corresponds to the phase shift at resonance. Sudden changes in the resonance frequency produce deviations in the phase from 0 (see the spikes of lower graph in Fig. 13), that the system rapidly corrects. It is evident that resonance phases were locked efficiently during experiments, as the base line of phase shift remained almost invariable regardless of spikes that stand for events corresponding to resonance frequency shifts.

Furthermore, frequency shifts are observed which were not present in the previous situation that liquid was only DI water that was driven by lower pressure difference (see Fig. 14). Some of this variations belong to the flow of particles or aggregate of particles through the cantilever that demonstrate expected peak profile shape (a frequency shift shape that a particle makes when flowing through the hollow cantilever) and will be later used for the determination of particles masses (see red profiles in Fig. 15). These mostly small peaks are almost invisible (large ones are visible) in Figs. 13 and 14. This result shows the suitability of the system to detect spherical gold particles of 130 nm in diameter as we discuss later.

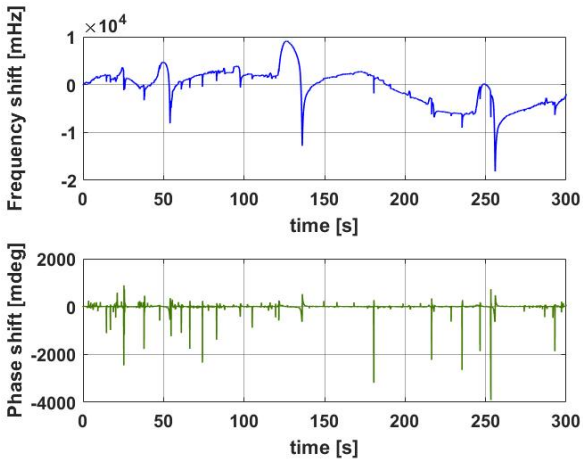

Fig. 13: *Frequency shifts (upper) and Phase shifts (lower) of 5 minutes measurements of an aqueous solution containing 100* nm *gold nanoparticles with* f_{PLL} = 100 Hz*, LPF order 4 and averaging time of* 5 ms*.*

In addition to small frequency shifts, there are some other extreme frequency variations that are repeated regularly over time (the large peaks seen in Fig. 14). These drastic variations start with a considerable rise to reach a peak, then it is followed by a rapid plunge to a minimum and rises again (see an example of them in Fig. 16). This type of frequency changes were observed in the second mode as well (see supplementary notes). It is remarkable that they were repeated more frequently by increase the pressure difference of the flowing fluid (see supplementary notes). To address the reason of these changes, three possible hypotheses were considered: i) passing large aggregates of particles, ii) temperature drift, and iii) over pressure in the cantilever.

To answer them, firstly, they cannot be a frequency shift profile of large or slow moving particles, since they have similar profiles for the first and second bending modes, whilst they must be different. Secondly, they are not temperature drifts, since there were no such abnormal peaks when the sample solution was solely DI water, while the two solutions equilibrated for one hour with ambient temperature (21 °C). The third hypotheses might be the case, since the number of such variations raised when the driven fluid pressure increased. To explain this, suppose somewhere on the internal passage is partially clogged or the outlet reservoir is not able to flow the

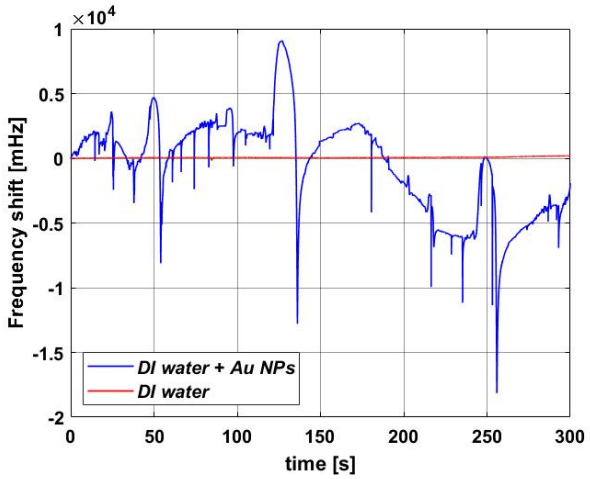

Fig. 14: *Comparison of frequency shifts between when the aqueous solution was only DI water with 70 mbar pressure difference (red) and when the aqueous solution was DI water and gold nanoparticles of 100 nm with 500 mbar pressure difference (blue)*

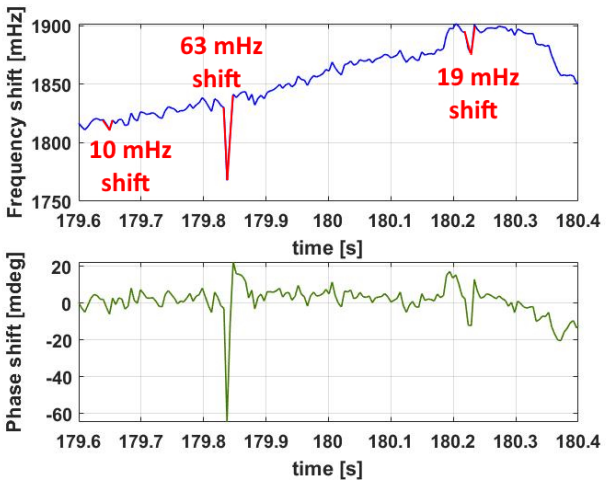

Fig. 15: *The visually detected frequency shift profiles of particles, that are distinguished from noises for an interval of less than 1 second of the experiment's duration time. The large peaks are surely particles, however detecting small peaks are prone to errors due to being in the range shifts of noise. Therefore the 10 mHz shift on the left side could be noise.*

liquid uniformly, then fluid does not flow unless pressure is built-up to remove that clog. As soon as the clog is cleared, the channel experiences a brief moment of underpressure. This shift in pressure differences might induce pulsating stress on the cantilever, leading to changes in Young's modulus and changes in the resonance frequency.

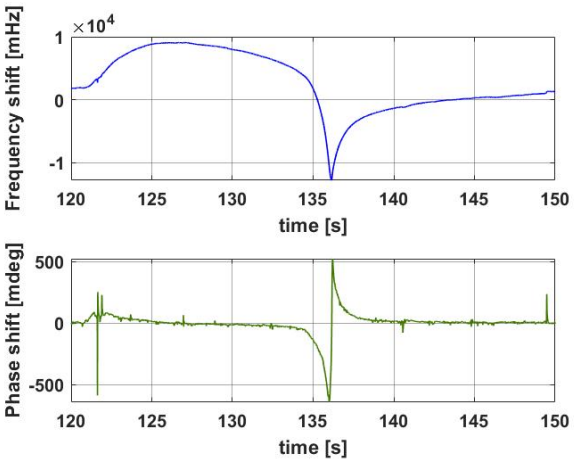

Fig. 16: *The zoomed representation of a drastic frequency variations happened between t=120 to 150 in terms of both frequency and phase shifts. None of them resembled particle's profile shift.*

Another possible explanation can be the change in frequency due to momentum impact caused by over pressure and under pressure that were explained above. This momentum impact can have influence on the vibration of cantilever, shown itself as large peaks that are stabilized over time. However, this needs to be investigated more in the future.

For the observed frequency shifts, we attribute fast changes to nanoparticles and slow changes to pressure fluctuations inside the channel. To remove the latter, we applied a high-pass filter of 10 Hz cutoff frequency to the data. A comparison between filtered and unfiltered data is shown in Fig. 17.

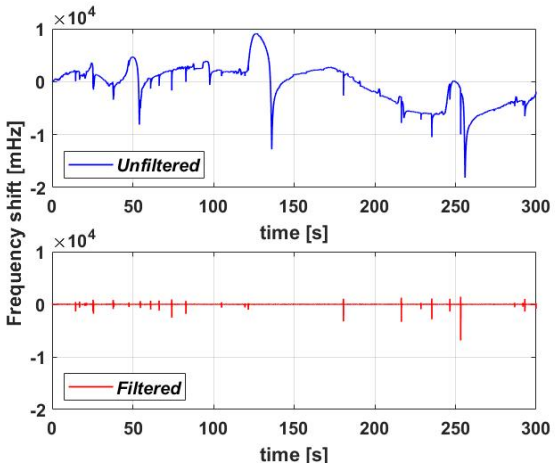

Fig. 17: *A low pass filter of 10 Hz was able to refine unfiltered data (blue) into (red) smooth one.*

As soon as unwanted frequency variations were filtered, the smooth frequency shifts over time were monitored to find distinguished peak profiles. Some indications of flowing nanoparticles with their calculated masses are shown in Fig. 18. It was noticed that the smallest distinguished frequency shift was −10 mHz, which is equivalent to a gold nanoparticle of 130 nm (a buoyant mass of 21.2 fg), (A particle with 70 nm to 130 nm diameter can be considered as a single particle, because of diameter variations among particles of 100 nm nominal diameter according to manufacturer). This is less than two folds of expected smallest detectable gold nano particle's diameter using the first bending mode with f_{PLL}=100 Hz at 5 ms gate time (According to Fig. 11(a), 3.5 fg buoyant mass, which is equivalent to a gold nanoparticle of 71 nm in diameter, was expected to be measured). This degradation in mass limit detection is understandable, since there was a seven days gap between conduction of Allan deviation experiment and mass detection experiment performing, that might have caused increase in effective mass of the used device, resulting in lower sensitivity.

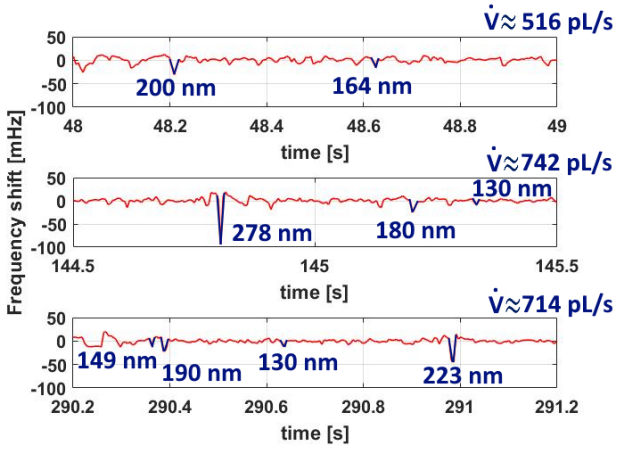

Fig. 18: *Few examples of detected masses with their equivalent particle's diameters in different one second periods of time, and the current flow rate $\dot{V}$.*

4 Conclusion

In this work, we presented frequency stability and mass detection limit of the silicon dioxide suspended micro channel resonators. In terms of frequency stability, in short gate times ($\tau < 20$ ms in water-filled case and $\tau < 200$ ms in empty case), the system's stability was limited by instrument noise in all three modes. However in long gate times, thermal drift and flicker noise were dominant in bending modes and torsional mode respectively.

In terms of mass detection limit, the best mass resolutions were obtained by the second bending mode, first bending mode and torsional mode respectively. The lowest resolved mass for an empty and a water-filled resonator using second bending mode was 0.11 fg and 0.38 fg respectively, for a PLL bandwidth of 1000 Hz that corresponds to a system settling time of 0.37 ms.

We then tried to prove it experimentally by implementing a Phase-Locked loop for a system bandwidth of 100 Hz, and we succeeded to measure mass of 21.2 fg which is an equivalent gold nanoparticle of 130 nm in diameter.

We envision that ultimately our sensor will be capable of measuring mass of nanoparticles continuously, precisely and robustly if the following steps would taken: i) A new chip must be fabricated (new fabrication methods) that allows for working continuously without fractures in it earlier than applying flow driven pressure, ii) equipping a sensitive flow rate sensor in the range of (pL/s) that provides regulating fluid flow smoothly and iii) applying matched filter methods that allows for automatic peak detection in a continuous measurement.

REFERENCES

[1] Perez Garza, H.H. *"Development of Nanotools for Applications in (sub-)Femtofluidics and Graphene Technologies,"*Doctoral thesis, Department of Precision and Microsystems Engineering, Faculty of Mechanical, Maritime and Materials Engineering, Delft University of Technology, Delft,2015.[Online].Available: `https://doi.org/10.4233/uuid:ca9e559b-ec04-4d4f-ac52-bf94b2e901e4`

[2] Heuck, F. C. *"Developing and Analysing sub-10 μm Fluidic Systems with Integrated Electrodes for Pumping and Sensing in*

*Nanotechnology Applications,"*Doctoral thesis, Department of Precision and Microsystems Engineering, Faculty of Mechanical, Maritime and Materials Engineering, Delft University of Technology, Delft,2010.[Online].Available: http://resolver.tudelft.nl/uuid:f1eaec5d-29fe-4424-b8f4-9d6d9e49985a

[3] T. Manzaneque, P. G. Steeneken, F. Alijani and M. K. Ghatkesar, *"Method to Determine the Closed-Loop Precision of Resonant Sensors From Open-Loop Measurements,"* in IEEE Sensors Journal, vol. 20, no. 23, pp. 14262-14272, 1 Dec.1, 2020, doi: 10.1109/JSEN.2020.3008557.

[4] R. Geyer, J. R. Jambeck, and K. L. Law, *"Production, use, and fate of all plastics ever made"*, Science Advances, vol. 3, no. 7, 2017. doi: 10.1126/sciadv.1700782. eprint: https://advances.sciencemag.org/content/3/7/e1700782.full.pdf. [Online]. Available:https://advances.sciencemag.org/content/3/7/e1700782.

[5] P. Europe, *"Plasticsthe facts 2020, An Analysis of European Latest Plastics Production,Demand andWasteData"*,2019. [Online]. Available:https://www.plasticseurope.org/download_file/force/4261/181.

[6] H. Bouwmeester, P. C. H. Hollman, and R. J. B. Peters, *"Potential health impact of environmentally released micro- and nanoplastics in the human food production chain: Experiences from nanotoxicology"*, Environmental Science & Technology, vol. 49, no. 15, pp. 8932–8947, 2015, PMID: 26130306. doi: 10.1021/acs.est.5b01090. [Online]. Available:https://doi.org/10.1021/acs.est.5b01090.

[7] M. Revel, A. Chtel, and C. Mouneyrac, *"Micro(nano)plastics: A threat to human health?"*, Current Opinion in Environmental Science & Health, vol. 1, pp. 17–23, 2018, Micro and Nanoplastics Edited by Dr. Teresa A.P. Rocha-Santos, ISSN: 2468-5844. doi:https://doi.org/10.1016/j.coesh.2017.10.003. [Online]. Available:http://www.sciencedirect.com/science/article/pii/S2468584417300235.

[8] R. Lehner, C.Weder, A. Petri-Fink, and B. Rothen-Rutishauser, *"Emergence of nanoplastic in the environment and possible impact on human health"*, Environmental Science & Technology, vol. 53, no. 4, pp. 1748–1765, 2019, PMID: 30629421. doi: 10.1021/acs.est.8b05512. eprint: https://doi.org/10.1021/acs.est.8b05512. [Online]. Available:https://doi.org/10.1021/acs.est.8b05512.

[9] Kim, H.-A.; Seo, J.-K.; Kim, T.; Lee, B.-T. *"Nanometrology and its perspectives in environmental research"*. Environ. Health Toxicol. 2014, 29, No. e2014016.

[10] Selim Olcum, Nathan Cermak, Steven C Wasserman, and Scott R Manalis. *"High-speed multiple-modemass-sensing resolves dynamic nanoscale mass distributions"*.Nature communications, 6(1):1–8, 2015.doi: https://doi.org/10.1038/ncomms8070.

[11] S. Olcum, N. Cermak, S. C. Wasserman, K. S. Christine, H. Atsumi, K. R. Payer, W. Shen, J. Lee, A. M. Belcher, S. N. Bhatia, and S. R. Manalis, *"Weighing nanoparticles in solution at the attogram scale"*, Proceedings of the National Academy of Sciences, vol. 111, no. 4, pp. 1310–1315, 2014, ISSN: 0027-8424. DOI: 10.1073/pnas. 1318602111. eprint: https://www.pnas.org/content/111/4/1310.full.pdf. [Online]. Available: https://www.pnas.org/content/111/4/1310.

[12] A. K.Bryan, V. C. Hecht, W. Shen, W., K. Payer, W. H. Grover, S. R. Manalis, *"Measuring Single Cell Mass, Volume, and Density with Dual Suspended Microchannel Resonators"*. Lab Chip 2014, 14 (3), 569-576.

[13] Hu, Xin. *"Precision Error in Mass Measurements using Metal-coated Microchannel Resonators"*,Master thesis, Department of Precision and Microsystems Engineering, Faculty of Mechanical, Maritime and Materials Engineering, Delft University

of Technology, Delft,2019. [Online]. Available:http://resolver.tudelft.nl/uuid:da108fc4-81c6-41de-88a9-a0cc8fce3682

[14] Silvan Schmid, Luis Guillermo Villanueva, and Michael Lee Roukes. *"Fundamentals of nanomechanical resonators"*, volume 49. Springer, 2016. ISBN 978-3-319-28691-4. doi: 10.1007/978-3-319-28691-4.

[15] Marco Gagino, Georgios Katsikis, Selim Olcum, Leopold Virot, Martine Cochet, Aurélie Thuaire, Scott R. Manalis, and Vincent Agache, *"Suspended Nanochannel Resonator Arrays with Piezoresistive Sensors for High-Throughput Weighing of Nanoparticles in Solution"*, ACS Sensors 2020 5 (4), 1230-1238, DOI:10.1021/acssensors.0c00394

[16] Francisco Laborda, Eduardo Bolea, Gemma Cepriá, María T. Gómez, María S. Jiménez, Josefina Pérez-Arantegui, and Juan R. Castillo. Detection, *"Characterization and quantification of inorganic engineerednanomaterials: A review of techniques and methodological approaches for the analysis of complexsamples"*,Analytica Chimica Acta, 904:10 – 32, 2016. ISSN 0003-2670. doi: https://doi.org/10.1016/j.aca.2015.11.008. URL:http://www.sciencedirect.com/science/article/pii/S0003267015013677.

[17] Christian Schwaferts, Reinhard Niessner, Martin Elsner, and Natalia P. Ivleva, *"Methods for the analysisof submicrometer- and nanoplastic particles in the environment"*, TrAC Trends in Analytical Chemistry,112:52 – 65, 2019. ISSN 0165-9936. doi: https://doi.org/10.1016/j.trac.2018.12.014. URL:http://www.sciencedirect.com/science/article/pii/S0165993618304631

[18] Miller, James M. Lehto, Azadeh Ansari, David B. Heinz, Yunhan Chen, Ian B. Flader, Dongsuk D. Shin, L. Guillermo Villanueva, and Thomas W. Kenny, *"Effective quality factor tuning mechanisms in micromechanical resonators"*, Applied Physics Reviews 5, no. 4 (2018): 041307, [Online]. Available:https://doi.org/10.1063/1.5027850

[19] J. A. Barnes, A. R. Chi, L. S. Cutler, D. J. Healey, D. B. Leeson, T. E. McGunigal, J. A. Mullen, W. L. Smith,R. L. Sydnor, R. F. C. Vessot, and G. M. R. Winkler, *"Characterization of frequency stability"*, IEEE Trans-actions on Instrumentation and Measurement, IM-20(2):105–120, 1971, [Online]. Available:https://doi.org/10.1109/TIM.1971.5570702

[20] A. Demir and M. Hanay, *"Fundamental Sensitivity Limitations of Nanomechanical Resonant Sensors Due to Thermomechanical Noise"*, IEEE Sensors Journal, vol. 20, no. 4, pp. 1947-1961, 2020. [Online]. Available:10.1109/jsen.2019.2948681

[21] K. Ekinci, Y. Yang and M. Roukes, *"Ultimate limits to inertial mass sensing based upon nanoelectromechanical systems"*, Journal of Applied Physics, vol. 95, no. 5, pp. 2682-2689, 2004. [Online]. Available:10.1063/1.1642738.

7

Supplementary notes

7.1. PLL-Resonator design

To design a system consisting a resonator and a PLL, it is rational to start with input and output compatibility of one to another one. Although it is eventually a voltage or currents signal which goes across the components of resonator-PLL, it might contain different phase, frequency and amplitude. If we look back into the reason of choosing PLL for our project, we could realise that we aimed to track resonator's frequency and quickly bringing it back into resonant frequency when it is deviated. This could be done by locking the resonator's phase at its resonant frequency, which PLL is responsible for that. Therefore, the output and input phase is the prime target for a PLL, and hence a transfer function for resonator's phase and resonator-PLL model in the phase domain are essential parts of our design. Furthermore, determination of resonator-PLL parameters completes this design.

Note: This chapter is mostly based on Selim Olcum et al. work [94].

7.1.1. Phase-domain transfer function

In order to determine the phase domain transfer function of system, as it has been described in supplementary material of[94], phase-space transfer function of the resonator is required. This can be obtained by analyzing the time domain response of the resonator. Since, particularly, the resonator's phase response to small changes in the excitation frequency needs to be modeled, linear superposition as a mediator is applied to break down this problem into sum of two simpler problems. To do this, two situations, which resemble instantaneous change in resonant frequency by varying of the m_{eff} of resonator, are considered: response of the system to a harmonic excitation at resonant frequency ω_0 until time zero and response of the system to an excitation at ω_1, slightly different from (ω_0), after time zero. Based on linear superposition, the sum of these two decomposed responses together are the desired (total) response that is required. Suppose, as Figure 7.1 shows, the excitation forces (input forces) are $F_0 sin(\omega_0 t)$ and $F_0 sin(\omega_1 t)$ for the first and second situation respectively. The system response is then depicted in Figure 7.2.

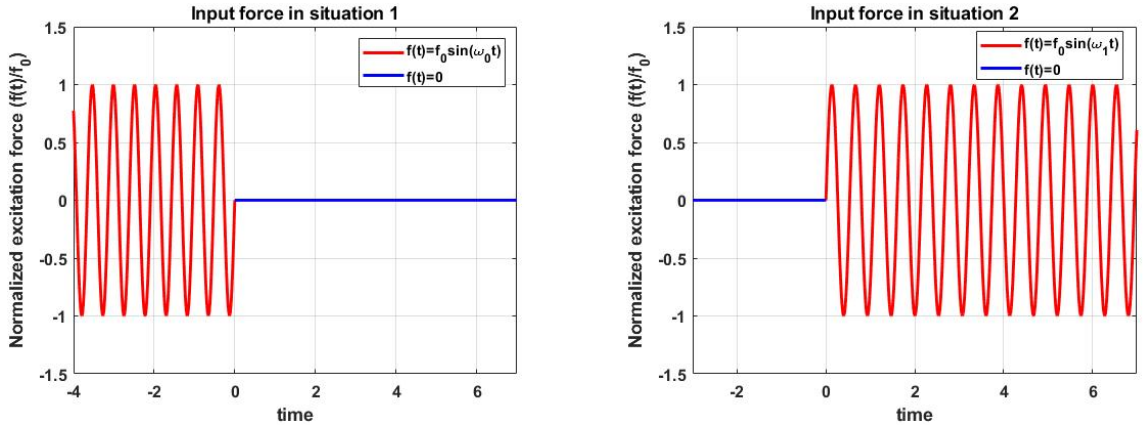

(a) (b)

Figure 7.1: *Input force (a) switched off at t=0 (b) switched on at t=0*

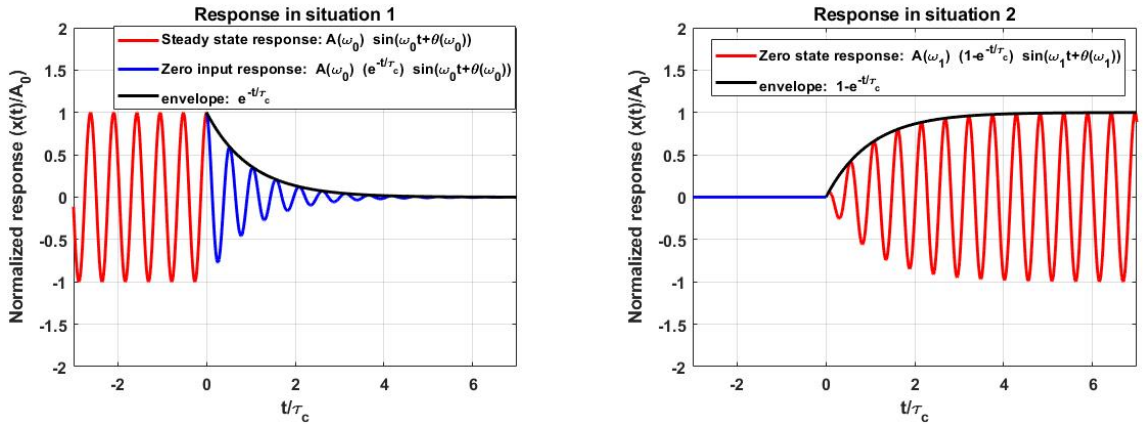

(a) (b)

Figure 7.2: *System response when (a) the input force switched off at t=0 (b) the input force switched on at t=0*

The total response that we need, is the response of the system after time zero, which are summation of zero-input and zero-state response, coloured in blue and red respectively, shown in Figure 7.2. Therefore, the total response is as follows:

$$x(t) = A(\omega_0)e^{-t/\tau_c}sin(\omega_0 t + \theta(\omega_0) + A(\omega_1)(1 - e^{-t/\tau_c})sin(\omega_1 t + \theta(\omega_1) \tag{7.1}$$

Zero-input and zero-state responses can be derived from the following equations with their initial conditions:

$$Zero-Input: \qquad \ddot{x} + \frac{\omega_0}{Q}\dot{x} + \omega_0^2 x = 0 \qquad for \;\; x(0) = A(\omega_0) \;\; and \;\; \dot{x}(0) = 0 \tag{7.2}$$

$$Zero-state: \qquad \ddot{x} + \frac{\omega_0}{Q}\dot{x} + \omega_0^2 x = \frac{f_0}{m}sin(\omega_1 t) \qquad for \;\; x(0) = 0 \;\; and \;\; \dot{x}(0) = 0 \tag{7.3}$$

Where $A(\omega)$, $\theta(\omega)$ and τ_c are amplitude, phase delay of the response and characteristic time of the system respectively, and can be found by:

$$A(\omega) = \frac{f_0/m}{\sqrt{(\omega_0^2 - \omega^2)2 + (\omega_0\omega/Q)^2}} \tag{7.4}$$

$$\theta(\omega) = arctan(\frac{\omega_0\omega}{Q(\omega^2 - \omega_0^2)}) \tag{7.5}$$

$$\tau_c = \frac{2Q}{\omega_0} \tag{7.6}$$

To access to the phase of resonator, Equation 7.1 should be converted to the form of $x(t) = A(t)sin(\omega_1 t + \phi(t))$, where $\phi(t)$ is the instantaneous phase of the resonator. This conversion is done using a trigonometric identity, simplifying and then linearizing the resonator phase around the resonant frequency. Next, the phase transfer function is determined by normalizing the time domain phase response and taking a Laplace transform of it. This process has been well described in the supplementary notes of [94]. The resonator's phase transfer function obtained from the mentioned process is given:

$$\Phi(s) = \frac{\Phi_{out}(s)}{\Phi_{in}(s)} = \frac{1}{\tau_c s + 1} \tag{7.7}$$

The transfer function above, which is also used in Figure 7.4-Figure 7.7, is identical to a first order lowpass filter with the bandwidth of $1/\tau_c$.

7.1.2. Resonator-PLL modeling

As it was earlier decided, a PLL architecture is employed, which controls the resonator's phase, resulting in tracking and stabilizing frequency of the resonator. This can be seen in Figure 7.3. However in a PLL, the most interest input and output variables are the input and output phase of a signal and not the currents and voltage. Therefore, a phase model for our system is much more efficient. This model, which describes the phase-space model of the resonator-PLL in way of [94], is shown in Figure 7.4.

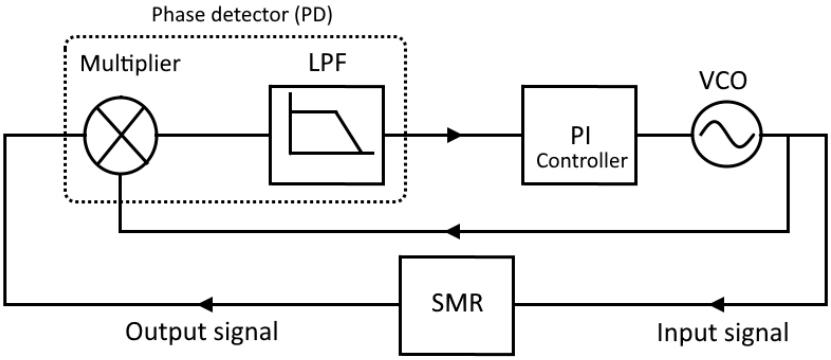

Figure 7.3: Block diagram of the resonator-PLL

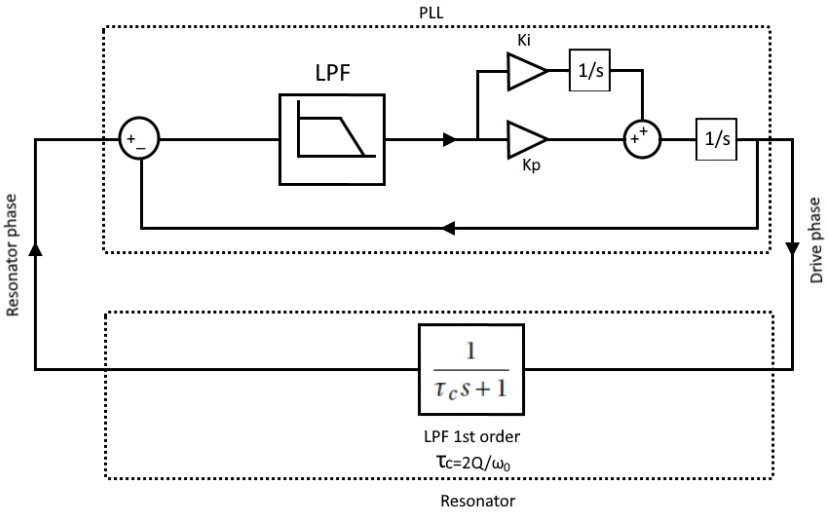

Figure 7.4: Phase-domain model of the resonator-PLL

In the phase-domain model, VCO is replaced by an integrator which converts the drive frequency into corresponding phase. Furthermore, the resonator is represented by a first order lowpass filter (LPF), whose determination was given in the subsection 7.1.1. In order to have access into the input frequency, an equivalent model can be obtained by adding a positive feed-forward path, a differentiator and a conversion gain to the phase -domain model. This is shown in Figure 7.5.

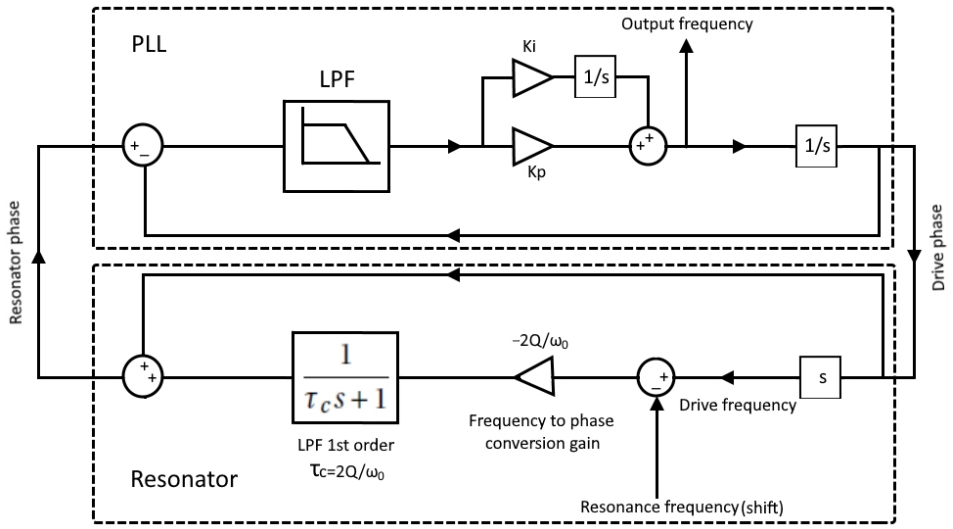

Figure 7.5: Phase-domain model of the resonator-PLL with access to the input frequency

It can be shown that both model used for resonator's phase in Figure 7.4 and Figure 7.5 are equivalent and it was done to get access to the input frequency. This can be proven, if transfer function of the model bellow becomes identical to Equation 7.7.

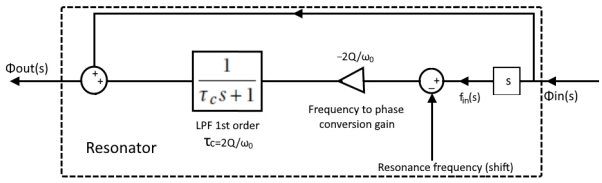

Figure 7.6: Resonator's phase model

$$\Phi_{out}(s) = \frac{-\tau_c s}{\tau_c s+1}\Phi_{in}(s) + \Phi_{in}(s) = (1 - \frac{\tau_c s}{\tau_c s+1})\Phi_{in}(s) \quad \Rightarrow \quad \Phi(s) = \frac{\Phi_{out}(s)}{\Phi_{in}(s)} = 1 - \frac{\tau_c s}{\tau_c s+1} = \frac{1}{\tau_c s+1} \tag{7.8}$$

The model shown in Figure 7.5 can even become simpler when the negative feedback cancels the positive feed-forward and also when the integrator cancels the differentiator. Furthermore, a general form of LPF transfer function with cut-off frequencies $1/\tau_k$ is placed, which is crucial for determining the PLL parameters in subsection 7.1.3. Figure 7.7 illustrates the mentioned modifications. This model is used to compute the required parameters in subsection 7.1.3.

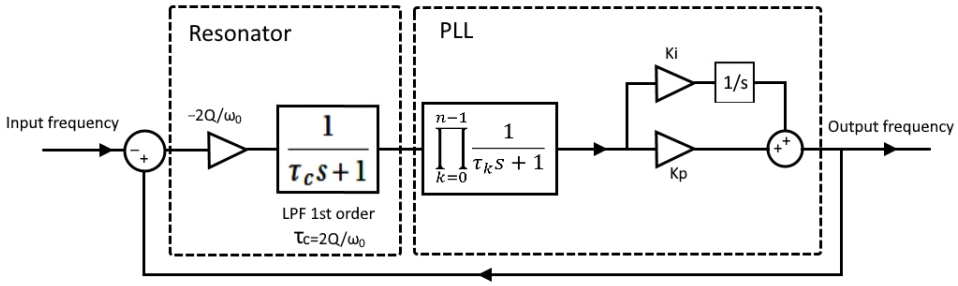

Figure 7.7: Generalized Phase-domain model of the resonator-PLL

7.1.3. Resonator-PLL parameters determination

Final goal of a resonator-PLL system is to lock the resonator's phase at its resonant frequency. In other words, the output phase must follow the input phase ($\Phi_{out} = \Phi_{in}$) as fast as possible, resulting in well-tracking the

resonant frequency. To achieve this, a wise decision is to have an identical transfer function for resonator-PLL closed loop to a Butterworth lowpass filter. Looking at Figure 7.8 reveals the truth of this decision. The Butterworth, has the most flat amplitude gain before reaching the cut-off frequency, which guaranties chasing of the output signal by input signal.

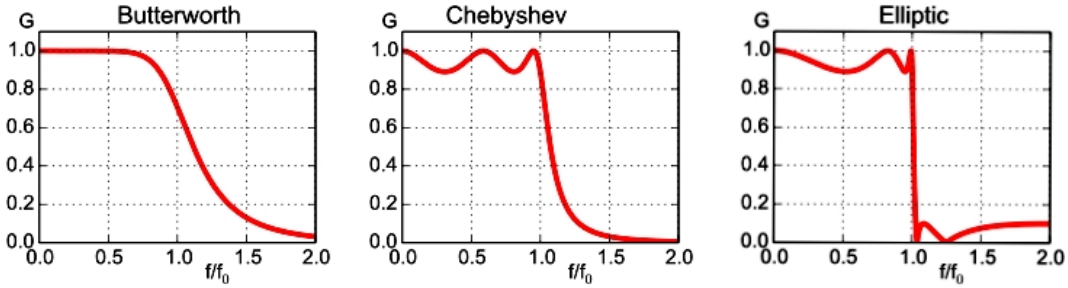

Figure 7.8: Three types of a lowpass filter [140]

To obtain such flat amplitude, the closed loop transfer function of phase domain model shown in Figure 7.7,Equation 7.9, has to equate general form of Butterworth transfer function (Equation 7.11), where β is the Butterworth cut-off frequency or resonator-PLL bandwidth, n is the order of Butterworth filter and B_n is Btterworth poles polynomial of order n [28, 40] . In this way, PLL variables such as k_i, k_p and τ_k are parametrically determined based on desired resonator-PLL bandwidth β.

$$H(s) = \frac{k_p s + k_i}{(s^2 + s/\tau_c)\prod_{k=1}^{n-1}(\tau_k s + 1) + k_p s + k_i} \tag{7.9}$$

$$H(s) = \frac{1}{B_n(s/\beta)} \tag{7.10}$$

Equation 7.9 and Equation 7.11 can be equated as follows:

$$\frac{k_p s + k_i}{(s^2 + s/\tau_c)\prod_{k=1}^{n-1}(\tau_k s + 1) + k_p s + k_i} = \frac{1}{B_n(s/\beta)} * \frac{k_p s + k_i}{k_p s + k_i} \tag{7.11}$$

By parametrically solving them, required parameters are determined. These parameters for the first three Butterworth filter orders are tabulated in Table 7.1.

Table 7.1: *Resonator-PLL parameters*

Butterworth filter order n	Proportional gain k_p	Integral gain k_i	Lowpass filter time constant τ_1	Lowpass filter time constant τ_2
1	β	$\frac{k_p}{\tau_c}$	–	–
2	$\frac{\beta}{\sqrt{2}}$	$\frac{k_p}{\tau_c}$	$\frac{\sqrt{2}}{2\beta}$	–
3	$\frac{\beta}{2}$	$\frac{k_p}{\tau_c}$	$\frac{1\pm j}{2\beta}$	$\frac{1\mp j}{2\beta}$

7.1.4. MATLAB and Simulink simulation

Once required parameters have been found in Table 7.1, to ensure that they perform like a Butterworth lowpass filter, amplitude response as a function of normalized frequency is plotted. As it was expected, Figure 7.9 shows ultimate flatness for the passbands and 20,40 and 60$[dB/decade]$ attenuation for the stopband of system order 1,2 and 3 respectively. More extensive investigation reveals that system order 1 demonstrates

slightly larger bandwidth, resulting in faster response to the input, than order 2 and 3. This is shown in Figure 7.10.

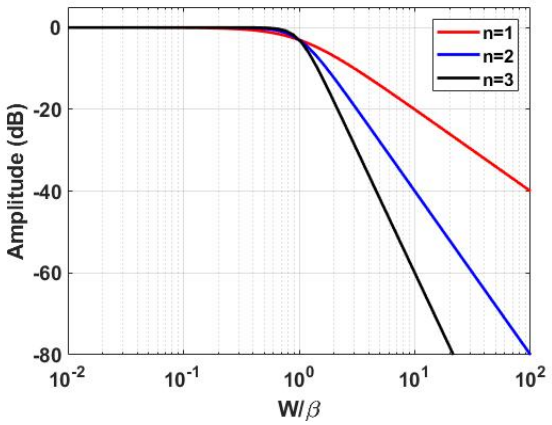

Figure 7.9: *Amplitude response of the closed loop system*

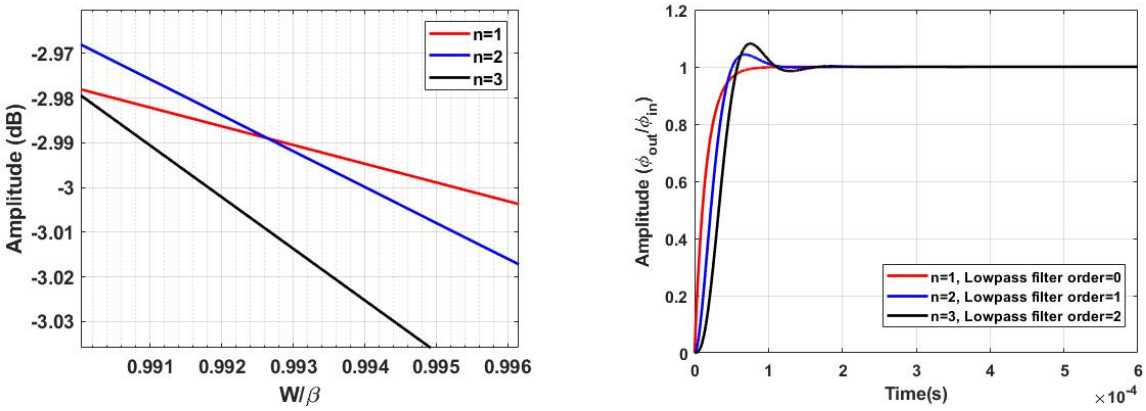

(a) (b)

Figure 7.10: *Comparison among system orders in terms of (a) bandwidth, and (b) Step response.*

To choose one of the system orders for further simulations and possibly practically implementation by Zurich instrument, possessing larger bandwidth (larger flat passband) is in the first priority, regardless of concerning about the roll off speed. Therefore, system orders 1,2 and 3 respectively, are the most efficient ones. However, keeping in mind that system order 1 does not need a lowpass filter to work in the phase domain (see Table 7.1), but in reality, phase detection is not possible without a lowpass filter. Therefore, system order 1 is eliminated from the candidates and the second choice, which is system order 2, is selected for further simulations.

In Simulink, the performance of phase domain model shown in Figure 7.7 with a step signal as an input is tested. To do this, β and τ_c should be determined. From the work of previous students, Q and $\omega_0 = \omega_r$ thus τ_c is known, and $\omega_{PLL} = \beta$ can be determined under following condition:

- $\omega_{PLL} < \omega_L < \omega_r$

$\omega_L < \omega_r$, since, it is technically impossible to block a signal with higher frequencies than cut-off frequency of a low pass filter, and in our model, we need to suppress such signal in the phase detector. To elaborate it, looking at Figure 7.3 and considering PD block, where its output is a signal containing the phase difference and inputs are two signals, e.g. cosinusoidal, $V_r(t) = A_r cos(\omega_r t + \phi_r)$ and $V_o(t) = A_o cos(\omega_o t + \phi_o)$, and $\omega_r \approx$

ω_o. Recall that a multiplier multiplies two signals as follows:

$$2cos(A)cos(B) = cos(A-B) + cos(A+B) \longrightarrow V(t) = \frac{A_o A_r}{2}(cos(\phi_r - \phi_o) + cos(2\omega_r + \phi_r + \phi_o)) \tag{7.12}$$

Therefore, there will be one output containing the cosine of the phase difference and one output at twice the input frequency. Since we need only the phase difference component, the doubled frequency component must be blocked by the lowpass filter with the same cut-off frequency as $2\omega_r$. However, in reality, we do not have an ideal lowpass filter, which can block signals at its cut-off frequency. Thus, we take a safe distance from it by choosing $\omega_L = \frac{1}{10}\omega_r$, which explicitly implies $\omega_L < \omega_r$.

$\omega_{PLL} < \omega_L$ is required so that a closed loop transfer function, which is identical to Butterworth lowpass filter, is obtained as it can be seen in Table 7.1.

Therefor, following steps result in determination of β, k_p and k_i:

- $\omega_L = \frac{1}{10}\omega_r$
- $\omega_L = \frac{1}{\tau_1} \longrightarrow \tau_1 = \frac{1}{\omega_L}$
- $\tau_1 = \frac{\sqrt{2}}{2\beta} \longrightarrow \beta = \frac{\sqrt{2}}{2\tau_1} \longrightarrow k_p = \frac{\beta}{\sqrt{2}} \longrightarrow k_i = \frac{k_p}{\tau_c}$

The parameters above are the inputs of Simulink's model, shown in Figure 7.11. The step response of the system then can be seen in Figure 7.12, where it confirms tracking of the input signal by resonator-PLL and it is evident that resonator-PLL response time is much shorter than resonator's phase response time. To have an exact comparison on response speeds, settling time t_s, in which the error between the output response and final response falls within 2% of finale response, is employed. Next, Figure 7.13 and Figure 7.14 compare the resonator's phase responses of cantilevers, made by PME former students: S.D Savio and X.Hu, to a step input in case of resonator itself and resonator-PLL respectively. To complete this section, frequency response of $X.Hu-2nd$ is depicted in Figure 7.15, where its flat amplitude before the bandwidth can be seen. The corresponding data is also gathered in Table 7.2.

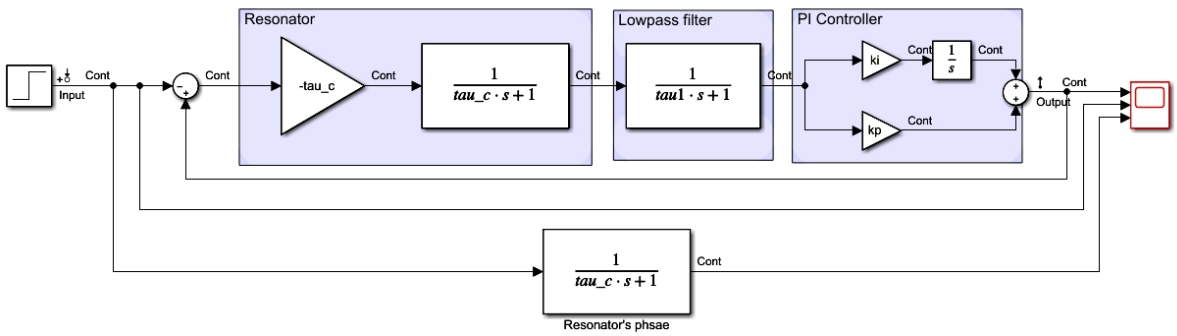

Figure 7.11: *Phase model under test*

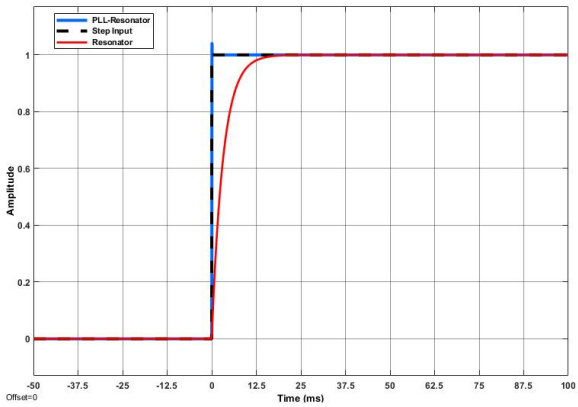

(a)

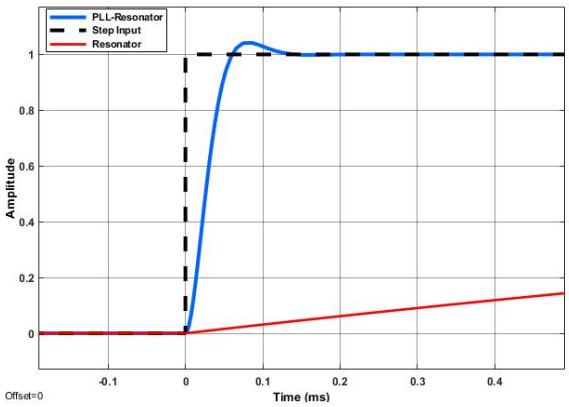

(b)

Figure 7.12: *Step responses of resonator-PLL and resonator itself.*

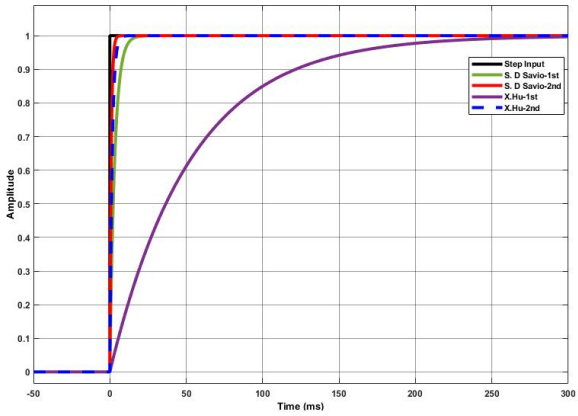

(a)

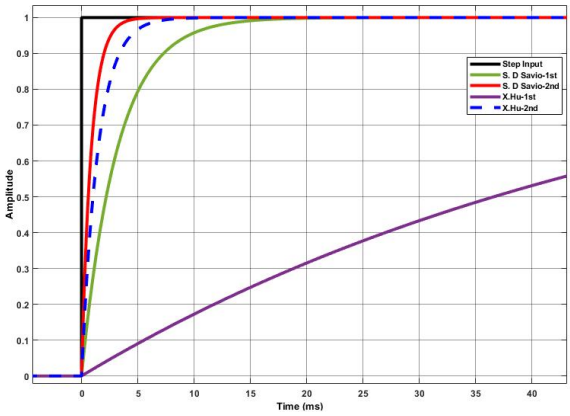

(b)

Figure 7.13: *Step responses of different resonators.*

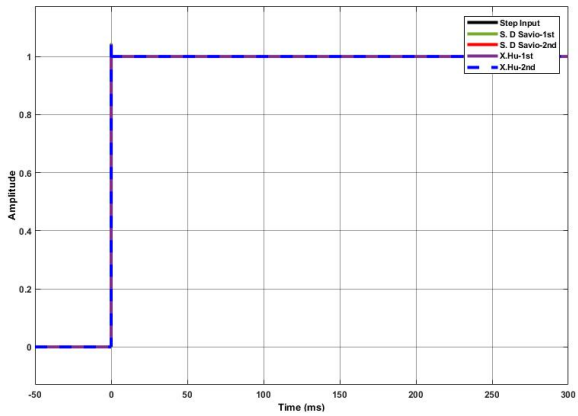

(a)

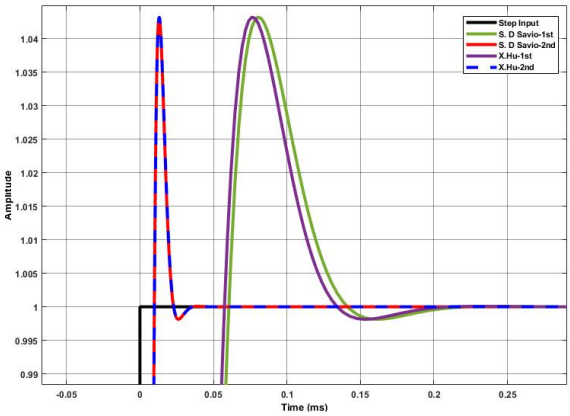

(b)

Figure 7.14: *Step responses of different resonator-PLLs.*

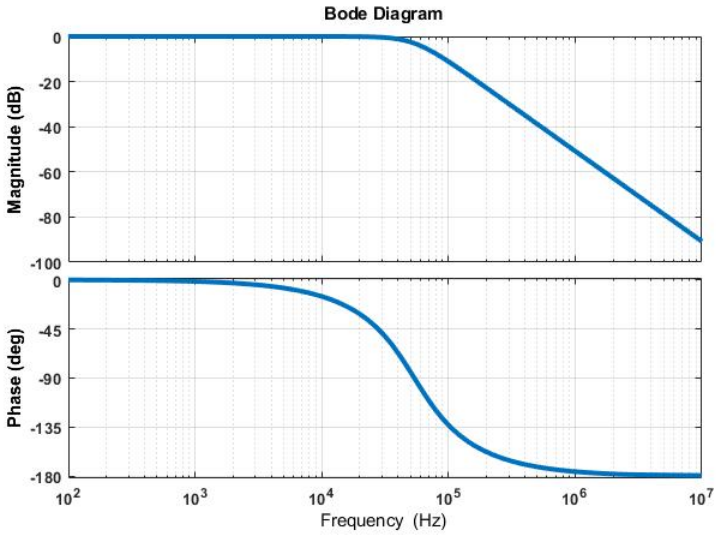

Figure 7.15: *Frequency response of $X.Hu-2nd$*

Table 7.2: *Resonator-PLL parameters*

SMR name Mode nr.	ω_r $[Hz]$	Q $[-]$	ω_L $[Hz]$	$\omega_P LL$ $[Hz]$	τ_c $[ms]$	τ_{PLL} $[ms]$	$t_S(R)$ $[ms]$	$t_S(PLL)$ $[ms]$	$\frac{\omega_r}{\omega_{PLL}}$ $[-]$	K_{eff} [N/m]	R [Hz/fg]	S [fg/Hz]
S. D Souza-1st	124007	1233	12401	8768	3.165	0.018	12.381	0.108	14.1421	2.37	0.0159	62.9554
S. D Souza-2nd	764848	2084	76484	54083	0.867	0.0029	3.4	0.017	14.1421	2.33	3.7924	0.2637
X. Hu-1st	130437	21639	1304.37	9223.29	52.806	0.017	206.6	0.103	14.1421	4.53	0.0097	103.4589
X. Hu-2nd	760900	3507	76090	53803.75	1.467	0.0029	5.7	0.018	14.1421	3.98	2.1826	0.4582

7.2. Frequency stability

A SMR device attached to a PLL consists of different mechanical and electrical components that introduce noises to the measured signal. If there were noise-free measured signal, we could have a precise system by which we could measure smallest masses. However, in presence of noises, we are confined to a specific precision, which affects mass sensing precision. Therefore, it is necessary to recognise the dominant noises in our system in terms of their behaviors and ways to reduce them in our system. At the same time, it is necessary to determine sensitivity/responsivity of the product and improve it in the future. Since in this project we need to determine possible smallest measured mass by our system, we need to define a way for it. Frequency stability methods are normally applied for this purpose, and this chapter is concerned with the mentioned aspects of noise and determination of mass sensing by a SMR.

There are five noise types for a frequency source [7] : white phase- modulation (PM) noise, flicker PM noise, white frequency-modulation (FM) noise, flicker FM noise and random walk FM ($RW\ FM$). It is noted that in FM and PM, the frequency and the phase of the carrier signal are varied respectively. Therefore the five mentioned noises can be categorized into three types, including: white, flicker and random walk noises which their frequency spectrums are shown in Figure 7.16. It is noticed that white noise has almost equal intensity when frequency changes. However in the cases of flicker and random walk, the intensity attenuates as the frequency increases. This attenuation is more intense in random walk than in flicker.

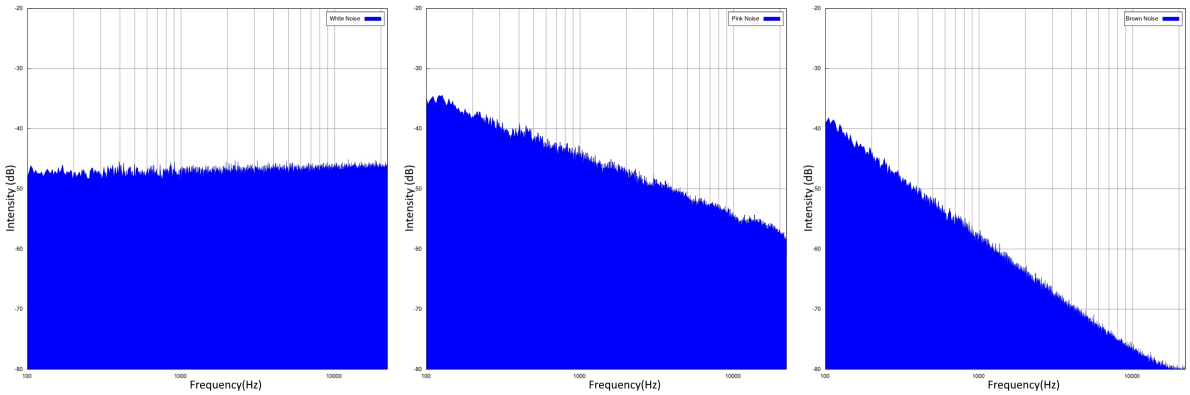

(a) (b) (c)

Figure 7.16: *frequency spectrum [139] of (a) White noise (b) flicker noise and (c) random walk noise.*

Frequency stability can be characterized in the frequency domain and also in the time domain. Before introducing them, a short introduction on noise model is given.
Suppose the output signal of a precision oscillator is given by [42]:

$$V(t) = [V_0 + \epsilon(t)]sin(2\pi\nu_0 t + \phi(t)) \tag{7.13}$$

Where

- V_0: nominal peak output voltage
- $\epsilon(t)$: amplitude deviation by time
- ν_0: nominal frequency [Hz]
- $\phi(t)$: phase shift [rad]

Knowing that the instantaneous angular frequency is the derivative of the total phase, the instantaneous frequency is then determined as follows:

$$\nu_t = \nu_0 + \frac{1}{2\pi}\frac{d\phi}{dt} \tag{7.14}$$

And the fractional instantaneous frequency is given by [12]:

$$y(t) = \frac{\nu(t)}{\nu_0} = 1 + \frac{1}{2\pi\nu_0}\frac{d\phi}{dt} \tag{7.15}$$

Now the two frequency stability approaches are introduced briefly by stressing on the time domain analysis more than the frequency domain approach, since the former is tightly concerned with this project.

In frequency domain analysis, a Fast Fourier Transform FFT is performed on the time domain data to obtain power spectral densities (PSDs) that describe frequency or phase fluctuations as a function of frequency. There are different PSDs which describe the frequency stability, however the two most important PSDs are PSD of Frequency Fluctuations $S_y(f)$ and PSD of Phase Fluctuations $S_\phi(f)$. In this stability analysis, the previously mentioned noises can be modeled in the form of f^α which is approximately equal to $S_y(f)$, where α is the exponent of the power law noise process and f is the Fourier or sideband frequency [108]. This α varies for different noises, for example, α equals $0, -1, -2$ for white, flicker and random walk noises respectively. Figure 7.17 depicts different types of noise with their exponents of the power law noise.

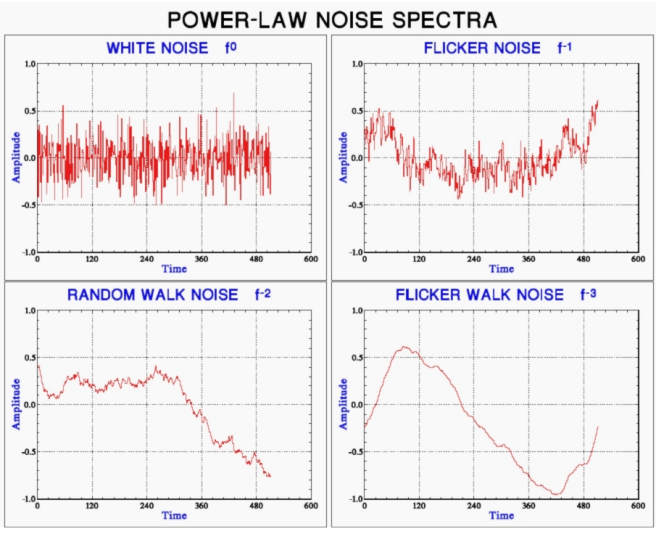

Figure 7.17: Example of noises with different α [108]

In time domain analysis, statistics is employed to measure the frequency stability. To do that, some variances i.e., Allan, Hadamard, time and Theo1 [108] can be used to characterize instabilities of a frequency source, but standard variance is excluded and should not be used for this purpose. The reason is that it shows a non-convergent behavior for the non-white FM noise types [7] which are commonly seen in frequency sources. This can be seen in Figure 7.18, where the standard deviation (blue curve) of flicker FM noise diverges by increase in number of samples, while the number of data points is not important when the noise level is the same. However, Allan deviation (red curve) demonstrates its independence from the number of data points. That is why Allan deviation is widely used for the purpose of frequency stability.

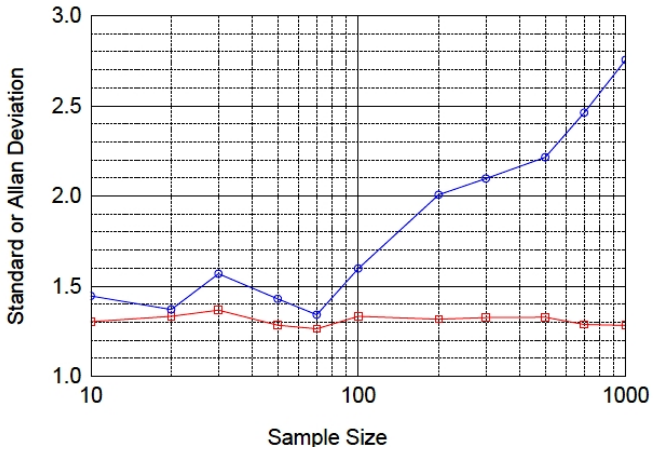

Figure 7.18: Standard and Allan deviation convergence for flicker FM noise [108]

Here, Allan variance (AVAR) and Allan deviation (ADEV) are introduced in the way of [12]. Allan determines the averaged fractional frequency from fractional instantaneous frequency obtained in Equation 7.15 by [12]:

$$\overline{y}_k = \frac{1}{\tau}\int_{t_k}^{t_{k+1}} y(t)\,dt \tag{7.16}$$

In Equation 7.16, τ is the averaging time or gate time and $t_{k+1} = t_k + \tau$. Averaging is a method in signal processing to increase signal to noise ratio (SNR), which is a measure for strength of a signal relative to the engaged noise. Here is the same, we want to decrease noise influence in order to be able precisely measuring fractional frequency. The smallest averaging time is identical to sampling period (time interval between two consecutive measurements of fractional frequency) $T = \frac{1}{f_s}[s]$. However, we might be interested in different time intervals causing different number of data points inside the interval. These intervals can be found by

multiplying an increasing factor e.g. $m = \{1,2,4,8...\}$, which is called averaging factor, with sampling period T. Hence, averaging time can be calculated by $\tau = m * T$.
Allan variance and Allan deviation are then computed for a specific τ with M number of periods as follows:

$$AVAR : \sigma_y^2(\tau) = \frac{1}{M} \sum_{k=0}^{M-1} \frac{(\overline{y}_{k+1} - \overline{y}_k)^2}{2} \tag{7.17}$$

$$ADEV : \sigma_y(\tau) = \sqrt{\sigma_y^2(\tau)} \tag{7.18}$$

Allan deviation as a function of averaging time can be an appropriate measure for the fractional frequency as a function of time, by which mass precision (δm) of a SMR device at a specific averaging time τ can be obtained as follows

$$\sigma_y(\tau) = \frac{\delta f}{f_0} = \frac{frequency \;\; imprecision}{nominal \;\; frequency} \tag{7.19}$$

$$\delta m \approx -2 m_{eff} \frac{\delta f}{f_0} = -2 m_{eff} \sigma_y(\tau) \tag{7.20}$$

A pictorial representation of Allan deviation σ_y as a function of gate time τ is shown in Figure 7.19, where the slope of the graph represents the dominant noise type in that certain gate time τ. There are also relations that converts the slopes of $\sigma_y - \tau$ to the ones of $S_y(f)$ diagram and vice versa [108]:

$$\sigma_y(\tau) \approx \tau^{\mu/2} \tag{7.21}$$

$$S_y(f) \approx f^{\alpha} \tag{7.22}$$

$$\mu = -\alpha - 1 \tag{7.23}$$

Where α is the exponent of the power law noise that were described earlier, and μ is the slope of $\sigma_y - \tau$ graph.

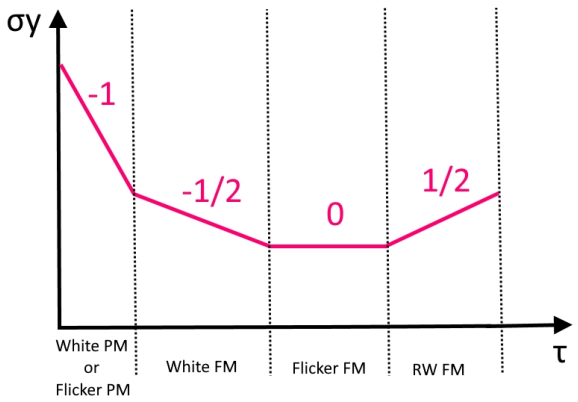

Figure 7.19: $\sigma_y - \tau$ diagram

7.3. Chip and hollow cantilever dimensions

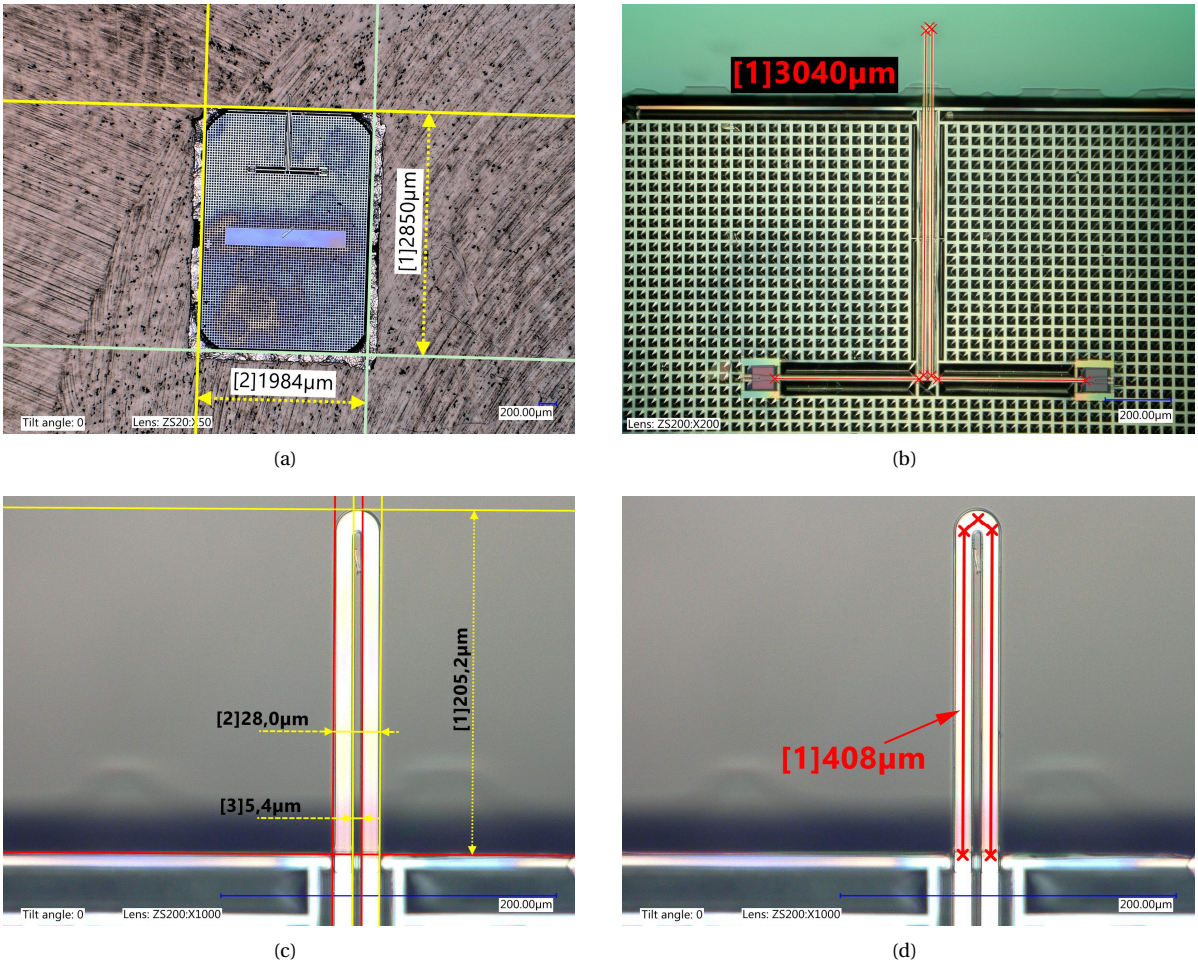

Figure 7.20: *a) Top view of the chip and fluidic channels with dimensions. b) Top view of on-chip and suspended channel. c) and d) Top view of the U-shaped silicon dioxide resonator with dimensions.*

Table 7.3: *Chip and resonator dimensions*

Parameter	Value (μm)
Resonator total length	408
Gap between the legs	5.4
Channels width (outer)	11.3
Channels width (inner)	9
Channels height (outer)	3.5
Channels height (inner)	2.5
Chip length	2850
Chip width	1984

7.4. Simulated modes

This COMSOL study was performed based on our resonator's dimensions with a Young's modulus of 87 GPa. The fact is that there are a range of values from 60-92 GPa for modulus of elasticity for SiO_2. Therefore, different modes irrespective of mode numbers would appear in very different resonance frequencies. We chose this value based on a study conducted by our department [14]. The resonance frequencies were 112 kHz, 674 kHz and 698 kHz for first bending, first torsional and second bending modes respectively.

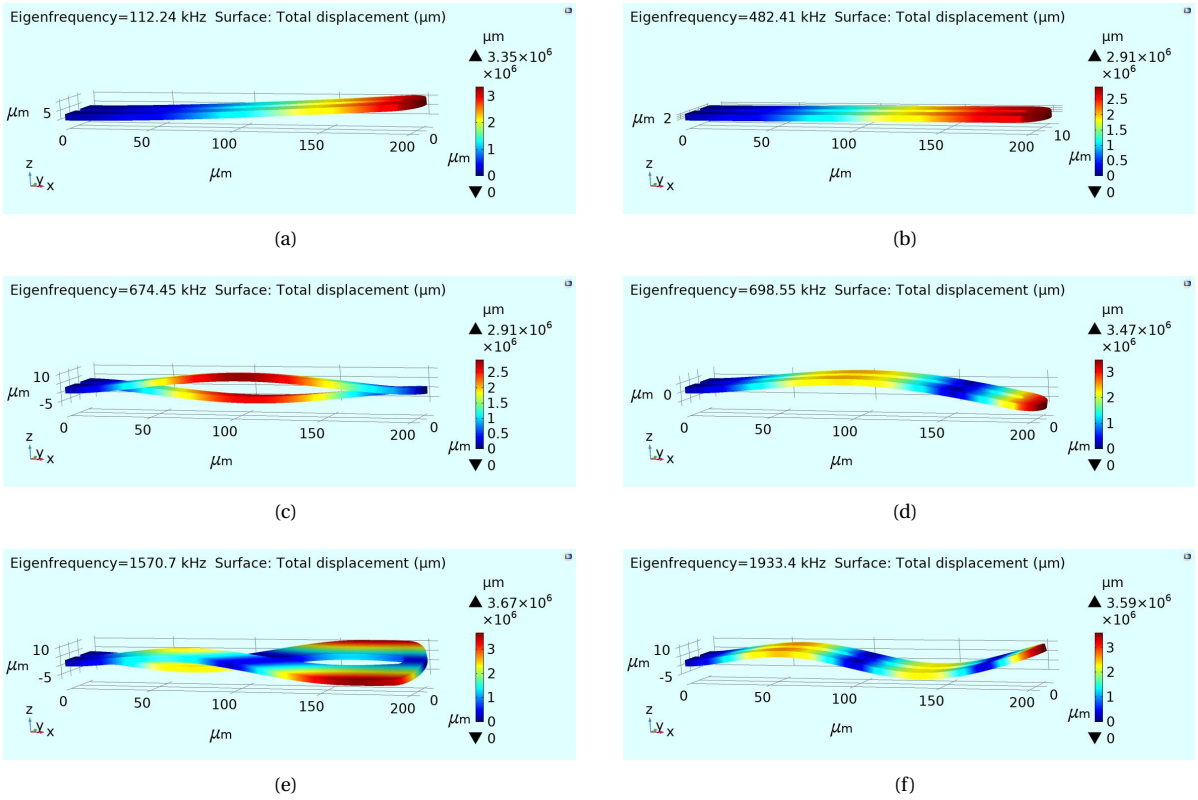

(a) (b) (c) (d) (e) (f)

Figure 7.21: *Results of eigenfrequency analysis by COMSOL including three out of plane bending modes, two torsional modes and one in-plane bending mode. a) First bending mode, b) First in-plane bending mode, c)First torsional mide, d)Second bending mode, e)Second torsional mode, f)Third bending mode*

7.5. Characterization of the empty SMR

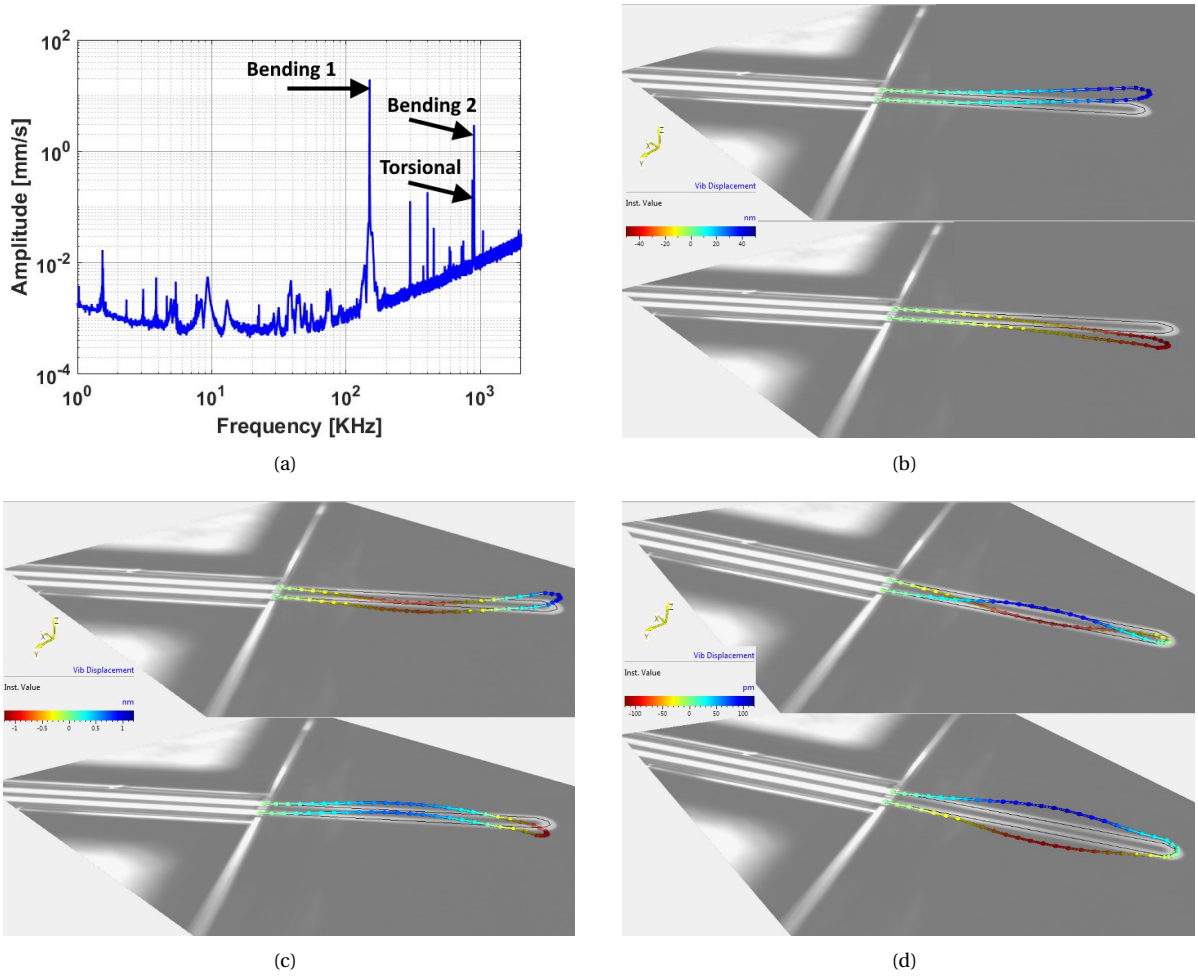

Figure 7.22: *(a) Complete frequency spectra of the empty resonator up to 2 MHZ. Mode shapes of (b) first bending mode at 149.420 kHz, (c) second bending mode at 893.287 kHz and (d) first torsional mode at 869.414 kHz.*

Table 7.4: *Important parameters of the empty resonator in a vacuum environment of 0.012 mbar*

Parameter	Bending 1	Bending 2	Torsional
f_r $[kHz]$	149.420	893.287	869.414
Q [-]	25993	13214	43634
K_{eff} $[\mathrm{N\,m^{-1}}]$	71.45	538.25	1503.17
m_{eff} $[g]$	8.107×10^{-8}	1.709×10^{-8}	5.037×10^{-08}

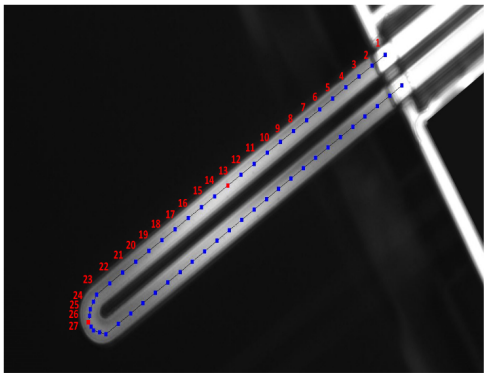

(a)

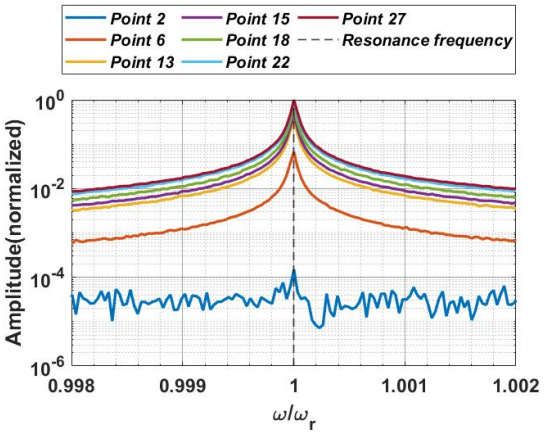

(b)

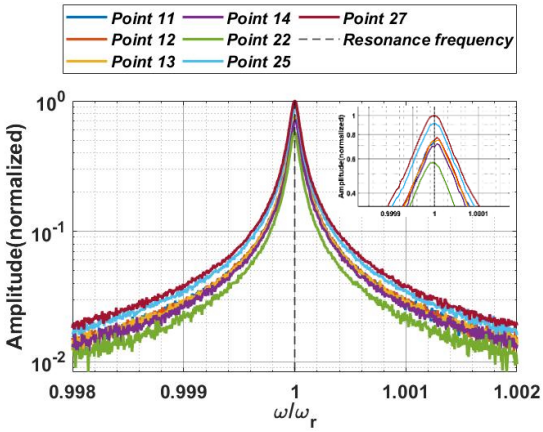

(c)

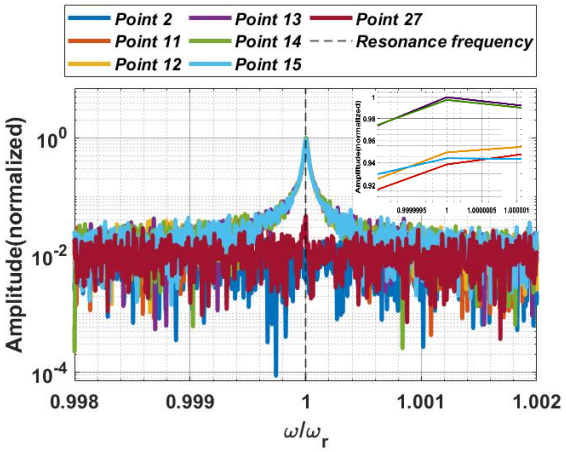

(d)

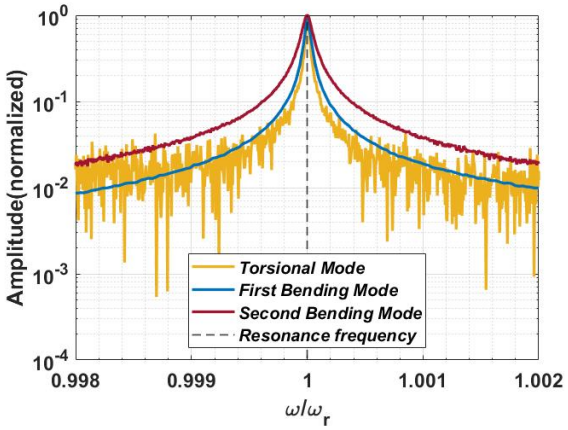

(e)

Figure 7.23: *(a) Top view of the cantilever with girds corresponding measurement points. Normalized amplitude response at resonance for (b) first bending mode, (c) second bending mode and (d) first torsional mode. (e) Normalized amplitude responses of the three modes, which indicates that the torsional mode has the highest quality factor. The highest amplitudes were obtained at the tip of resonator for the first and second flexural modes (point 27), and at a point near the middle of the resonator in the first portion of the length for the torsional mode (point 13). These points are of the utmost importance for better sensing the mass of particles,due to having highest signal to noise ratio.*

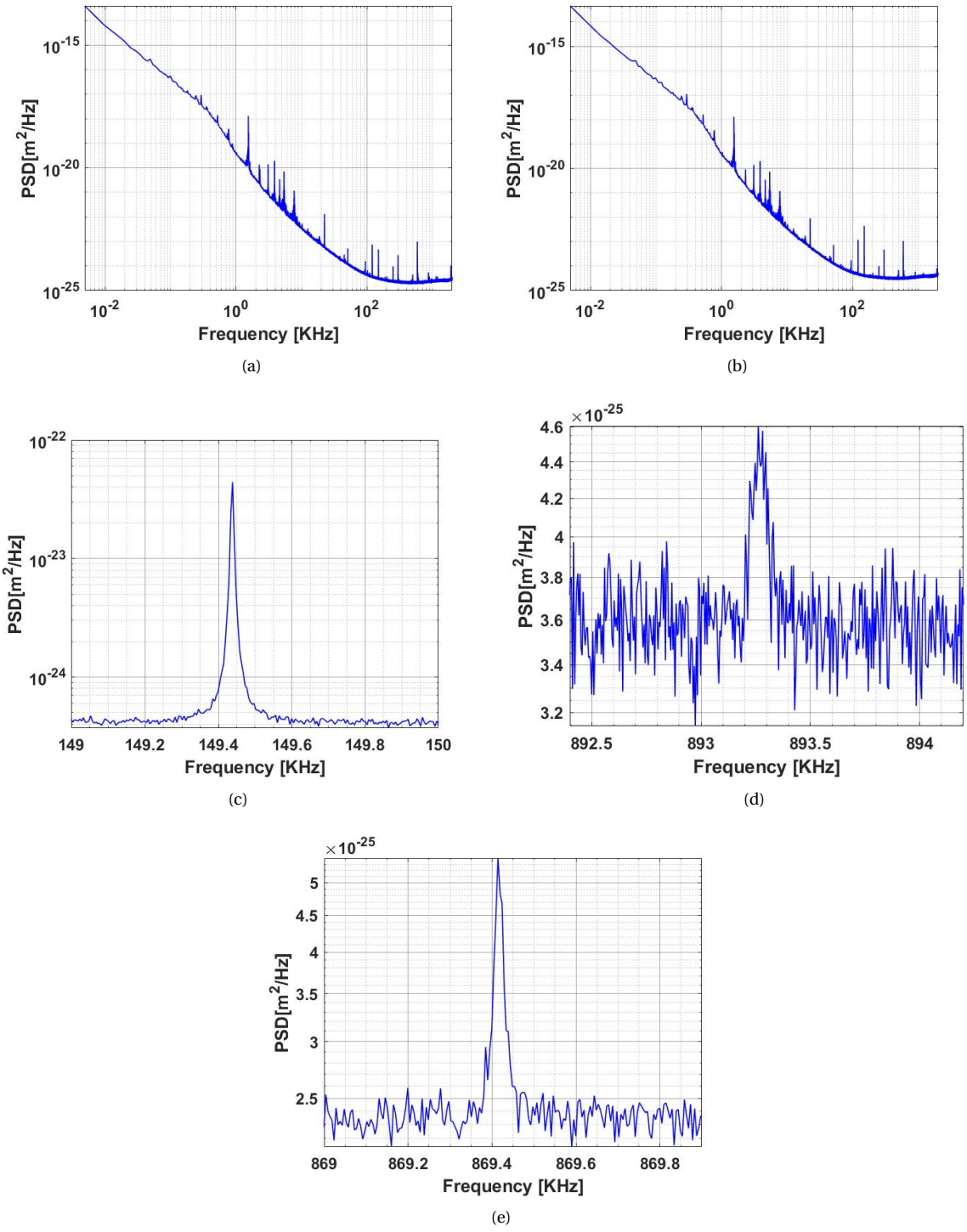

Figure 7.24: *(a) The total displacement PSD at point 13 of the empty resonator, and (b) at point 27. (c) PSD of the first bending mode at point 27, (d) PSD of the second bending mode at point 27, and (e) PSD of the torsional mode at point 13. Power Spectral Densities (PSD)s were measured when the resonator was not excited by piezoelectric. This was done to measure vibrations of the resonator in presence of thermo-mechanical noise. This was obtained to compute the stiffness of resonator for different modes. The following equation was used to compute the cantilever stiffness (k) [82]:* $k = \frac{4K_B TQ}{\omega_r PSD(\omega_r)}$*, where T is the temperature in kelvin,* k_B *is Boltzmann's constant in joule per kelvin,* ω_r *is resonance frequency and* $PSD(\omega_r)$ *is the power spectral density of the resonator displacement evaluated at the resonance frequency.*

7.6. Characterization of the water-filled SMR

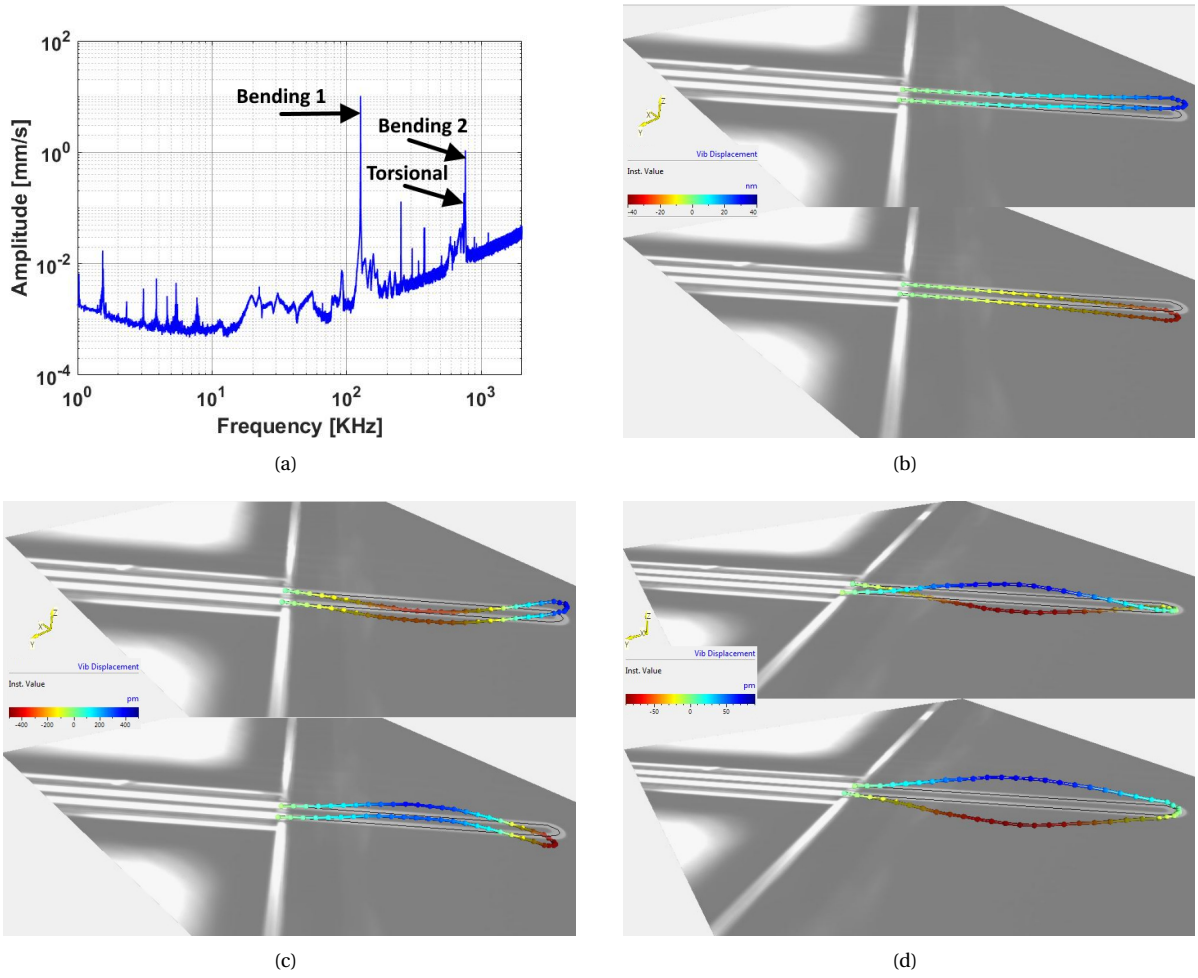

(a) (b)

(c) (d)

Figure 7.25: *(a) Complete frequency spectra of the water-filled resonator up to 2 MHZ. Mode shapes of (b) first bending mode at 126.393 kHz, (c) second bending mode at 759.192 kHz and (d) first torsional mode at 740.528 kHz. These shifts in resonance frequencies compared to empty case are mainly due to increase in effective mass of filled cantilever, which is inversely proportional to resonance frequency.*

Table 7.5: *Important parameters of the water-filled resonator in a vacuum environment of 0.012 mbar*

Parameter	Bending 1	Bending 2	Torsional
f_r $[kHz]$	126.393	759.192	740.528
Q [-]	9716	3241	4784
K_{eff} $[\mathrm{Nm}^{-1}]$	71.45	538.25	1503.17
m_{eff} [g]	1.133×10^{-7}	2.365×10^{-8}	6.943×10^{-08}

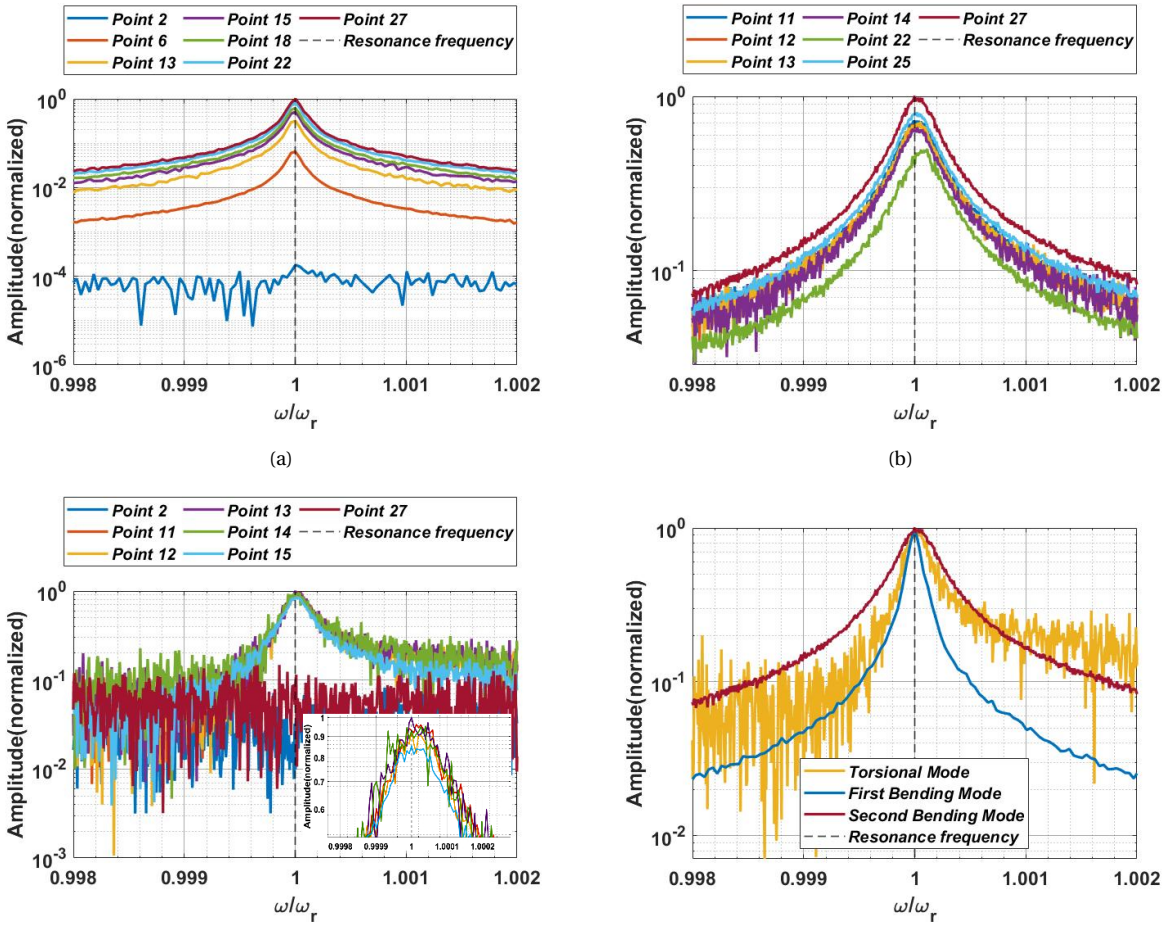

Figure 7.26: *Amplitude response of the water-filled cantilever at different measurement points (see Fig. 7.23(a)) on the resonator for (a) first bending mode, (b) second bending mode and (c) torsional mode. (d) Normalized amplitude responses of the three modes, indicating that the first bending mode has the highest quality factor.*

7.7. PLL circuit of the lock-in amplifier

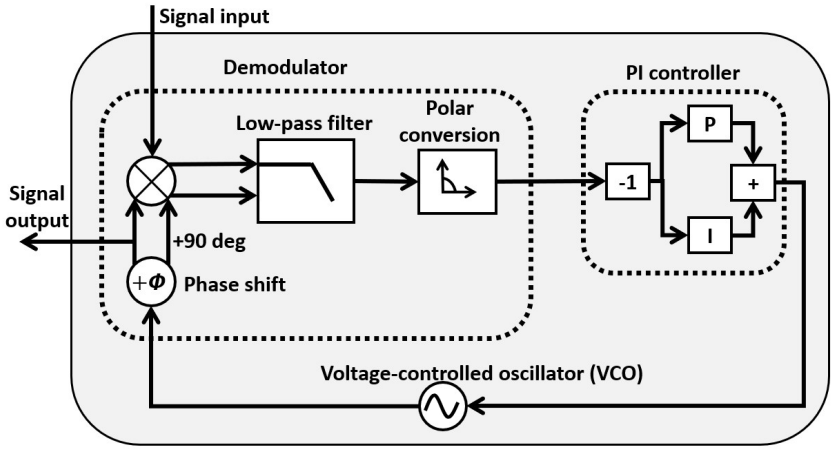

Figure 7.27: *Schematic of the PLL in Zurich Instrument (UHFLI): The reference signal generated by a Voltage Controlled Oscillator (VCO) and its 90° version are multiplied with the input signal that comes from DUT. The outputs of this mixing are then low pass filtered and converted into polar coordinates which provides the signal phase* Θ*. The phase is then compared with the resonance phase, and a new phase, that corrects the resonator's dynamics, is computed by the PI controller. Finally, this signal is applied to the DUT for a new loop.*

7.8. UHFLI transfer function and parameters

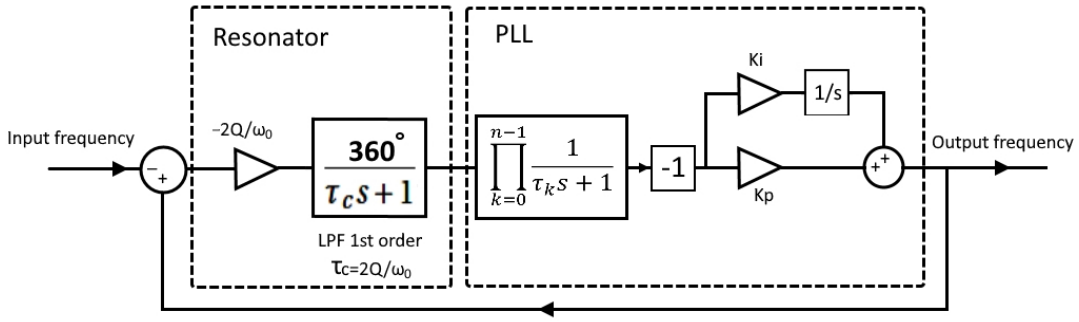

Figure 7.28: *Generalized phase domain diagram of resonator and PLL in UHFLI*

For the diagram above, transfer function below is obtained:

$$H(s) = \frac{-360k_p s - 360k_i}{(s^2 + s/\tau_c)\prod_{k=1}^{n-1}(\tau_k s + 1) - 360k_p s - 360k_i} \tag{7.24}$$

The parameters for first five order of the system are given in Table 7.6 and the corresponding frequency responses and step responses are shown in Fig. 7.29.

Table 7.6: *Resonator-PLL parameters when β is in HZ*

System order	k_p	k_i	τ_1	τ_2	τ_3	τ_4
1	$\frac{-\beta}{360}$	$\frac{k_p}{\tau_c}$	–	–	–	–
2	$\frac{-\beta}{360\sqrt{2}}$	$\frac{k_p}{\tau_c}$	$\frac{\sqrt{2}}{2\beta}$	–	–	–
3	$\frac{-\beta}{720}$	$\frac{k_p}{\tau_c}$	$\frac{1\pm j}{2\beta}$	$\frac{1\mp j}{2\beta}$	–	–
4	-0.0011β	$\frac{k_p}{\tau_c}$	$\frac{0.667}{\beta}$	$\frac{0.320+0.687j}{\beta}$	$\frac{0.320-0.687j}{\beta}$	–
5	-0.0009β	$\frac{k_p}{\tau_c}$	$\frac{0.609+0.301j}{\beta}$	$\frac{0.609-0.301j}{\beta}$	$\frac{0.199+0.793j}{\beta}$	$\frac{0.199-0.793j}{\beta}$

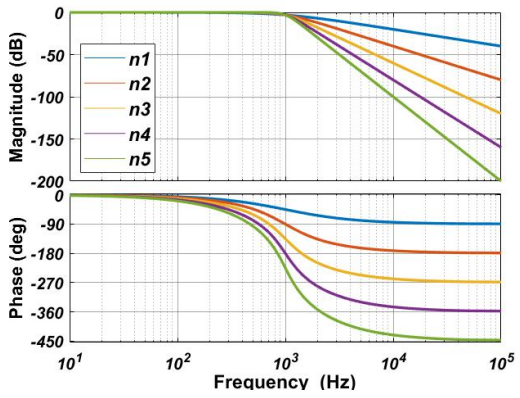

(a)

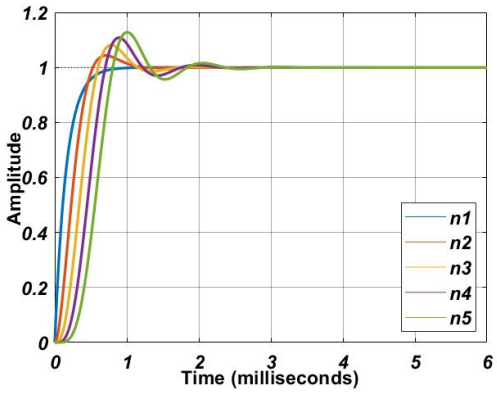

(b)

Figure 7.29: *Frequency responses and step responses of the resonator based on parameters given in Table 7.6 and target bandwidth of 1000 Hz. n is system order which is one number higher than the PLL's LPF order.*

7.9. Step responses

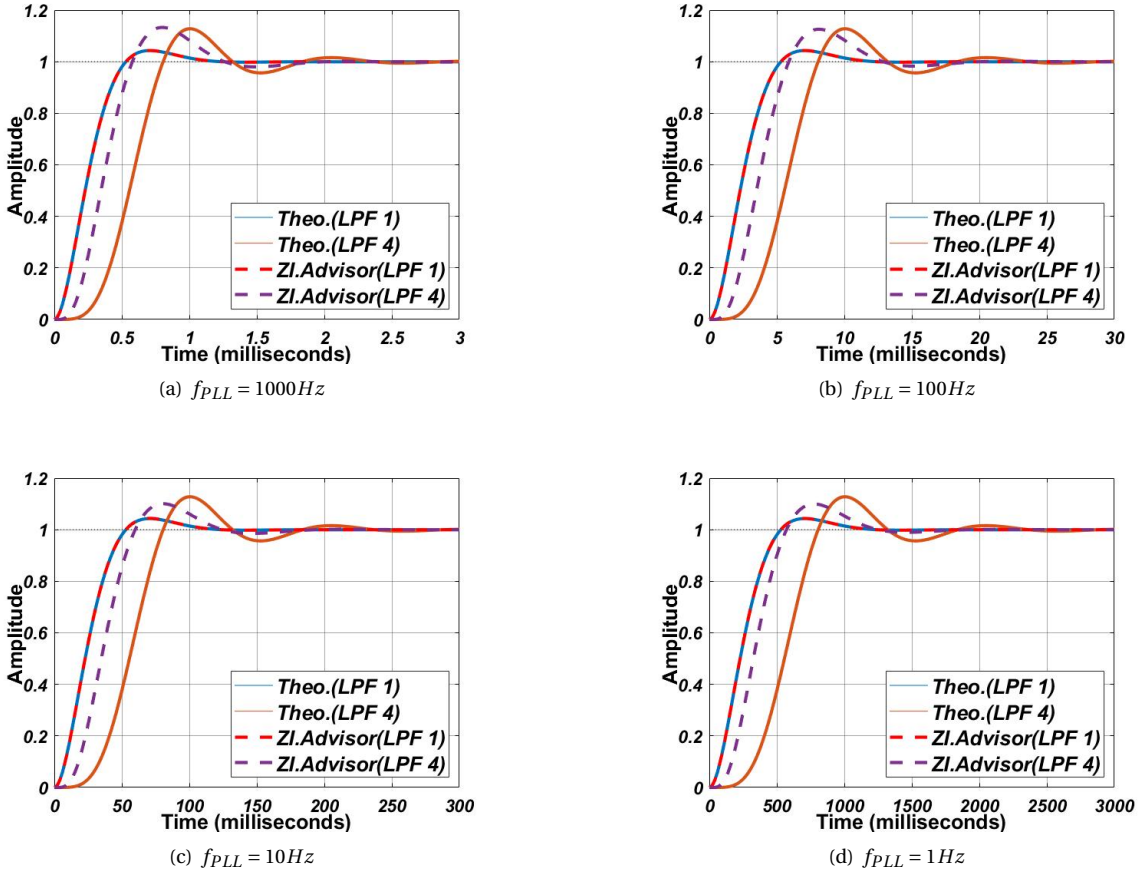

(a) $f_{PLL} = 1000Hz$ (b) $f_{PLL} = 100Hz$

(c) $f_{PLL} = 10Hz$ (d) $f_{PLL} = 1Hz$

Figure 7.30: *Comparison between the theoretical step responses (based on the transfer function which was obtained in Section 7.8) and the experimental ones using Lock-in amplifier for different PLL bandwidths. In each PLL bandwidth, the theoretical and experimental systems overlapped in case of LPF1. In this case, the settling times to within* 5% *were equal to* 0.465 ms, 4.65 ms, 46.5 ms *and* 465 ms *for the corresponding* f_{PLL} *of* 1000 Hz, 100 Hz,10 Hz *and* 1 Hz *respectively. However, the experimental systems responded faster in case of LPF4. This is mainly due to use of "PLL advisor" of the Lock-in amplifier instead of inputting the theoretically needed values of the PLL parameters. While we obtained the step responses based on the transfer function of the system, the advisor of the Lock-in amplifier determines the PLL parameters based on the actual system and considers input to output delay of the system. Therefore, this discrepancy between the step responses are understandable. In case of LPF4, the settling times to within* 5% *were equal to* 1.1 ms, 11 ms, 110 ms *and* 1010 ms *(for experimental systems), and* 1.22 ms, 12.2 ms, 122 ms *and* 1220 ms *(for theoretical systems) for the corresponding* f_{PLL} *of* 1000 Hz, 100 Hz,10 Hz *and* 1 Hz *respectively.*

7.10. Fluids dilution process

Two different types of NPs used in experiments: Gold NPs and Polystyrene NPs. Polystyrene NPs of 800 nm from SIGMA were suspended in a 1 mL DI water when we received. Gold NPs of 100nm diameter with Polyvinylpyrrolidone (PVP) surfactant from nanoComposix arrived at university, while they were suspended in DI water of 50 mL. It was claimed that PVP is a large polymer that covers the particle surface and provides stability when particles are exposed to a variety range of solvent with salt and pH. However, DI water is considered as a safe solvent for that.
To dilute and obtain the desire volume and concentration, $C_1 \times V_1 = C_2 \times V_2$ relation was used with stress on the lowest available pipette volume at the chemistry lab (2 µL) and needed volume of fluid for experiments (≈5 mL). Definitions and procedures are given in Tables 7.7 to 7.9.

Table 7.7: *Parameters and definition for dilution process*

Parameter	Gold nanoparticle	Polystyrene nanoparticle
Diameter (nm)	100	800
Stock Mass concentration ($mg\,mL^{-1}$)	0.05	-
Stock Weight concentration	-	0.1
C_1 =Particle concentration (particles mL^{-1})	4.94×10^9	3.57×10^{11}
C_2 =Needed concentration (particles mL^{-1})	1.022×10^7	1.022×10^7
V_1 =Removed volume from stock (mL)	As low as possible	As low as possible
V_2 =Needed volume (mL)	≈ 5 mL	≈ 5 mL

Table 7.8: *Dilution process of gold nanopatilces of 100 nm diameter*

Dilution	V1 (mL)	C1 (particles mL^{-1})	DI Water (mL)	V2 (mL)	C2 (particles mL^{-1})
1	1×10^{-2}	4.94×10^9	4.824	4.834	1.022×10^7

Table 7.9: *Dilution process of Polystyrene nanoparticles of 800 nm diameter*

Dilution	V1 (mL)	C1 (particles mL^{-1})	DI Water (mL)	V2 (mL)	C2 (particles mL^{-1})
1	2×10^{-3}	3.57×10^{11}	0.998	1	7.141×10^8
2	7×10^{-2}	7.141×10^8	4.82	4.89	1.022×10^7

7.11. SMR filling scene

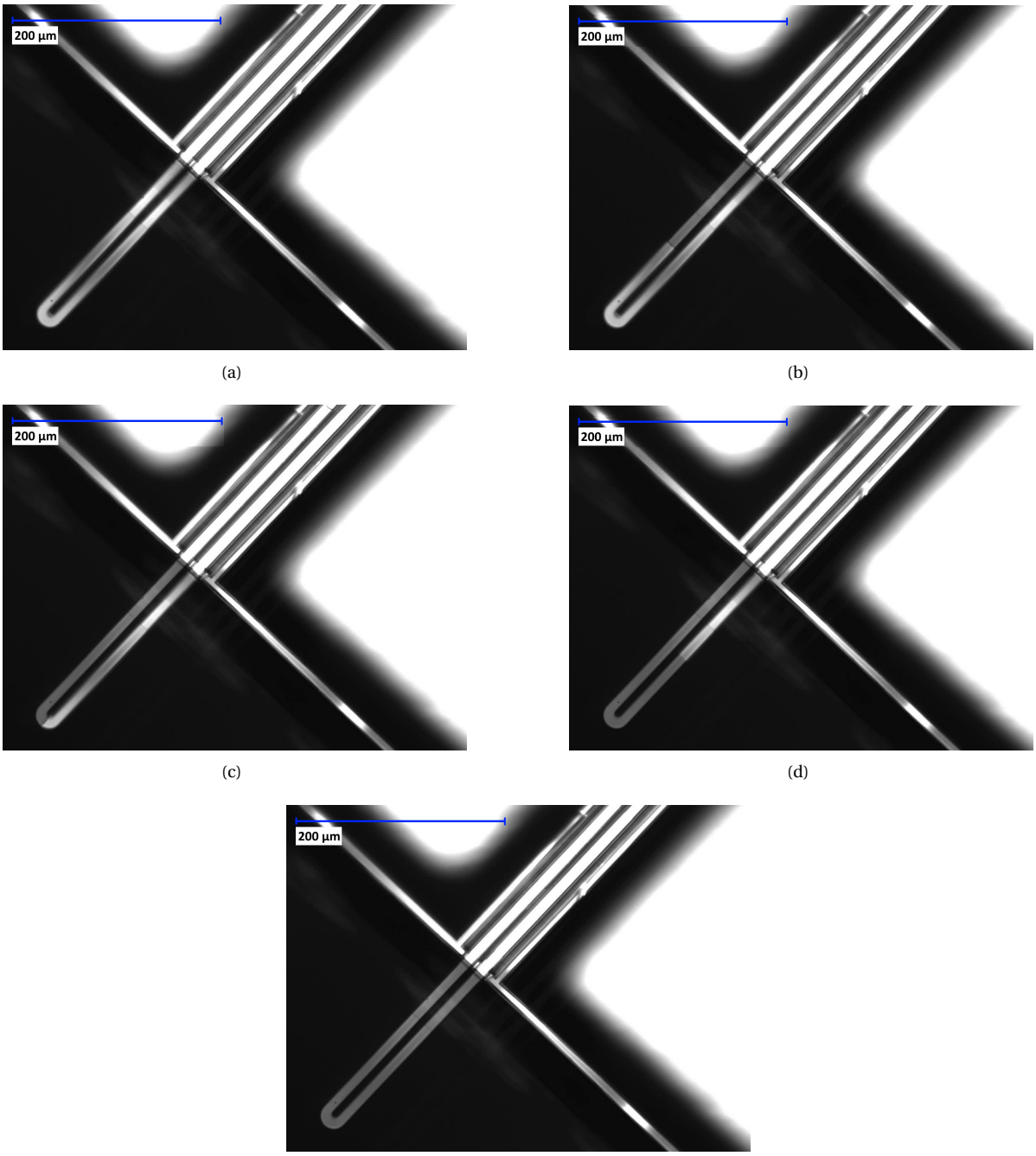

(a) (b) (c) (d) (e)

Figure 7.31: *Suspended hollow cantilever being filled with liquid from left-leg to right-leg. The cantilever becomes dark when it is filled. The snapshots were taken when a) the cantilever was empty, b) the left leg was half-filled, c) the left leg was totally filled and the right leg was empty, d) the right leg was also filled in half and e) both legs were totally filled.*

7.12. Allan deviation and mass detection limit

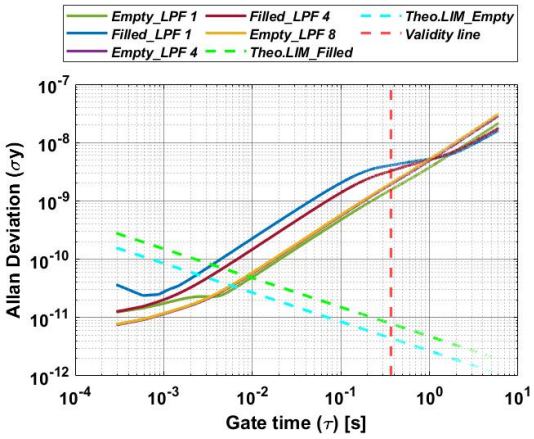

(a) Bending1

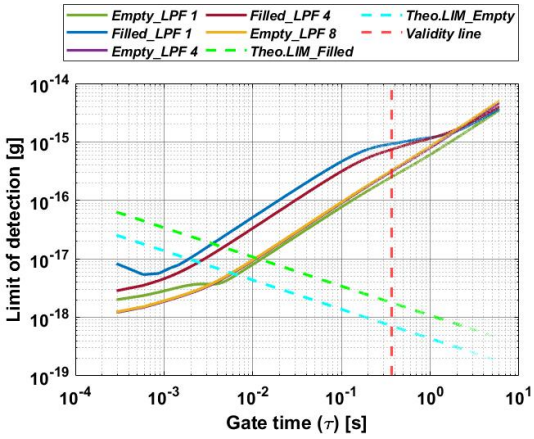

(b) Bending1

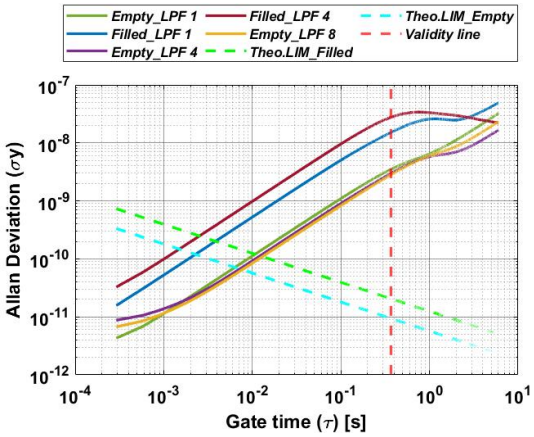

(c) Bending2

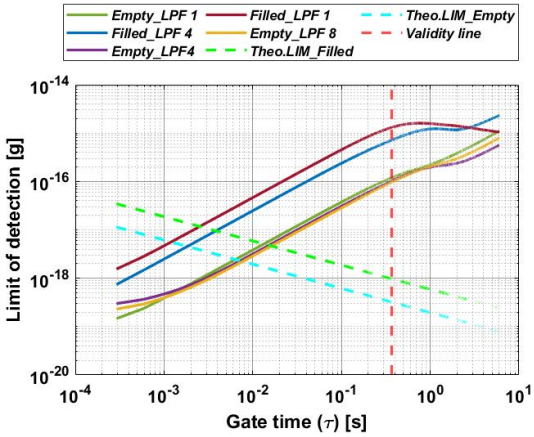

(d) Bending2

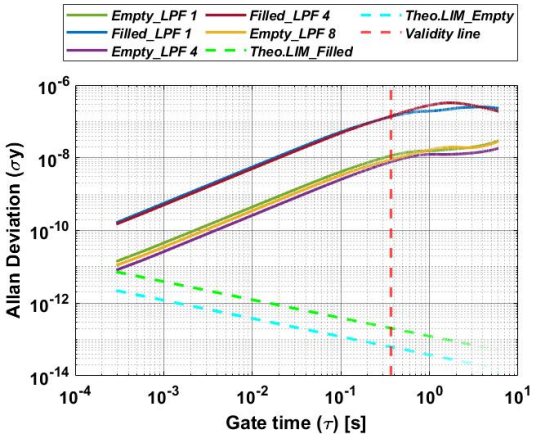

(e) Torsional

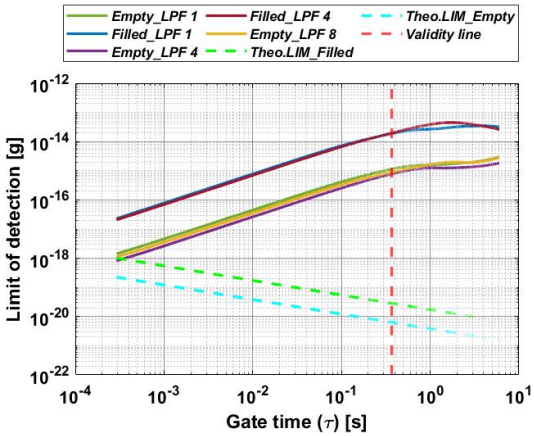

(f) Torsional

Figure 7.32: *Allan deviation (on the left) and limit of detection (on the right) for different modes with f_{PLL}=1 Hz. The "Validity line" determines the lowest averaging time that our system can provide. Therefore, longer averaging times than the validity line are region of interest in graphs. "Theo.LIM" stands for theoretical limit. It represents the thermomechanical noise level of the system in different gate times.*

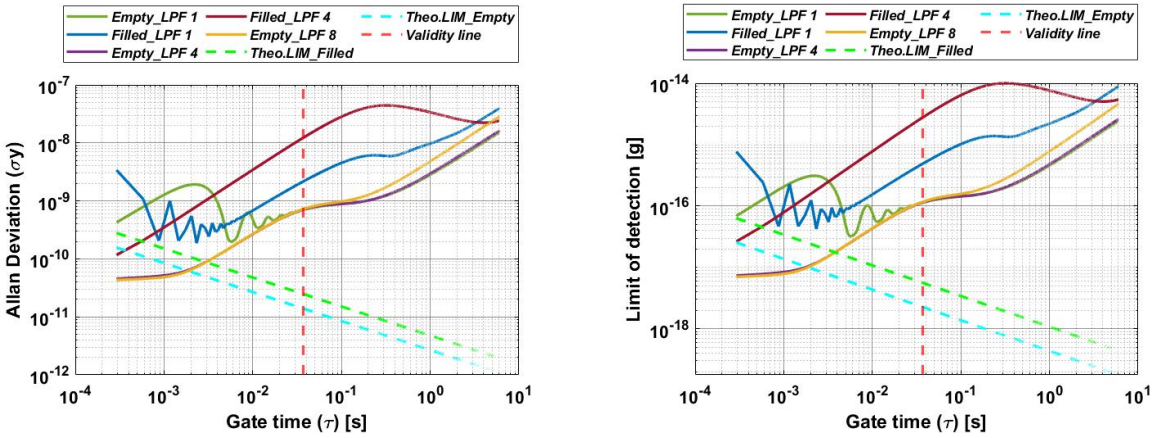

(a) Bending1 (b) Bending1

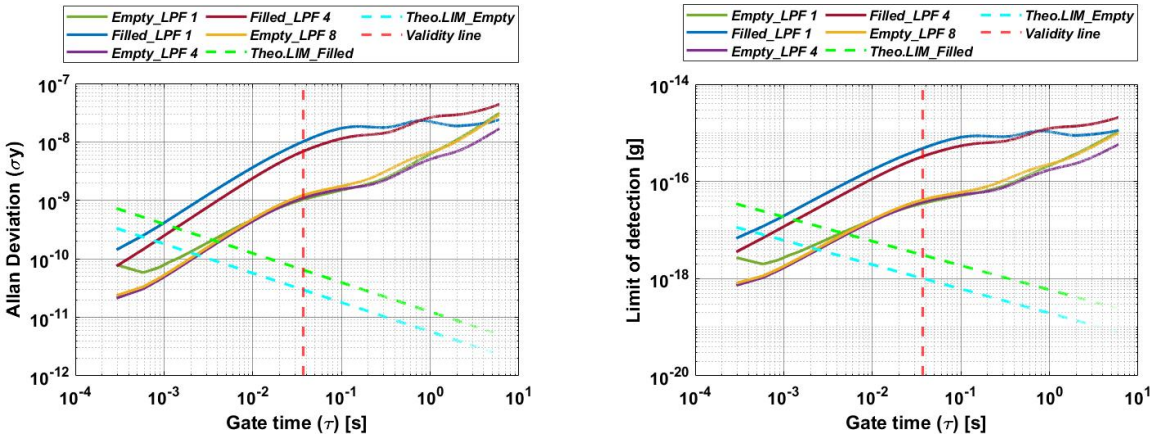

(c) Bending2 (d) Bending2

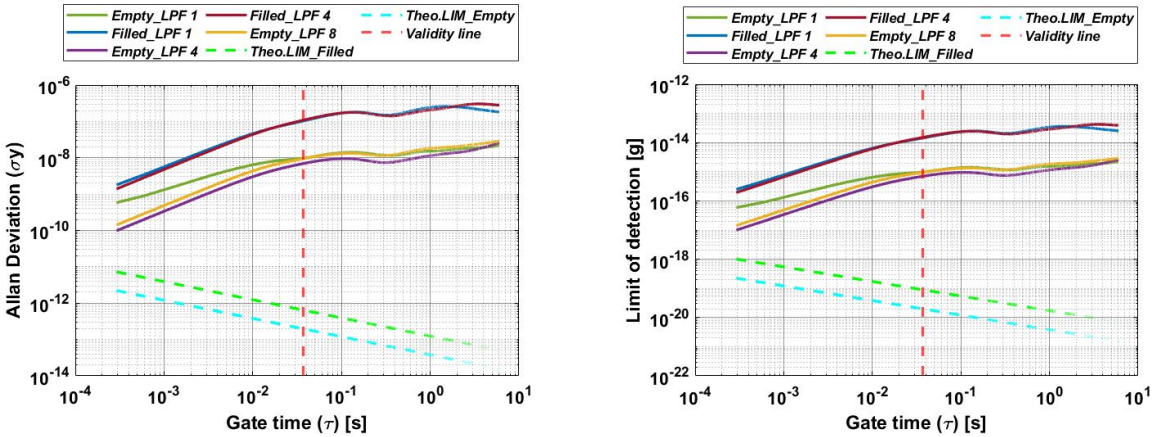

(e) Torsional (f) Torsional

Figure 7.33: *Allan deviation (on the left) and limit of detection (on the right) for different modes with f_{PLL}=10 Hz. The "Validity line" determines the lowest averaging time that our system can provide. Therefore, longer averaging times than the validity line are region of interest in graphs. "Theo.LIM" stands for theoretical limit. It represents the thermomechanical noise level of the system in different gate times.*

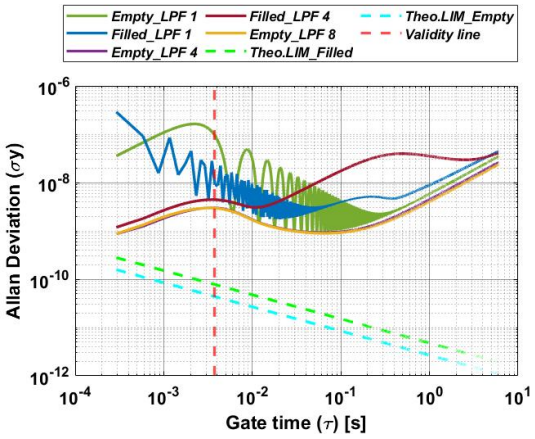

(a) Bending1

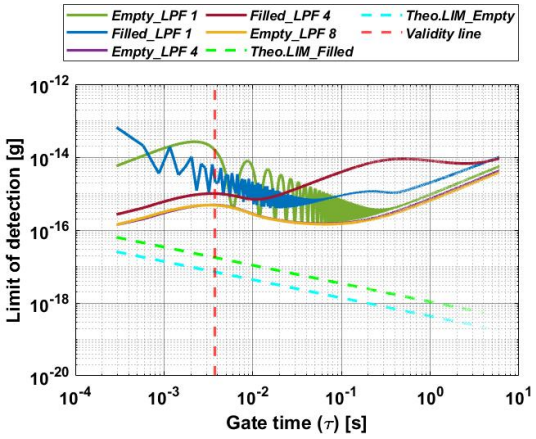

(b) Bending1

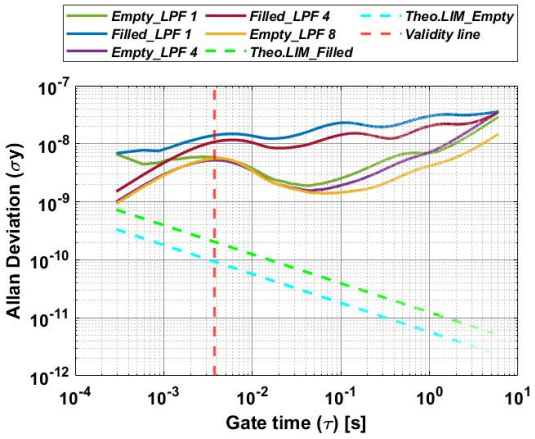

(c) Bending2

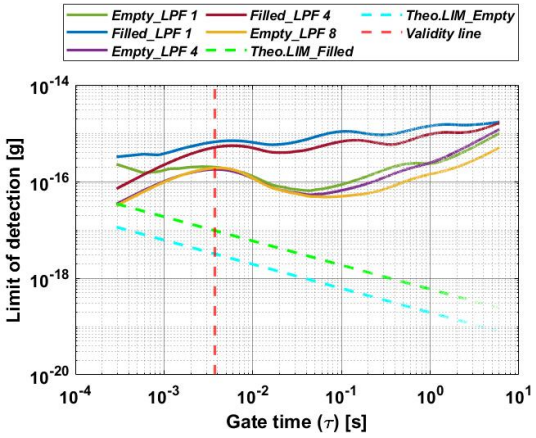

(d) Bending2

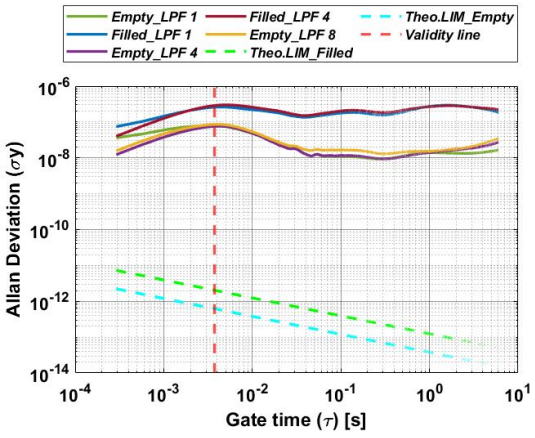

(e) Torsional

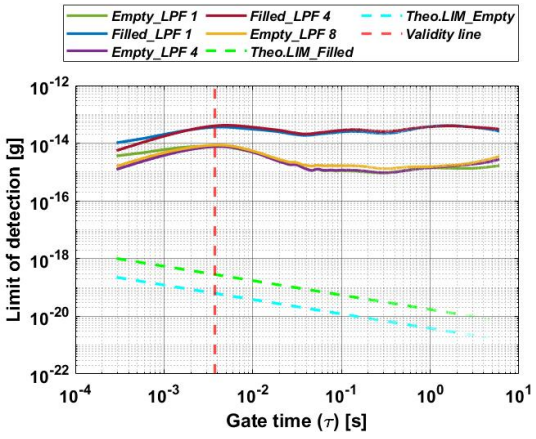

(f) Torsional

Figure 7.34: *Allan deviation (on the left) and limit of detection (on the right) for different modes with f_{PLL}=100 Hz. The "Validity line" determines the lowest averaging time that our system can provide. Therefore, longer averaging times than the validity line are region of interest in graphs. "Theo.LIM" stands for theoretical limit. It represents the thermomechanical noise level of the system in different gate times.*

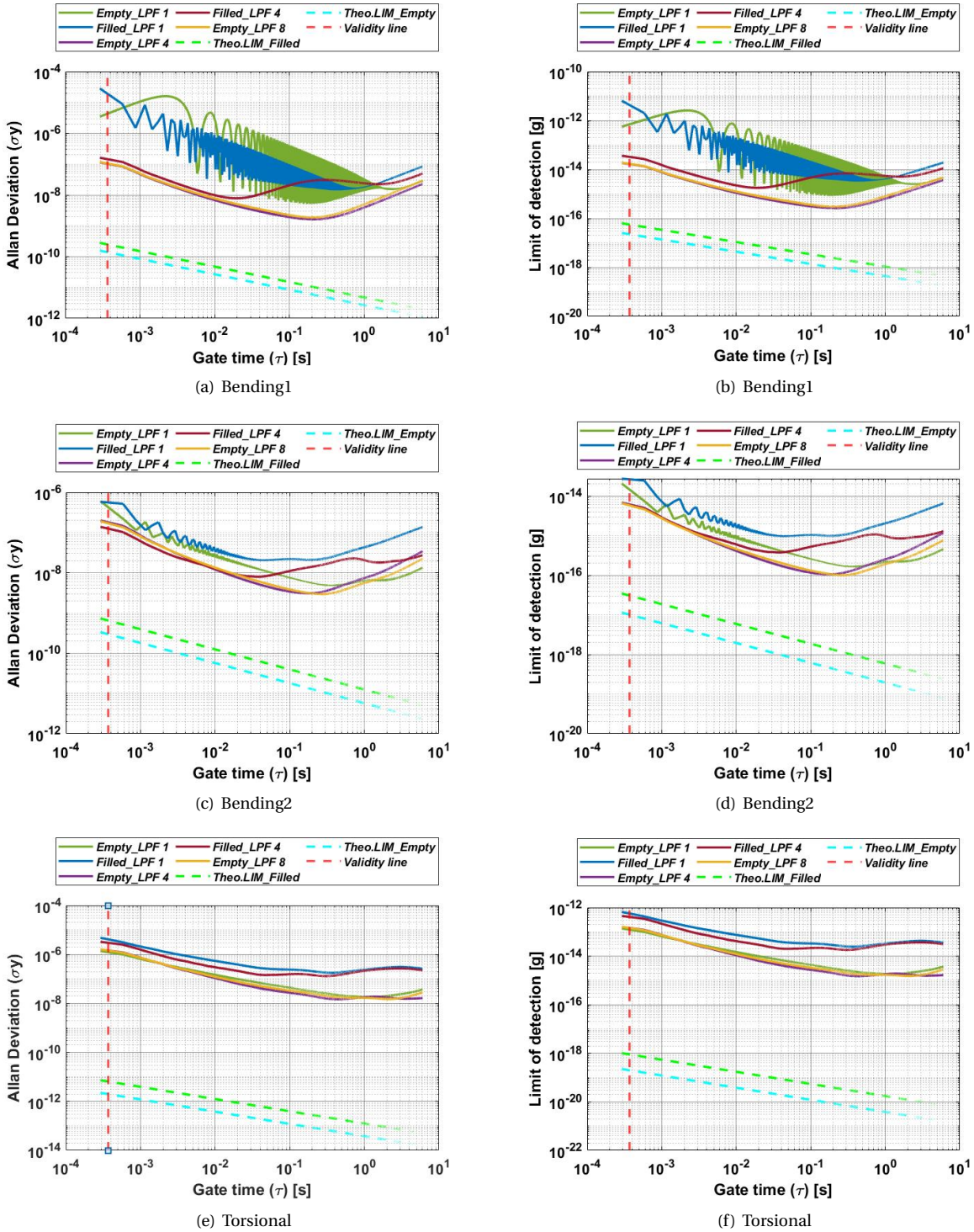

(a) Bending1

(b) Bending1

(c) Bending2

(d) Bending2

(e) Torsional

(f) Torsional

Figure 7.35: *Allan deviation (on the left) and limit of detection (on the right) for different modes with f_{PLL}=1000 Hz. The "Validity line" determines the lowest averaging time that our system can provide. Therefore, longer averaging times than the validity line are region of interest in graphs. "Theo.LIM" stands for theoretical limit. It represents the thermomechanical noise level of the system in different gate times.*

7.13. Introducing nanoparticles into the SMR

The experiments always started with a low driven pressure difference such as 70 mbar, however no fluid movements could be seen at the inlet of fluidic channels. Therefore, driven pressure difference increased until fluid entry was confirmed. Since no flow could be detected visually or by the flow rate sensor, the pressure at the inlet was repeatedly increased.

Two devices were used for conducting this experiment. First device, which lasted only 2 hours during this experiment and broke from a corner of on-chip fluidic channel, was the one that had survived from the Allan deviation experiments (thus it had worked for two consecutive days). This device only used for gold nanoparticles. Second device, with the same material and dimensions of the first device, was operative in total 4 hours in two days and used for measurements of polystyrene beads. Introducing nanoparticles in the first device was done 7 days after the primary experiments, while this was only 1 day for the second device. This delay led to blockage in fluidic channel, hence higher driven pressure was applied such as 500 mbar or 1200 mbar for having fluid stream. It was noticed that this blockage due to particles aggregation or dirt led to change in resonance frequency and m_{eff} of the cantilever on the day of conducting the experiment. Assuming that k_{eff} remained constant, a comparison of values in first bending mode is given in Table 7.10.

Table 7.10: *Resonator's parameters comparison in a period of 7 days between two experiments.*

Parameter	Only DI water	DI water+Au particles
f_r $[kHz]$	126.393	119.4522718
Q [-]	9716	8850
m_{eff} $[g]$	1.133×10^{-7}	1.268×10^{-7}

In case of gold nanoparticles, due to suffering from cracks in fluidic channels after 2 hours operation, only the first bending mode was examined. The PLL configuration was set as follows: f_{PLL}=100 HZ and f_{LPF}=141 Hz, while fluid pressure difference was set to 500 mbar and 1200 mbar (see Figs. 7.36 and 7.37).

In case of polystyrene nanoparticles, second device was employed. During 2 hours operating time of this device, the second bending mode (f_r = 711.7 KHz, Q=1220 and m_{eff} = 2.69×10^{-8} g) was used with a PLL configuration of f_{PLL}=100 HZ and f_{LPF}=141 Hz, while fluid pressure difference was set to i) 100 mbar, ii) 200 mbar and iii) 400 mbar (see Figs. 7.38 to 7.40).

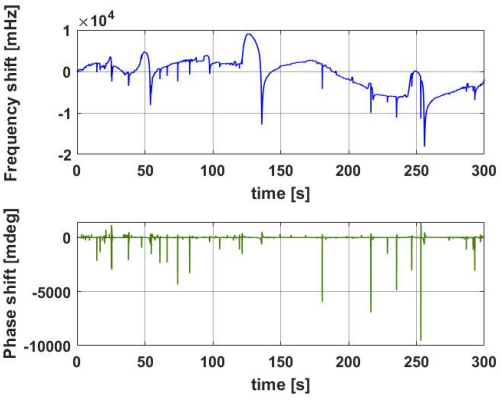

(a)

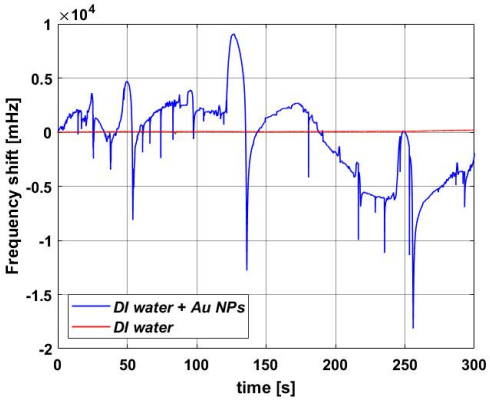

(b)

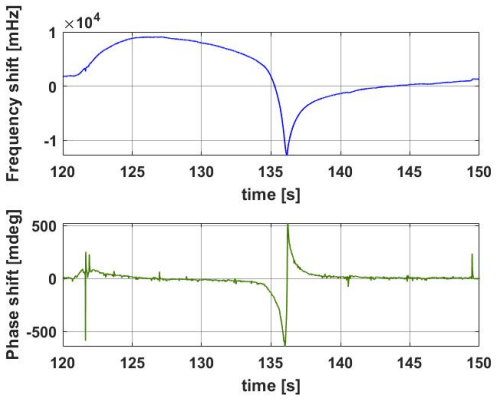

(c)

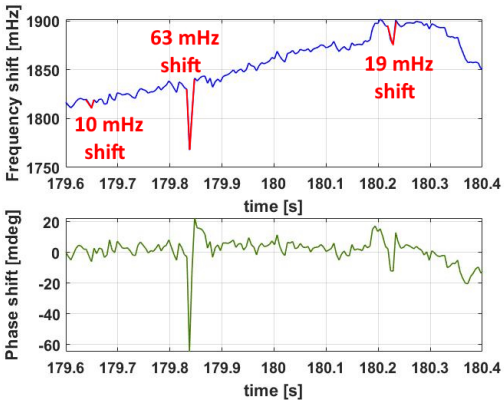

(d)

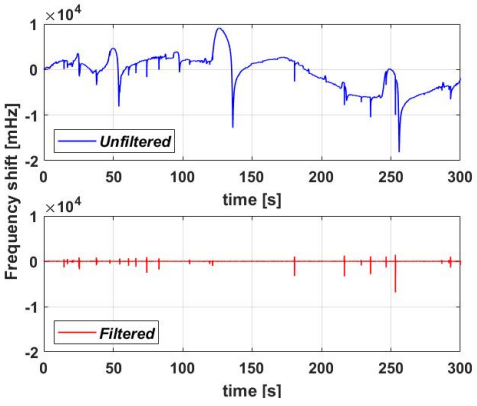

(e)

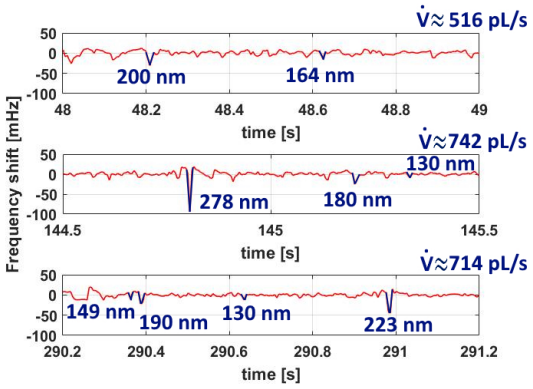

(f)

Figure 7.36: *Mass measurement's graphs of gold nanoparticles with f_{PLL}=100 Hz, fluid driven pressure of 500 mbar and averaging time of 5 ms. (a) Raw data of frequency shift and phase shift measurement for 5 minutes, (b) Frequency shifts comparison between two solutions: DI water with and without gold nanoparticles, (c) An example of large frequency variations (seen in (a)) with its phase shift, (d) An example of small frequency shifts that corresponds transition of gold nanoparticles, (e) Comparison between raw data and filtered data, (f) Few examples of detected buoyant mass and corresponding equivalent particles diameters.*

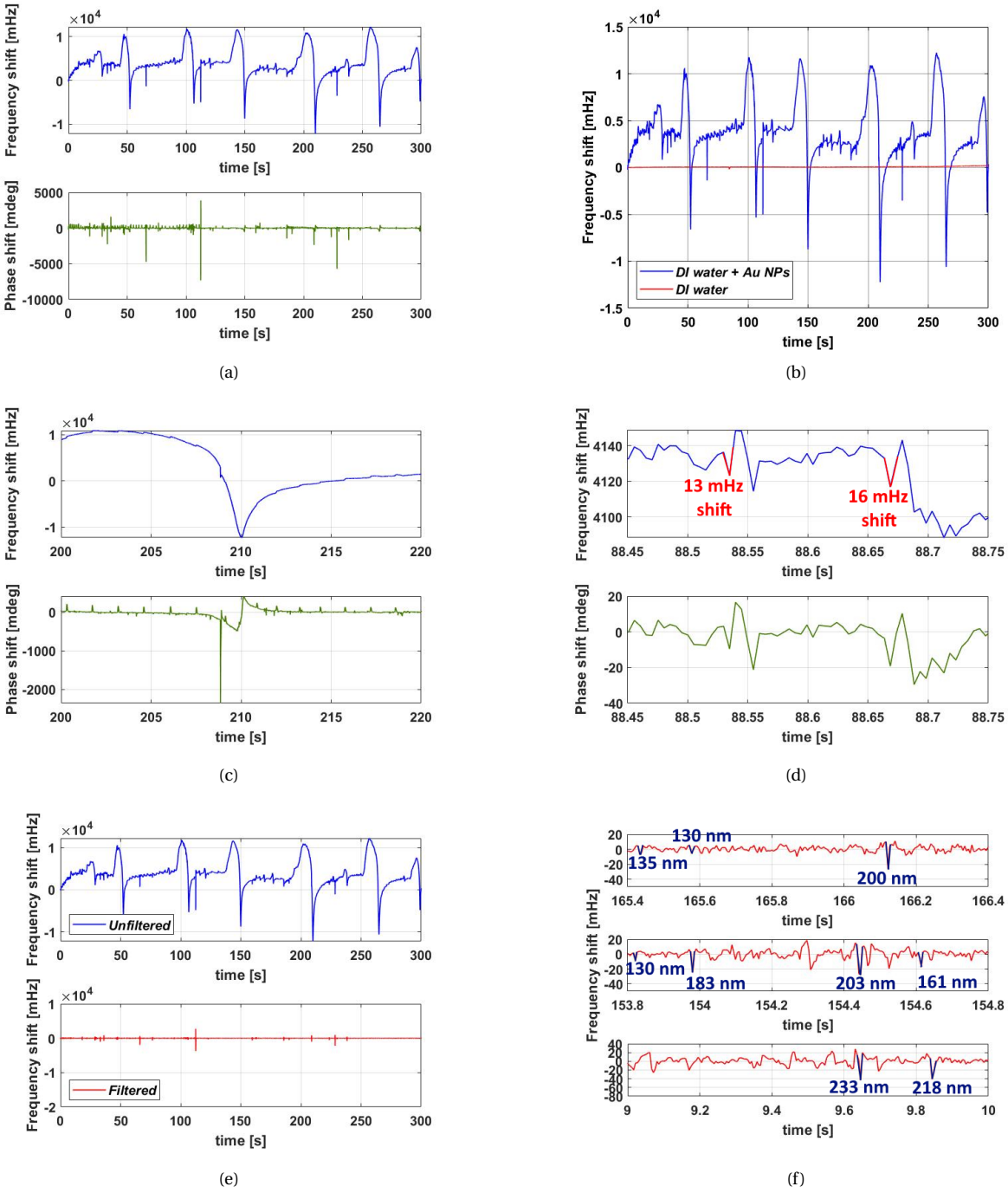

Figure 7.37: *Mass measurement's graphs of gold nanoparticles with f_{PLL}=100 Hz, fluid driven pressure of 1200 mbar and averaging time of 5 ms. (a) Raw data of frequency shift and phase shift measurement for 5 minutes, (b) Frequency shifts comparison between two solutions: DI water with and without gold nanoparticles, (c) An example of large frequency variations (seen in (a)) with its phase shift, (d) An example of small frequency shifts that corresponds transition of gold nanoparticles, (e) Comparison between raw data and filtered data, (f) Few examples of detected buoyant mass and corresponding equivalent particles diameters.*

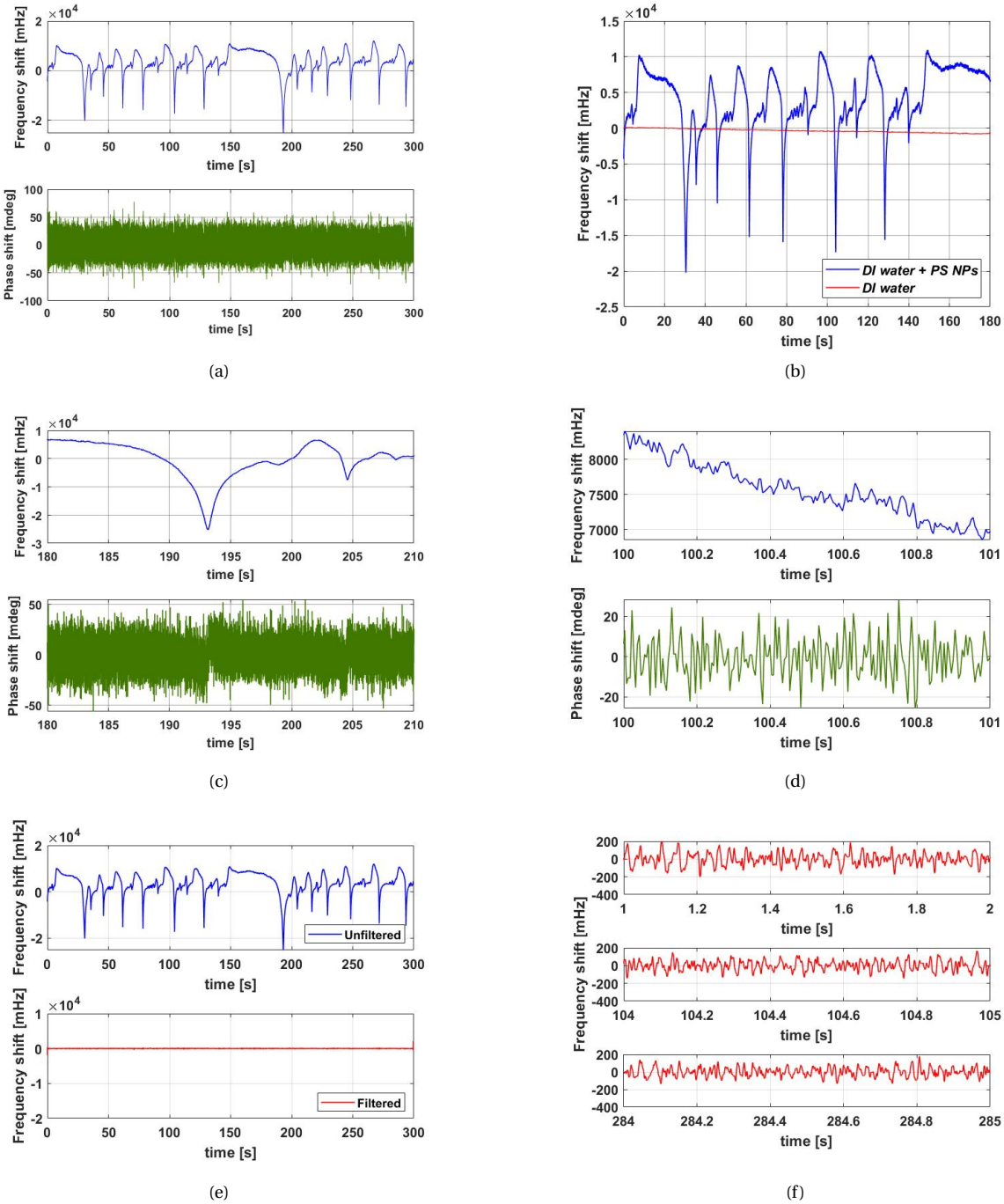

Figure 7.38: *Mass measurement's graphs of polystyrene nanoparticles with f_{PLL}=100 Hz, fluid driven pressure of 100 mbar and averaging time of 5 ms. (a) Raw data of frequency shift and phase shift measurement for 5 minutes, (b) Frequency shifts comparison between two solutions: DI water with and without polystyrene nanoparticles, (c) An example of large frequency variations (seen in (a)) with its phase shift, (d) An example of small frequency shifts that seem to be noise, (e) Comparison between raw data and filtered data, (f) Three examples of filtered data, however particles profiles can not be distinguished.*

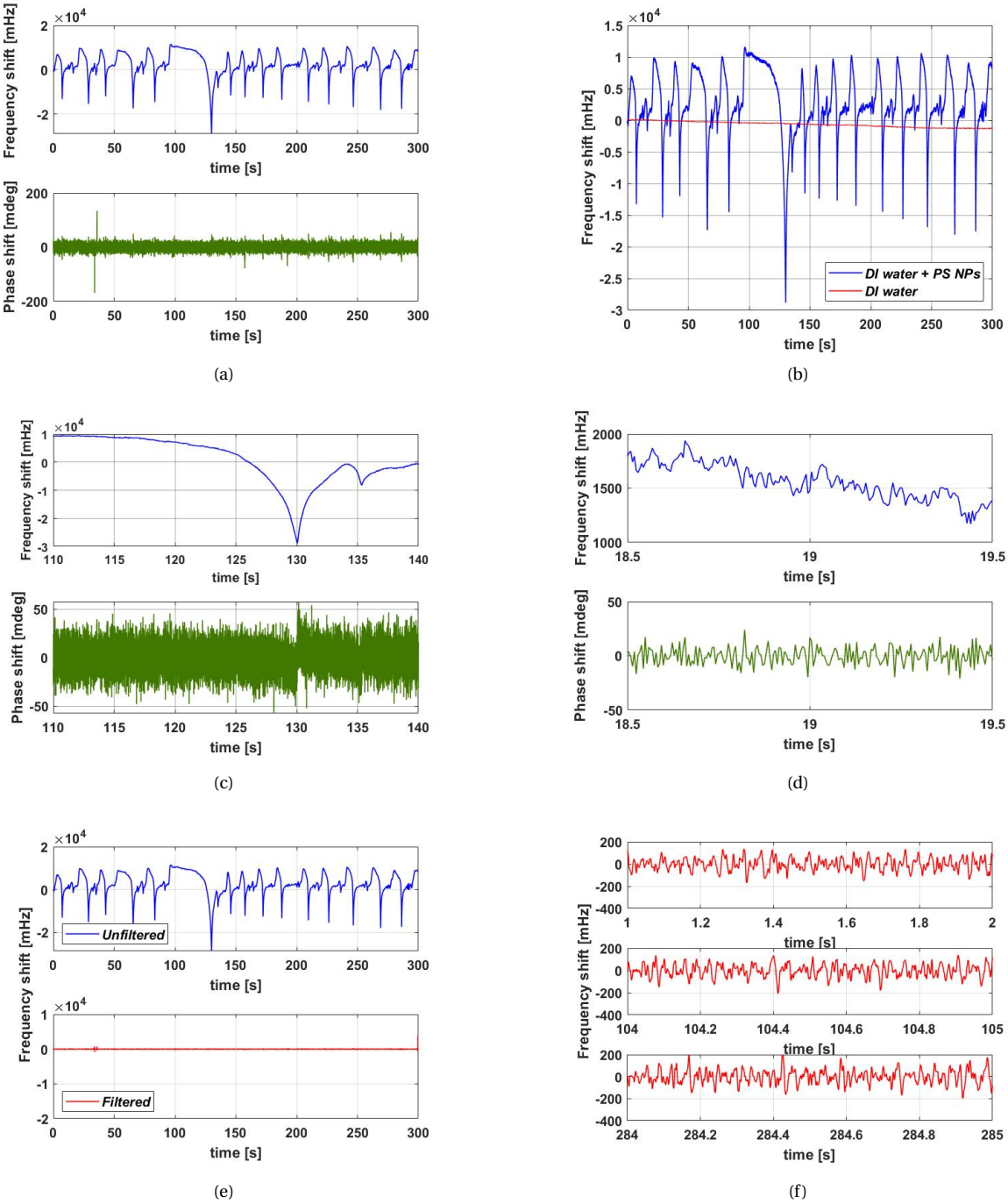

Figure 7.39: *Mass measurement's graphs of polystyrene nanoparticles with f_{PLL}=100 Hz, fluid driven pressure of 200 mbar and averaging time of 5 ms. (a) Raw data of frequency shift and phase shift measurement for 5 minutes, (b) Frequency shifts comparison between two solutions: DI water with and without polystyrene nanoparticles, (c) An example of large frequency variations (seen in (a)) with its phase shift, (d) An example of small frequency shifts that seem to be noise, (e) Comparison between raw data and filtered data, (f) Three examples of filtered data, however particles profiles can not be distinguished.*

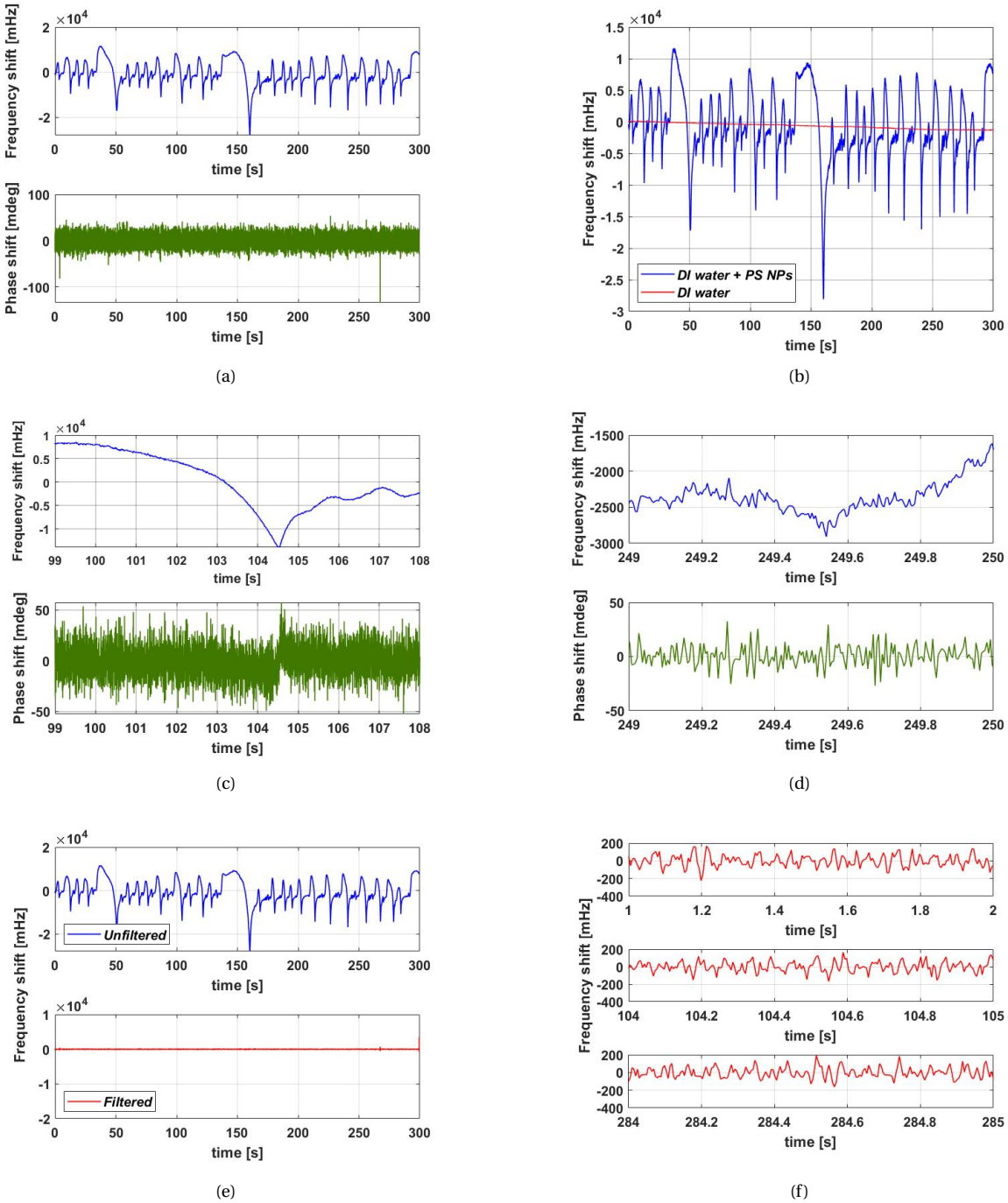

Figure 7.40: *Mass measurement's graphs of polystyrene nanoparticles with f_{PLL}=100 Hz, fluid driven pressure of 400 mbar and averaging time of 5 ms. (a) Raw data of frequency shift and phase shift measurement for 5 minutes, (b) Frequency shifts comparison between two solutions: DI water with and without polystyrene nanoparticles, (c) An example of large frequency variations (seen in (a)) with its phase shift, (d) An example of small frequency shifts that seem to be noise, (e) Comparison between raw data and filtered data, (f) Three examples of filtered data, however particles profiles can not be distinguished.*

8

Conclusion

This project has obtained its expected outputs which were the determination of the mass detection limit and detection speed of the silicon dioxide SMR. The expected outcomes of this project were detection of gold and polystyrene nanoparticles suspended in DI water and detection of nanoparticles suspended in environmental samples. This project has also partially gained its outcomes, which were proof of nanoparticles (gold and polystyrene) detection. However, the entire outputs of this project will be achievable, if the recommendations of this project (see Section 8.2) are taken into account.

8.1. Research questions answers

- ***Can the fabricated silicondioxide SMR at TUDelft enhanced with the PLL control system detect nanoplastic particles?***

This research revealed that the fabricated chip is barely capable of measuring nanopaticle's mass in a flow-through mode. This chip, in most cases, cannot mechanically tolerate working in a simple vacuum environment. This is mainly due to the lack of stiffness on fluidic channels and not the cantilever itself, which results in fractures on channels even before entering fluid. However, during the two opportunities, we detected gold nanoparticles. Therefore, there are no reasons not being able to detect plastic nanoparticles if the research recommendations are considered for future experiments and improvements.

- ***What is the performance of silicondioxide SMR in terms of mass limit detection and maximum detection speed?***

The lowest mass can be detected at averaging times between 20 ms and 400 ms using the second bending mode, first bending mode and first torsional mode respectively. The lowest resolved mass for an empty and a water-filled resonator using second bending mode was 0.11 fg and 0.38 fg respectively, using a PLL bandwidth of 1000 Hz. The maximum speed of detection is determined by the PLL bandwidth. The higher the bandwidth is, the faster is the detection. This detection speed is 0.37 ms and 3.7 ms for 1000 Hz and 100 Hz respectively.

8.2. Recommendations

- **Improving strength of micro-fluidic channels.**
  Unfortunately, two third of the current devices suffered from fractures on micro-fluidic channels (not on the cantilever itself, but on the on-chip microchannel) as soon as they were placed in a vacuum environment. This shows the necessity of revision in design and fabrication of this device. There will be no experiments and results, when there is no operative devices.

- **Providing a highly sensitive flow rate sensor.**
  Not having a valid confirmation for fluid flow in the channels was one of the reasons that we were forced to use high pressure differences to regulate flow. We would be more confident about the effect of pressure on variations of frequency over time if we could have monitored the flow rate.

- **Validating the concentration and the particles sizes in solutions.**
  As long as we cannot test particles sizes and their concentrations in a liquid solution that was used for measurements by our SMR, we cannot ensure about what we have obtained as mass of particles. It is recommended having access to a DLS system at our university (if it is available) or outside.

- **Equipping our data processing with matched filter method.**
  To provide automatic peak detection from the raw data, match filtering technique could be useful. Matched filtering method is a convolution method in signal processing, in which a template function is defined in such a way that it is only sensitive to the peak profiles of the particles with different mass and the rest will not be detected.

8.3. Self reflection

I started this project by having a literature survey on plastic nanoparticles and currently existed methods of characterization. I learned about techniques that later I never used them during the project or even never was asked during the literature survey presentation, but instead, I was asked about PLL that I had not studied it completely until that time. Moreover, until the end of project, I only had one opportunity to test polystyrene nanoparticles using our device and that lasted for less than two hours. This tells me that project's goal and title were defined very unrealistic at the beginning. This made me frustrated when I saw that not having a good device (I was not responsible for its fabrication) has jeopardized obtaining even primary results.

During weekly meetings, we mainly discussed the obtained results or encountered problems of the last week. Therefore, I had to organize stuff in some slides. The slides and comments that I put on them helped me until the last day. This highlighted the importance of internal communication and feedback in a group, which is the safest place for committing mistakes and learning from them.

In total, this project provided me with experiences not only in technical filled but in self management and project management.

Bibliography

[1] Department of Physics, The Chinese University of Hong Kong. *Basic principle of transmission electron microscope*, 2019. URL http://www.hk-phy.org/atomic_world/tem/tem02_e.html.

[2] Malvern Panalytical Ltd. *Static Light Scattering technologies for GPC - SEC explained [White paper]*, 2018. URL https://www.malvernpanalytical.com/en/assets/WP130627SLSTechnologiesGPCSECExplained-6_tcm50-52602.pdf.

[3] Malvern Panalytical Ltd. *Zetasizer Ultra World's most advanced light scattering system*, 2019. URL https://www.malvernpanalytical.com/en/products/product-range/zetasizer-range/zetasizer-ultra.

[4] Shimadzu Corporation. *UV-VIS Spectrophotometer UV-1900i*, 2019. URL https://www.shimadzu.com/an/sites/shimadzu.com.an/files/ckeditor/an/spectro/uv/1900i/c101e168.pdf.

[5] Thermo Fisher Scientific Inc. *Thermo Scientific 253 Plus*, 2016. URL https://assets.thermofisher.com/TFS-Assets/CMD/brochures/BR-30333-IRMS-253-Plus-BR30333-EN.pdf.

[6] Priscila Alessio, Pedro H.B. Aoki, Leonardo N. Furini, Alvaro E. Aliaga, and Carlos J. Leopoldo Constantino. 3 - spectroscopic techniques for characterization of nanomaterials. In Alessandra L. Da Róz, Marystela Ferreira, Fabio de Lima Leite, and Osvaldo N. Oliveira, editors, *Nanocharacterization Techniques*, Micro and Nano Technologies, pages 65 – 98. William Andrew Publishing, 2017. ISBN 978-0-323-49778-7. doi: https://doi.org/10.1016/B978-0-323-49778-7.00003-5. URL http://www.sciencedirect.com/science/article/pii/B9780323497787000035.

[7] David W Allan, Neil Ashby, and Clifford C Hodge. *The science of timekeeping*. Hewlett-Packard, 1997.

[8] G.V. Andrievsky, V.K. Klochkov, A.B. Bordyuh, and G.I. Dovbeshko. Comparative analysis of two aqueous-colloidal solutions of c60 fullerene with help of ftir reflectance and uv–vis spectroscopy. *Chemical Physics Letters*, 364(1):8 – 17, 2002. ISSN 0009-2614. doi: https://doi.org/10.1016/S0009-2614(02)01305-2. URL http://www.sciencedirect.com/science/article/pii/S0009261402013052.

[9] J. L. Arlett and M. L. Roukes. Ultimate and practical limits of fluid-based mass detection with suspended microchannel resonators. *Journal of Applied Physics*, 108(8):084701, 2010. doi: 10.1063/1.3475151. URL https://doi.org/10.1063/1.3475151.

[10] Paul A.Tipler and Gene Mosca. Chapter 34 - wave-particle duality and quantum physics. In *Physics for Scientists and Engineers*, pages 1173 – 1202. W.H.Freeman and Company, 2008. ISBN 978-1-4292-0265-7.

[11] Colin N Banwell, Elaine M McCash, et al. *Fundamentals of molecular spectroscopy*, volume 851. McGraw-Hill New York, 1994.

[12] J. A. Barnes, A. R. Chi, L. S. Cutler, D. J. Healey, D. B. Leeson, T. E. McGunigal, J. A. Mullen, W. L. Smith, R. L. Sydnor, R. F. C. Vessot, and G. M. R. Winkler. Characterization of frequency stability. *IEEE Transactions on Instrumentation and Measurement*, IM-20(2):105–120, 1971.

[13] Prabir Basu. 14. analytical techniques. In *Biomass Gasification, Pyrolysis and Torrefaction - Practical Design and Theory (3rd Edition)*. Elsevier, 2018. ISBN 978-0-12-812992-0. doi: http://dx.doi.org/10.1016/B978-0-12-812992-0.00023-6. URL https://app.knovel.com/hotlink/khtml/id:kt00CYVRN1/biomass-gasification/analytical-techniques.

[14] P. Belardinelli, M.K. Ghatkesar, U. Staufer, and F. Alijani. Linear and non-linear vibrations of fluid-filled hollow microcantilevers interacting with small particles. *International Journal of Non-Linear Mechanics*, 93:30 – 40, 2017. ISSN 0020-7462. doi: https://doi.org/10.1016/j.ijnonlinmec.2017.04.016. URL http://www.sciencedirect.com/science/article/pii/S002074621630364X.

[15] Vu Thien Binh, N. Garcia, and A.L. Levanuyk. A mechanical nanosensor in the gigahertz range: where mechanics meets electronics. *Surface Science*, 301(1):L224 – L228, 1994. ISSN 0039-6028. doi: https://doi.org/10.1016/0039-6028(94)91277-7. URL http://www.sciencedirect.com/science/article/pii/0039602894912777.

[16] Pratim Biswas and Chang-Yu Wu. Nanoparticles and the environment. *Journal of the Air & Waste Management Association*, 55(6):708–746, 2005. doi: 10.1080/10473289.2005.10464656. URL https://doi.org/10.1080/10473289.2005.10464656.

[17] Robert D Blevins. *Formulas for dynamics, acoustics and vibration*. John Wiley & Sons, 2015. ISBN 9781119038139.

[18] Hans Bouwmeester, Peter C. H. Hollman, and Ruud J. B. Peters. Potential health impact of environmentally released micro- and nanoplastics in the human food production chain: Experiences from nanotoxicology. *Environmental Science & Technology*, 49(15):8932–8947, 2015. doi: 10.1021/acs.est.5b01090. URL https://doi.org/10.1021/acs.est.5b01090. PMID: 26130306.

[19] Satinder K. Brar and M. Verma. Measurement of nanoparticles by light-scattering techniques. *TrAC Trends in Analytical Chemistry*, 30(1):4 – 17, 2011. ISSN 0165-9936. doi: https://doi.org/10.1016/j.trac.2010.08.008. URL http://www.sciencedirect.com/science/article/pii/S0165993610002700. Characterization, Analysis and Risks of Nanomaterials in Environmental and Food Samples.

[20] Mark Anthony Browne, Phillip Crump, Stewart J. Niven, Emma Teuten, Andrew Tonkin, Tamara Galloway, and Richard Thompson. Accumulation of microplastic on shorelines woldwide: Sources and sinks. *Environmental Science & Technology*, 45(21):9175–9179, 2011. doi: 10.1021/es201811s. URL https://doi.org/10.1021/es201811s. PMID: 21894925.

[21] Andrea K Bryan, Vivian C Hecht, Wenjiang Shen, Kristofor Payer, William H Grover, and Scott R Manalis. Measuring single cell mass, volume, and density with dual suspended microchannel resonators. *Lab on a Chip*, 14(3):569–576, 2014. doi: 10.1039/C3LC51022K. URL https://doi.org/10.1039/C3LC51022K.

[22] Gurvinder Singh Bumbrah and Rakesh Mohan Sharma. Raman spectroscopy – basic principle, instrumentation and selected applications for the characterization of drugs of abuse. *Egyptian Journal of Forensic Sciences*, 6(3):209 – 215, 2016. ISSN 2090-536X. doi: https://doi.org/10.1016/j.ejfs.2015.06.001. URL http://www.sciencedirect.com/science/article/pii/S2090536X15000477.

[23] T. P. Burg, A. R. Mirza, N. Milovic, C. H. Tsau, G. A. Popescu, J. S. Foster, and S. R. Manalis. Vacuum-packaged suspended microchannel resonant mass sensor for biomolecular detection. *Journal of Microelectromechanical Systems*, 15(6):1466–1476, Dec 2006. ISSN 1941-0158. doi: 10.1109/JMEMS.2006.883568.

[24] Thomas P. Burg, Michel Godin, Scott M. Knudsen, Wenjiang Shen, Greg Carlson, Ken Babcock John S. Foster, and Scott R. Manalis. Weighing of biomolecules, single cells and single nanoparticles in fluid. *Nature*, 446:1066–1069, 2007. doi: 10.1038/nature05741. URL https://doi.org/10.1038/nature05741.

[25] David J. Burleson, Michelle D. Driessen, and R. Lee Penn. On the characterization of environmental nanoparticles. *Journal of Environmental Science and Health, Part A*, 39(10):2707–2753, 2004. doi: 10.1081/ESE-200027029. URL https://doi.org/10.1081/ESE-200027029.

[26] Antonio R Montoro Bustos, Jorge Ruiz Encinar, and Alfredo Sanz-Medel. Mass spectrometry for the characterisation of nanoparticles. *Analytical and bioanalytical chemistry*, 405(17):5637–5643, 2013. doi: https://doi.org/10.1007/s00216-013-7014-y.

[27] Hans-Jürgen Butt, Brunero Cappella, and Michael Kappl. Force measurements with the atomic force microscope: Technique, interpretation and applications. *Surface science reports*, 59(1-6):1–152, 2005. doi: https://doi.org/10.1016/j.surfrep.2005.08.003.

[28] Stephen Butterworth. Experimental wireless and the wireless engineer. *Wireless Eng*, 7:536, 1930. URL https://www.changpuak.ch/electronics/downloads/On_the_Theory_of_Filter_Amplifiers.pdf.

[29] Y. Cai, W.-P. Peng, and H.-C. Chang. Ion trap mass spectrometry of fluorescently labeled nanoparticles. *Analytical Chemistry*, 75(8):1805–1811, 2003. doi: 10.1021/ac0206723. URL https://doi.org/10.1021/ac0206723. PMID: 12713037.

[30] Matthew Cole, Pennie Lindeque, Elaine Fileman, Claudia Halsband, Rhys Goodhead, Julian Moger, and Tamara S. Galloway. Microplastic ingestion by zooplankton. *Environmental Science & Technology*, 47 (12):6646–6655, 2013. doi: 10.1021/es400663f. URL https://doi.org/10.1021/es400663f. PMID: 23692270.

[31] Manuel Correia and Katrin Loeschner. Detection of nanoplastics in food by asymmetric flow field-flow fractionation coupled to multi-angle light scattering: possibilities, challenges and analytical limitations. *Analytical and bioanalytical chemistry*, 410(22):5603–5615, 2018. doi: https://doi.org/10.1007/s00216-018-0919-8.

[32] Andrés Cózar, Fidel Echevarría, J. Ignacio González-Gordillo, Xabier Irigoien, Bárbara Úbeda, Santiago Hernández-León, Álvaro T. Palma, Sandra Navarro, Juan García-de Lomas, Andrea Ruiz, María L. Fernández-de Puelles, and Carlos M. Duarte. Plastic debris in the open ocean. *Proceedings of the National Academy of Sciences*, 111(28):10239–10244, 2014. ISSN 0027-8424. doi: 10.1073/pnas.1314705111. URL https://www.pnas.org/content/111/28/10239.

[33] Christopher Blair Crawford and Brian Quinn. 10 - microplastic identification techniques. In Christopher Blair Crawford and Brian Quinn, editors, *Microplastic Pollutants*, pages 219 – 267. Elsevier, 2017. ISBN 978-0-12-809406-8. doi: https://doi.org/10.1016/B978-0-12-809406-8.00010-4. URL http://www.sciencedirect.com/science/article/pii/B9780128094068000104.

[34] Savio D Souza. Resonant modes of hollow micro-cantilevers for characterization of liquids in picolitre volumes. *Delft University of Technology*, master thesis, 2018. URL http://resolver.tudelft.nl/uuid:0a054205-1d99-4079-ae5b-b48858a354a6.

[35] A Dazzi, J Saunier, K Kjoller, and N Yagoubi. Resonance enhanced afm-ir: A new powerful way to characterize blooming on polymers used in medical devices. *International journal of pharmaceutics*, 484(1-2):109–114, 2015. doi: https://doi.org/10.1016/j.ijpharm.2015.02.046.

[36] Alexandre Dazzi, Craig B. Prater, Qichi Hu, D. Bruce Chase, John F. Rabolt, and Curtis Marcott. Afm–ir: Combining atomic force microscopy and infrared spectroscopy for nanoscale chemical characterization. *Applied Spectroscopy*, 66(12):1365–1384, 2012. doi: 10.1366/12-06804. URL https://doi.org/10.1366/12-06804. PMID: 23231899.

[37] Marcelo de Assumpção Pereira-da Silva and Fabio A. Ferri. 1 - scanning electron microscopy. In Alessandra L. Da Róz, Marystela Ferreira, Fabio de Lima Leite, and Osvaldo N. Oliveira, editors, *Nanocharacterization Techniques*, Micro and Nano Technologies, pages 1 – 35. William Andrew Publishing, 2017. ISBN 978-0-323-49778-7. doi: https://doi.org/10.1016/B978-0-323-49778-7.00001-1. URL http://www.sciencedirect.com/science/article/pii/B9780323497787000011.

[38] Ray F Egerton et al. *Physical principles of electron microscopy*. Springer, 2005. ISBN 9783319398778. doi: https://doi.org/10.1007/978-3-319-39877-8.

[39] K. L. Ekinci, Y. T. Yang, and M. L. Roukes. Ultimate limits to inertial mass sensing based upon nanoelectromechanical systems. *Journal of Applied Physics*, 95(5):2682–2689, 2004. doi: 10.1063/1.1642738. URL https://doi.org/10.1063/1.1642738.

[40] Douglas F Elliott. *Handbook of digital signal processing: engineering applications*. Elsevier, 2013.

[41] Plastic Europe. Plastics—the facts 2019. *An Analysis of European Latest Plastics Production, Demand and Waste Data*, 2019. URL https://www.plasticseurope.org/application/files/9715/7129/9584/FINAL_web_version_Plastics_the_facts2019_14102019.pdf.

[42] E. S. Ferre-Pikal, J. R. Vig, J. C. Camparo, L. S. Cutler, L. Maleki, W. J. Riley, S. R. Stein, C. Thomas, F. L. Walls, and J. D. White. Draft revision of ieee std 1139-1988 standard definitions of physical quantities for fundamental, frequency and time metrology-random instabilities. In *Proceedings of International Frequency Control Symposium*, pages 338–357, May 1997. doi: 10.1109/FREQ.1997.638567.

[43] Gernot Friedbacher, Manfred Grasserbauer, Yousef Meslmani, Norbert Klaus, and Michael J Higatsberger. Investigation of environmental aerosol by atomic force microscopy. *Analytical Chemistry*, 67 (10):1749–1754, 1995.

[44] Ricardo Garcıa and Ruben Perez. Dynamic atomic force microscopy methods. *Surface science reports*, 47(6-8):197–301, 2002. doi: https://doi.org/10.1016/S0167-5729(02)00077-8.

[45] Roland Geyer, Jenna R. Jambeck, and Kara Lavender Law. Production, use, and fate of all plastics ever made. *Science Advances*, 3(7), 2017. doi: 10.1126/sciadv.1700782. URL https://advances.sciencemag.org/content/3/7/e1700782.

[46] Franz Josef Giessibl. Atomic force microscopy in ultrahigh vacuum. *Japanese Journal of Applied Physics*, 33(Part 1, No. 6B):3726–3734, jun 1994. doi: 10.1143/jjap.33.3726. URL https://doi.org/10.1143%2Fjjap.33.3726.

[47] Julien Gigault, Alexandra ter Halle, Magalie Baudrimont, Pierre-Yves Pascal, Fabienne Gauffre, Thuy-Linh Phi, Hind El Hadri, Bruno Grassl, and Stéphanie Reynaud. Current opinion: What is a nanoplastic? *Environmental Pollution*, 235:1030 – 1034, 2018. ISSN 0269-7491. doi: https://doi.org/10.1016/j.envpol.2018.01.024. URL http://www.sciencedirect.com/science/article/pii/S0269749117337247.

[48] I V Gmoshinski, S A Khotimchenko, V O Popov, B B Dzantiev, A V Zherdev, V F Demin, and Yu P Buzulukov. Nanomaterials and nanotechnologies: methods of analysis and control. *Russian Chemical Reviews*, 82(1):48–76, jan 2013. doi: 10.1070/rc2013v082n01abeh004329. URL https://doi.org/10.1070%2Frc2013v082n01abeh004329.

[49] Michel Godin, Francisco Feijó Delgado, Sungmin Son, William H Grover, Andrea K Bryan, Amit Tzur, Paul Jorgensen, Kris Payer, Alan D Grossman, Marc W Kirschner, and Scott R Manalis. Using buoyant mass to measure the growth of single cells. *Nature Methods*, 7:387—-390, 2010. doi: 10.1038/nmeth.1452. URL https://doi.org/10.1038/nmeth.1452.

[50] Wolfgang Haiss, Nguyen T. K. Thanh, Jenny Aveyard, and David G. Fernig. Determination of size and concentration of gold nanoparticles from uvvis spectra. *Analytical Chemistry*, 79(11):4215–4221, 2007. doi: 10.1021/ac0702084. URL https://doi.org/10.1021/ac0702084. PMID: 17458937.

[51] Bahrudeen S. Hameed, Chandra S. Bhatt, Bharathkumar Nagaraj, and Anil K. Suresh. Chapter 19 - chromatography as an efficient technique for the separation of diversified nanoparticles. In Chaudhery Mustansar Hussain, editor, *Nanomaterials in Chromatography*, pages 503 – 518. Elsevier, 2018. ISBN 978-0-12-812792-6. doi: https://doi.org/10.1016/B978-0-12-812792-6.00019-4. URL http://www.sciencedirect.com/science/article/pii/B9780128127926000194.

[52] Sven Henning and Rameshwar Adhikari. Chapter 1 - scanning electron microscopy, esem, and x-ray microanalysis. In Sabu Thomas, Raju Thomas, Ajesh K. Zachariah, and Raghvendra Kumar Mishra, editors, *Microscopy Methods in Nanomaterials Characterization*, Micro and Nano Technologies, pages 1 – 30. Elsevier, 2017. ISBN 978-0-323-46141-2. doi: https://doi.org/10.1016/B978-0-323-46141-2.00001-8. URL http://www.sciencedirect.com/science/article/pii/B9780323461412000018.

[53] Ludovic Hermabessiere, Charlotte Himber, Béatrice Boricaud, Maria Kazour, Rachid Amara, Anne-Laure Cassone, Michel Laurentie, Ika Paul-Pont, Philippe Soudant, Alexandre Dehaut, et al. Optimization, performance, and application of a pyrolysis-gc/ms method for the identification of microplastics. *Analytical and bioanalytical chemistry*, 410(25):6663–6676, 2018. doi: https://doi.org/10.1007/s00216-018-1279-0.

[54] Laura M. Hernandez, Nariman Yousefi, and Nathalie Tufenkji. Are there nanoplastics in your personal care products? *Environmental Science & Technology Letters*, 4(7):280–285, 2017. doi: 10.1021/acs.estlett.7b00187. URL https://doi.org/10.1021/acs.estlett.7b00187.

[55] Valeria Hidalgo-Ruz, Lars Gutow, Richard C. Thompson, and Martin Thiel. Microplastics in the marine environment: A review of the methods used for identification and quantification. *Environmental Science & Technology*, 46(6):3060–3075, 2012. doi: 10.1021/es2031505. URL https://doi.org/10.1021/es2031505. PMID: 22321064.

[56] Dr. Ian Hunt. *Simple schematic of an electron impact mass spectrometer*, 2019. URL http://www.chem.ucalgary.ca/courses/350/Carey5th/Ch13/ch13-ms.html.

[57] B. Ilic, H. G. Craighead, S. Krylov, W. Senaratne, C. Ober, and P. Neuzil. Attogram detection using nanoelectromechanical oscillators. *Journal of Applied Physics*, 95(7):3694–3703, 2004. doi: 10.1063/1.1650542. URL https://doi.org/10.1063/1.1650542.

[58] Thermo Fisher Scientific Inc. The frontier of routine gc-ms. *PS10506-EN 0218M*, 2018. URL https://assets.thermofisher.com/TFS-Assets/CMD/Specification-Sheets/PS-10506-Exactive-GC-Orbitrap-GC-MS-PS10506-EN.pdf.

[59] RN Jagtap and AH Ambre. Overview literature on atomic force microscopy (afm): Basics and its important applications for polymer characterization. *Indian Journal of Engineering and Materials Sciences (IJEMS)*, 2006. ISSN 0975-1017. URL http://nopr.niscair.res.in/handle/123456789/7570.

[60] JEOL Ltd. *JEM-ARM300F Grand ARM Transmission Electron Microscope*, 2019. URL https://www.jeolusa.com/PRODUCTS/Transmission-Electron-Microscopes-TEM/300-kV/JEM-ARM300F.

[61] JEOL USA, Inc. *Mass Spectrometers - A Short Explanation for the Absolute Novice*, 2006. URL https://www.jeolusa.com/RESOURCES/Analytical-Instruments/Documents-Downloads?EntryId=285&Command=Core_Download.

[62] JEOL USA, Inc. *JSM-IT500HR InTouchScope™ SEM*, 2019. URL https://www.jeolusa.com/PRODUCTS/Scanning-Electron-Microscopes-SEM/High-Res-Large-Chamber-SEM/JSM-IT500HR.

[63] Blake N. Johnson and Raj Mutharasan. Biosensing using dynamic-mode cantilever sensors: A review. *Biosensors and Bioelectronics*, 32(1):1 – 18, 2012. ISSN 0956-5663. doi: https://doi.org/10.1016/j.bios.2011.10.054. URL http://www.sciencedirect.com/science/article/pii/S0956566311007421.

[64] Hanna L. Karlsson, Johanna Gustafsson, Pontus Cronholm, and Lennart Möller. Size-dependent toxicity of metal oxide particles—a comparison between nano- and micrometer size. *Toxicology Letters*, 188(2):112 – 118, 2009. ISSN 0378-4274. doi: https://doi.org/10.1016/j.toxlet.2009.03.014. URL http://www.sciencedirect.com/science/article/pii/S0378427409001611.

[65] Mike Kaszuba and Craig Sagar. *A basic introduction to Dynamic Light Scattering (DLS) for particle size analysis[Webinar]*, 2017. URL https://www.malvernpanalytical.com/en/learn/events-and-training/webinars/W180201BasicDynamicLightScattering.html.

[66] M.F. Khan, S. Schmid, P.E. Larsen, Z.J. Davis, W. Yan, E.H. Stenby, and A. Boisen. Online measurement of mass density and viscosity of pl fluid samples with suspended microchannel resonator. *Sensors and Actuators B: Chemical*, 185:456 – 461, 2013. ISSN 0925-4005. doi: https://doi.org/10.1016/j.snb.2013.04.095. URL http://www.sciencedirect.com/science/article/pii/S0925400513005285.

[67] Sascha Klein, Ian K Dimzon, Jan Eubeler, and Thomas P Knepper. Analysis, occurrence, and degradation of microplastics in the aqueous environment. In *Freshwater Microplastics*, pages 51–67. Springer, Cham, 2018. doi: https://doi.org/10.1007/978-3-319-61615-5_3.

[68] Francisco Laborda, Eduardo Bolea, Gemma Cepriá, María T. Gómez, María S. Jiménez, Josefina Pérez-Arantegui, and Juan R. Castillo. Detection, characterization and quantification of inorganic engineered nanomaterials: A review of techniques and methodological approaches for the analysis of complex samples. *Analytica Chimica Acta*, 904:10 – 32, 2016. ISSN 0003-2670. doi: https://doi.org/10.1016/j.aca.2015.11.008. URL http://www.sciencedirect.com/science/article/pii/S0003267015013677.

[69] J. R. Lead, D. Muirhead, and C. T. Gibson. Characterization of freshwater natural aquatic colloids by atomic force microscopy (afm). *Environmental Science & Technology*, 39(18):6930–6936, 2005. doi: 10.1021/es050386j. URL https://doi.org/10.1021/es050386j. PMID: 16201613.

[70] Bong Jae Lee and Jungchul Lee. Beyond mass measurement for single microparticles via bimodal operation of microchannel resonators. *Micro and Nano Systems Letters*, 7(1):1–6, 2019. URL https://doi.org/10.1186/s40486-019-0088-3.

[71] Jungchul Lee, Wenjiang Shen, Kris Payer, Thomas P. Burg, and Scott R. Manalis. Toward attogram mass measurements in solution with suspended nanochannel resonators. *Nano Letters*, 10(7):2537–2542, 2010. doi: 10.1021/nl101107u. URL https://doi.org/10.1021/nl101107u. PMID: 20527897.

[72] Roman Lehner, Christoph Weder, Alke Petri-Fink, and Barbara Rothen-Rutishauser. Emergence of nanoplastic in the environment and possible impact on human health. *Environmental Science & Technology*, 53(4):1748–1765, 2019. doi: 10.1021/acs.est.8b05512. URL https://doi.org/10.1021/acs.est.8b05512. PMID: 30629421.

[73] Jiana Li, Xiaoyun Qu, Lei Su, Weiwei Zhang, Dongqi Yang, Prabhu Kolandhasamy, Daoji Li, and Huahong Shi. Microplastics in mussels along the coastal waters of china. *Environmental Pollution*, 214:177 – 184, 2016. ISSN 0269-7491. doi: https://doi.org/10.1016/j.envpol.2016.04.012. URL http://www.sciencedirect.com/science/article/pii/S0269749116302767.

[74] Ping-Chang Lin, Stephen Lin, Paul C. Wang, and Rajagopalan Sridhar. Techniques for physicochemical characterization of nanomaterials. *Biotechnology Advances*, 32(4):711 – 726, 2014. ISSN 0734-9750. doi: https://doi.org/10.1016/j.biotechadv.2013.11.006. URL http://www.sciencedirect.com/science/article/pii/S0734975013002115. Biotechnology in Nanomedicine.

[75] Martin GJ Löder and Gunnar Gerdts. Methodology used for the detection and identification of microplastics a critical appraisal. In *Marine anthropogenic litter*, pages 201–227. Springer, 2015. ISBN 978-3-319-16509-7. doi: https://doi.org/10.1007/978-3-319-16510-3_8.

[76] Malvern Panalytical Ltd. *ARCHIMEDES MASS MEASUREMENT ON A DIFFERENT SCALE*, 2019. URL https://www.malvernpanalytical.com/en/assets/MRK1869-02_tcm50-17231.pdf.

[77] Instruments Ltd. Malvern. Dynamic light scattering: an introduction in 30 minutes. *Technical Note Malvern, MRK656-01*, 1, 2014. URL https://www.semanticscholar.org/paper/Dynamic-Light-Scattering-%3A-An-Introduction-in-30/1d28101f3c0b2c4bbcb305f930fdc658f800fac5?citationIntent=result#citing-papers.

[78] Marica Marrese, Vincenzo Guarino, and Luigi Ambrosio. Atomic force microscopy: A powerful tool to address scaffold design in tissue engineering. *Journal of Functional Biomaterials*, 8(1), 2017. ISSN 2079-4983. doi: 10.3390/jfb8010007. URL https://www.mdpi.com/2079-4983/8/1/7.

[79] Jan Mast, Eveline Verleysen, Vasile-Dan Hodoroaba, and Ralf Kaegi. Chapter 2.1.2 - characterization of nanomaterials by transmission electron microscopy: Measurement procedures. In Vasile-Dan Hodoroaba, Wolfgang E.S. Unger, and Alexander G. Shard, editors, *Characterization of Nanoparticles*, Micro and Nano Technologies, pages 29 – 48. Elsevier, 2020. ISBN 978-0-12-814182-3. doi: https://doi.org/10.1016/B978-0-12-814182-3.00004-3. URL http://www.sciencedirect.com/science/article/pii/B9780128141823000043.

[80] K. Mattsson, L.-A. Hansson, and T. Cedervall. Nano-plastics in the aquatic environment. *Environ. Sci.: Processes Impacts*, 17:1712–1721, 2015. doi: 10.1039/C5EM00227C. URL http://dx.doi.org/10.1039/C5EM00227C.

[81] Karin Mattsson, Simonne Jocic, Isa Doverbratt, and Lars-Anders Hansson. Chapter 13 - nanoplastics in the aquatic environment. In Eddy Y. Zeng, editor, *Microplastic Contamination in Aquatic Environments*, pages 379 – 399. Elsevier, 2018. ISBN 978-0-12-813747-5. doi: https://doi.org/10.1016/B978-0-12-813747-5.00013-8. URL http://www.sciencedirect.com/science/article/pii/B9780128137475000138.

[82] James M. Lehto Miller, Azadeh Ansari, David B. Heinz, Yunhan Chen, Ian B. Flader, Dongsuk D. Shin, L. Guillermo Villanueva, and Thomas W. Kenny. Effective quality factor tuning mechanisms in micromechanical resonators. *Applied Physics Reviews*, 5(4):041307, 2018. doi: 10.1063/1.5027850. URL https://doi.org/10.1063/1.5027850.

[83] Svenja Maria Mintenig, Patrick S Bäuerlein, Albert A Koelmans, Stefan C Dekker, and AP Van Wezel. Closing the gap between small and smaller: towards a framework to analyse nano-and microplastics in aqueous environmental samples. *Environmental Science: Nano*, 5(7):1640–1649, 2018. doi: 10.1039/C8EN00186C.

[84] Marco P Monopoli, Christoffer Åberg, Anna Salvati, and Kenneth A Dawson. Biomolecular coronas provide the biological identity of nanosized materials. *Nature nanotechnology*, 7(12):779, 2012. doi: https://doi.org/10.1038/nnano.2012.207.

[85] Fernando Moreno-Herrero and Julio Gomez-Herrero. Afm: Basic concepts. In Arturo M. Bar´o and Ronald G. Reifenberger, editors, *Atomic force microscopy in liquid: biological applications*, pages 3–34. John Wiley & Sons, 2012. ISBN 9783527327584.

[86] Stefanos Mourdikoudis, Roger M Pallares, and Nguyen TK Thanh. Characterization techniques for nanoparticles: Comparison and complementarity upon studying nanoparticle properties. *Nanoscale*, 10(27):12871–12934, 2018. doi: https://doi.org/10.1039/C8NR02278J.

[87] Richard C. Murdock, Laura Braydich-Stolle, Amanda M. Schrand, John J. Schlager, and Saber M. Hussain. Characterization of Nanomaterial Dispersion in Solution Prior to In Vitro Exposure Using Dynamic Light Scattering Technique. *Toxicological Sciences*, 101(2):239–253, 09 2007. ISSN 1096-6080. doi: 10.1093/toxsci/kfm240. URL https://doi.org/10.1093/toxsci/kfm240.

[88] M. Reza Nejadnik and Wim Jiskoot. Measurement of the average mass of proteins adsorbed to a nanoparticle by using a suspended microchannel resonator. *Journal of Pharmaceutical Sciences*, 104 (2):698 – 704, 2015. ISSN 0022-3549. doi: https://doi.org/10.1002/jps.24206. URL http://www.sciencedirect.com/science/article/pii/S0022354915302094.

[89] Diogo Neves, Paula Sobral, Joana Lia Ferreira, and Tânia Pereira. Ingestion of microplastics by commercial fish off the portuguese coast. *Marine Pollution Bulletin*, 101(1):119 – 126, 2015. ISSN 0025-326X. doi: https://doi.org/10.1016/j.marpolbul.2015.11.008. URL http://www.sciencedirect.com/science/article/pii/S0025326X15301582.

[90] Brian Nguyen, Dominique Claveau-Mallet, Laura M. Hernandez, Elvis Genbo Xu, Jeffrey M. Farner, and Nathalie Tufenkji. Separation and analysis of microplastics and nanoplastics in complex environmental samples. *Accounts of Chemical Research*, 52(4):858–866, 2019. doi: 10.1021/acs.accounts.8b00602. URL https://doi.org/10.1021/acs.accounts.8b00602.

[91] Takashi Nohmi and John B. Fenn. Electrospray mass spectrometry of poly(ethylene glycols) with molecular weights up to five million. *Journal of the American Chemical Society*, 114(9):3241–3246, 1992. doi: 10.1021/ja00035a012. URL https://doi.org/10.1021/ja00035a012.

[92] S. Olcum, N. Cermak, and S. R. Manalis. Precision mass measurements in solution reveal properties of single cells and bioparticles. In *2015 IEEE International Electron Devices Meeting (IEDM)*, pages 13.5.1–13.5.4, Dec 2015. doi: 10.1109/IEDM.2015.7409691.

[93] Selim Olcum, Nathan Cermak, Steven C. Wasserman, Kathleen S. Christine, Hiroshi Atsumi, Kris R. Payer, Wenjiang Shen, Jungchul Lee, Angela M. Belcher, Sangeeta N. Bhatia, and Scott R. Manalis. Weighing nanoparticles in solution at the attogram scale. *Proceedings of the National Academy of Sciences*, 111(4):1310–1315, 2014. ISSN 0027-8424. doi: 10.1073/pnas.1318602111. URL https://www.pnas.org/content/111/4/1310.

[94] Selim Olcum, Nathan Cermak, Steven C Wasserman, and Scott R Manalis. High-speed multiple-mode mass-sensing resolves dynamic nanoscale mass distributions. *Nature communications*, 6(1):1–8, 2015. doi: https://doi.org/10.1038/ncomms8070.

[95] Olena Oriekhova and Serge Stoll. Heteroaggregation of nanoplastic particles in the presence of inorganic colloids and natural organic matter. *Environ. Sci.: Nano*, 5:792–799, 2018. doi: 10.1039/C7EN01119A. URL http://dx.doi.org/10.1039/C7EN01119A.

[96] AE Owen. *Fundamentals of UV-visible spectroscopy: a primer*. Hewlett Packard, 1996.

[97] Park Systems. *Park NX10 The most accurate and easiest to use Atomic Force Microscope*, 2019. URL https://www.parksystems.com/images/media/brochures/nx10/park_NX10180904E16AB.pdf.

[98] W.-P. Peng, Y. Cai, Y.T. Lee, and H.-C. Chang. Laser-induced fluorescence/ion trap as a detector for mass spectrometric analysis of nanoparticles. *International Journal of Mass Spectrometry*, 229(1):67 – 76, 2003. ISSN 1387-3806. doi: https://doi.org/10.1016/S1387-3806(03)00257-4. URL http://www.sciencedirect.com/science/article/pii/S1387380603002574. Mass Spectrometry Contributions to Nanosciences and Nanotechnology.

[99] Peter M. van Galen and Martin C. Feiters. *Mass Spectrometry part of the Instrumental Analysis in (Bio)Molecular Chemistry Course*, 2016. URL https://www.ru.nl/publish/pages/580561/ms_lecture_notes_161003_mcf.pdf.

[100] Rosa Peñalver, Natalia Arroyo-Manzanares, Ignacio López-García, and Manuel Hernández-Córdoba. An overview of microplastics characterization by thermal analysis. *Chemosphere*, 242:125170, 2020. ISSN 0045-6535. doi: https://doi.org/10.1016/j.chemosphere.2019.125170. URL http://www.sciencedirect.com/science/article/pii/S0045653519324099.

[101] PG Instruments. *FTIR 7800 Fourier Transform Infrared Spectrometer*, 2019. URL https://www.pginstruments.com/product/ftir-7800/.

[102] Stepan Podzimek. *Light scattering, size exclusion chromatography and asymmetric flow field flow fractionation: powerful tools for the characterization of polymers, proteins and nanoparticles*. John Wiley & Sons, 2011. ISBN 978-0-470-38617-0.

[103] Jonathan J Powell, Vinay Thoree, and Laetitia C Pele. Dietary microparticles and their impact on tolerance and immune responsiveness of the gastrointestinal tract. *British Journal of Nutrition*, 98(S1): S59–S63, 2007. doi: 10.1017/S0007114507832922.

[104] Ana P.Ramos. Dynamic light scattering applied to nanoparticle characterization. *Nanocharacterization Techniques*, pages 99–110, 2017. doi: 10.1016/b978-0-323-49778-7.00004-7.

[105] J. Qin, K. Chao, and M.S. Kim. Chapter 6 - introduction to raman chemical imaging technology. In Da-Wen Sun, editor, *Computer Vision Technology for Food Quality Evaluation (Second Edition)*, pages 141 – 171. Academic Press, San Diego, second edition edition, 2016. ISBN 978-0-12-802232-0. doi: https://doi.org/10.1016/B978-0-12-802232-0.00006-2. URL http://www.sciencedirect.com/science/article/pii/B9780128022320000062.

[106] Gerrit Renner, Torsten C. Schmidt, and Jürgen Schram. Analytical methodologies for monitoring micro(nano)plastics: Which are fit for purpose? *Current Opinion in Environmental Science & Health*, 1:55 – 61, 2018. ISSN 2468-5844. doi: https://doi.org/10.1016/j.coesh.2017.11.001. URL http://www.sciencedirect.com/science/article/pii/S2468584417300260. Micro and Nanoplastics Edited by Dr. Teresa A.P. Rocha-Santos.

[107] Messika Revel, Amélie Châtel, and Catherine Mouneyrac. Micro(nano)plastics: A threat to human health? *Current Opinion in Environmental Science & Health*, 1:17 – 23, 2018. ISSN 2468-5844. doi: https://doi.org/10.1016/j.coesh.2017.10.003. URL http://www.sciencedirect.com/science/article/pii/S2468584417300235. Micro and Nanoplastics Edited by Dr. Teresa A.P. Rocha-Santos.

[108] William J Riley. Handbook of frequency stability analysis. 2008.

[109] Dror Sarid. *Scanning force microscopy: with applications to electric, magnetic, and atomic forces*, volume 5. Oxford University Press, 1994. ISBN 9780195062700.

[110] Jens Schaefer, Christine Schulze, Elena Eva Julianne Marxer, Ulrich Friedrich Schaefer, Wendel Wohlleben, Udo Bakowsky, and Claus-Michael Lehr. Atomic force microscopy and analytical ultracentrifugation for probing nanomaterial protein interactions. *ACS Nano*, 6(6):4603–4614, 2012. doi: 10.1021/nn202657q. URL https://doi.org/10.1021/nn202657q. PMID: 22577818.

[111] Silvan Schmid, Luis Guillermo Villanueva, and Michael Lee Roukes. *Fundamentals of nanomechanical resonators*, volume 49. Springer, 2016. ISBN 978-3-319-28691-4. doi: 10.1007/978-3-319-28691-4.

[112] R Munnig Schmidt, Georg Schitter, and Adrian Rankers. *The Design of High Performance Mechatronics - 2nd Revised Edition*. Ios Press, 2014. ISBN 9781614993674.

[113] Christian Schwaferts, Reinhard Niessner, Martin Elsner, and Natalia P. Ivleva. Methods for the analysis of submicrometer- and nanoplastic particles in the environment. *TrAC Trends in Analytical Chemistry*, 112:52 – 65, 2019. ISSN 0165-9936. doi: https://doi.org/10.1016/j.trac.2018.12.014. URL http://www.sciencedirect.com/science/article/pii/S0165993618304631.

[114] Alexander G. Shard, Robert C. Schofield, and Caterina Minelli. Chapter 3.2.3 - ultraviolet - visible spectrophotometry. In Vasile-Dan Hodoroaba, Wolfgang E.S. Unger, and Alexander G. Shard, editors, *Characterization of Nanoparticles*, Micro and Nano Technologies, pages 185 – 196. Elsevier, 2020. ISBN 978-0-12-814182-3. doi: https://doi.org/10.1016/B978-0-12-814182-3.00012-2. URL http://www.sciencedirect.com/science/article/pii/B9780128141823000122.

[115] Won Joon Shim, Sang Hee Hong, and Soeun Eo Eo. Identification methods in microplastic analysis: a review. *Analytical methods*, 9(9):1384–1391, 2017. doi: https://doi.org/10.1039/C6AY02558G.

[116] Douglas A. Skoog, F. James Holler, and Stanley R. Crouch. chapterseven components of optical instruments. In *Principles of Instrumental Analysis (Seventh Edition)*, pages 148 – 195. Cengage Learning, Boston, MA, seventh edition edition, 2018. ISBN 978-1-305-57721-3.

[117] Douglas A. Skoog, F. James Holler, and Stanley R. Crouch. chaptereighteen raman spectroscopy. In *Principles of Instrumental Analysis (Seventh Edition)*, pages 437 – 452. Cengage Learning, Boston, MA, seventh edition edition, 2018. ISBN 978-1-305-57721-3.

[118] Douglas A. Skoog, F. James Holler, and Stanley R. Crouch. chapterthirteen an introduction to ultraviolet-visible molecular absorption spectrometry. In *Principles of Instrumental Analysis (Seventh Edition)*, pages 304 – 330. Cengage Learning, Boston, MA, seventh edition edition, 2018. ISBN 978-1-305-57721-3.

[119] Douglas A. Skoog, F. James Holler, and Stanleyk R. Crouch. chaptersixteen an introduction to infrared spectrometry. In *Principles of Instrumental Analysis (Seventh Edition)*, pages 389 – 411. Cengage Learning, Boston, MA, seventh edition edition, 2018. ISBN 978-1-305-57721-3.

[120] Ki Chang Song, Sung Min Lee, Tae Sun Park, and Bum Suk Lee. Preparation of colloidal silver nanoparticles by chemical reduction method. *Korean Journal of Chemical Engineering*, 26(1):153–155, 2009. doi: 10.1007/s11814-009-0024-y. URL https://doi.org/10.1007/s11814-009-0024-y.

[121] Debbie Stokes. *Principles and practice of variable pressure/environmental scanning electron microscopy (VP-ESEM)*. John Wiley & Sons, Incorporated, 2008. ISBN 9780470758748.

[122] Debbie Stokes. *Principles and practice of variable pressure/environmental scanning electron microscopy (VP-ESEM)*. John Wiley & Sons, 2008. ISBN 9780470758748.

[123] Stefan-Adrian Strungaru, Roxana Jijie, Mircea Nicoara, Gabriel Plavan, and Caterina Faggio. Micro-(nano) plastics in freshwater ecosystems: Abundance, toxicological impact and quantification methodology. *TrAC Trends in Analytical Chemistry*, 110:116 – 128, 2019. ISSN 0165-9936. doi: https://doi.org/10.1016/j.trac.2018.10.025. URL http://www.sciencedirect.com/science/article/pii/S0165993618304254.

[124] C.Y. Tang and Z. Yang. Chapter 8 - transmission electron microscopy (tem). In Nidal Hilal, Ahmad Fauzi Ismail, Takeshi Matsuura, and Darren Oatley-Radcliffe, editors, *Membrane Characterization*, pages 145 – 159. Elsevier, 2017. ISBN 978-0-444-63776-5. doi: https://doi.org/10.1016/B978-0-444-63776-5.00008-5. URL http://www.sciencedirect.com/science/article/pii/B9780444637765000085.

[125] Ronald Tararam, Pâmela S. Garcia, Daiana K. Deda, José A. Varela, and Fábio de Lima Leite. 2 - atomic force microscopy: A powerful tool for electrical characterization. In Alessandra L. Da Róz, Marystela Ferreira, Fabio de Lima Leite, and Osvaldo N. Oliveira, editors, *Nanocharacterization Techniques*, Micro and Nano Technologies, pages 37 – 64. William Andrew Publishing, 2017. ISBN 978-0-323-49778-7. doi: https://doi.org/10.1016/B978-0-323-49778-7.00002-3. URL http://www.sciencedirect.com/science/article/pii/B9780323497787000023.

[126] Stefan Tenzer, Dominic Docter, Jörg Kuharev, Anna Musyanovych, Verena Fetz, Rouven Hecht, Florian Schlenk, Dagmar Fischer, Klytaimnistra Kiouptsi, Christoph Reinhardt, et al. Rapid formation of plasma protein corona critically affects nanoparticle pathophysiology. *Nature nanotechnology*, 8(10): 772, 2013. doi: https://doi.org/10.1038/nnano.2013.181.

[127] Alexandra Ter Halle, Laurent Jeanneau, Marion Martignac, Emilie Jardé, Boris Pedrono, Laurent Brach, and Julien Gigault. Nanoplastic in the north atlantic subtropical gyre. *Environmental Science & Technology*, 51(23):13689–13697, 2017. doi: 10.1021/acs.est.7b03667. URL https://doi.org/10.1021/acs.est.7b03667. PMID: 29161030.

[128] Emma L. Teuten, Steven J. Rowland, Tamara S. Galloway, and Richard C. Thompson. Potential for plastics to transport hydrophobic contaminants. *Environmental Science & Technology*, 41(22):7759–7764, 2007. doi: 10.1021/es071737s. URL https://doi.org/10.1021/es071737s. PMID: 18075085.

[129] Thermo Electron Corporation. *Introduction to Fourier Transform Infrared Spectroscopy*, 2005. URL http://www.nicoletcz.cz/upload/kc/files/aplikacni-podpora/teorie/IntroductionToFTIR.pdf.

[130] Thermo Scientific. *DXR3 Raman Microscope*, 2019. URL https://www.thermofisher.com/order/catalog/product/IQLAADGABFFAHCMAPB?SID=srch-srp-IQLAADGABFFAHCMAPB.

[131] Richard C. Thompson, Ylva Olsen, Richard P. Mitchell, Anthony Davis, Steven J. Rowland, Anthony W. G. John, Daniel McGonigle, and Andrea E. Russell. Lost at sea: Where is all the plastic? *Science*, 304(5672): 838–838, 2004. ISSN 0036-8075. doi: 10.1126/science.1094559. URL https://science.sciencemag.org/content/304/5672/838.

[132] T. Thundat, E. A. Wachter, S. L. Sharp, and R. J. Warmack. Detection of mercury vapor using resonating microcantilevers. *Applied Physics Letters*, 66(13):1695–1697, 1995. doi: 10.1063/1.113896. URL https://doi.org/10.1063/1.113896.

[133] Karen Tiede, Alistair B.A. Boxall, Steven P. Tear, John Lewis, Helen David, and Martin Hassellöv. Detection and characterization of engineered nanoparticles in food and the environment. *Food Additives & Contaminants: Part A*, 25(7):795–821, 2008. doi: 10.1080/02652030802007553. URL https://doi.org/10.1080/02652030802007553.

[134] Emilia Tomaszewska, Katarzyna Soliwoda, Kinga Kadziola, Beata, Tkacz-Szczesna, Grzegorz Celichowski, Michal Cichomski, Witold Szmaja, and Jaroslaw Grobelny. Detection limits of dls and uv-vis spectroscopy in characterization of polydisperse nanoparticles colloids. *Journal of Nanomaterials, 2013*, pages 1–10, 2013. doi: 10.1155/2013/313081.

[135] Shin Tsuge and Hajime Ohtani. Chapter 25 pyrolysis-gas chromatography. In *Practical Gas Chromatography*, pages 830–847. Springer, 2014. ISBN 978-3-642-54640-2. doi: https://doi.org/10.1007/978-3-642-54640-2.

[136] Thomas Walther. Chapter 4 - transmission electron microscopy of nanostructures. In Sabu Thomas, Raju Thomas, Ajesh K. Zachariah, and Raghvendra Kumar Mishra, editors, *Microscopy Methods in Nanomaterials Characterization*, Micro and Nano Technologies, pages 105 – 134. Elsevier, 2017. ISBN 978-0-323-46141-2. doi: https://doi.org/10.1016/B978-0-323-46141-2.00004-3. URL http://www.sciencedirect.com/science/article/pii/B9780323461412000043.

[137] Zhan Wang, Stephen E. Taylor, Prabhakar Sharma, and Markus Flury. Poor extraction efficiencies of polystyrene nano- and microplastics from biosolids and soil. *PLOS ONE*, 13(11):1–13, 11 2018. doi: 10.1371/journal.pone.0208009. URL https://doi.org/10.1371/journal.pone.0208009.

[138] J Throck Watson and O David Sparkman. *Introduction to mass spectrometry: instrumentation, applications, and strategies for data interpretation*. John Wiley & Sons, 2007. ISBN 9780470516348 0470516348.

[139] Wikipedia. Colors of noise, . URL https://en.wikipedia.org/wiki/Colors_of_noise.

[140] Wikipedia. *Butterworth filter*, . URL https://en.wikipedia.org/wiki/Butterworth_filter.

[141] Philip J. Wyatt. Submicrometer particle sizing by multiangle light scattering following fractionation. *Journal of Colloid and Interface Science*, 197(1):9 – 20, 1998. ISSN 0021-9797. doi: https://doi.org/10.1006/jcis.1997.5215. URL http://www.sciencedirect.com/science/article/pii/S0021979797952152.

[142] Wyatt Technology. *DAWN scattering light detector for SEC-MALS*, 2019. URL https://www.wyatt.com/products/instruments/dawn-multi-angle-light-scattering-detector.html#dawn-1.

[143] Jun-Li Xu, Kevin V Thomas, Zisheng Luo, and Aoife A Gowen. Ftir and raman imaging for microplastics analysis: state of the art, challenges and prospects. *TrAC Trends in Analytical Chemistry*, page 115629, 2019. doi: https://doi.org/10.1016/j.trac.2019.115629.

[144] Renliang Xu. Light scattering: A review of particle characterization applications. *Particuology*, 18: 11 – 21, 2015. ISSN 1674-2001. doi: https://doi.org/10.1016/j.partic.2014.05.002. URL http://www.sciencedirect.com/science/article/pii/S1674200114001114.

[145] Dalia G Yablon. Overview of atomic force microscopy. In Dalia G Yablon, editor, *Scanning Probe Microscopy in Industrial Applications*, pages 1–14. John Wiley & Sons, Incorporated, 2013. ISBN 9781118288238.

[146] Y. T. Yang, C. Callegari, X. L. Feng, K. L. Ekinci, and M. L. Roukes. Zeptogram-scale nanomechanical mass sensing. *Nano Letters*, 6(4):583–586, 2006. doi: 10.1021/nl052134m. URL https://doi.org/10.1021/nl052134m. PMID: 16608248.

[147] Boon-Siang Yeo, Esther Amstad, Thomas Schmid, Johannes Stadler, and Renato Zenobi. Nanoscale probing of a polymer-blend thin film with tip-enhanced raman spectroscopy. *Small*, 5(8):952–960, 2009. doi: 10.1002/smll.200801101. URL https://onlinelibrary.wiley.com/doi/abs/10.1002/smll.200801101.

[148] Rodney A. Young and Ronald V. Kalin. *Scanning Electron Microscopic Techniques for Characterization of Semiconductor Materials*, chapter 4, pages 49–74. Honeywell Inc., 1986. doi: 10.1021/bk-1986-0295.ch004. URL https://pubs.acs.org/doi/abs/10.1021/bk-1986-0295.ch004.